ASME Applied Mechanics Reviews
Online journal at:
https://asmedigitalcollection.asme.org/appliedmechanicsreviews

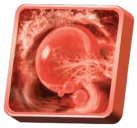

Mechanics and Dynamics of Organic Mixed Ionic-Electronic Conductors

Xiaokang Wang[1,2]
School of Mechanical Engineering,
Purdue University,
West Lafayette, IN 47907
e-mail: wangxk@illinois.edu

Xixian Yang[1]
School of Mechanical Engineering,
Purdue University,
West Lafayette, IN 47907
e-mail: yang1989@purdue.edu

Jianguo Mei
James Tarpo Jr. and Margaret Tarpo
Department of Chemistry,
Purdue University,
West Lafayette, IN 47907
e-mail: jgmei@purdue.edu

Kejie Zhao[3]
ASME Fellow
School of Mechanical Engineering,
Purdue University,
West Lafayette, IN 47907
e-mail: kjzhao@purdue.edu

Organic mixed ionic-electronic conductors (OMIECs) are a class of materials that can transport ionic and electronic charge carriers simultaneously. They have shown broad applications in soft robotics, electrochemical transistors, and bio-electronics. The structural response of OMIECs to the mixed conduction populates from molecular conformation to devices, presenting challenges in understanding their mechanical behavior and constitutive descriptions. Furthermore, OMIECs feature strong multiphysics interactions among mechanics, electrostatics, charge conduction, mass transport, and microstructural evolution. In this review, we summarize recent progress in mechanistic understanding of OMIECs and highlight dynamics and heterogeneity underlying each element of mechanics. We introduce strain activation and breathing, mechanical properties, and degradation of OMIECs upon electrochemical doping and dedoping. Drawing on the state-of-the-art experimental and simulation insights, we highlight the critical role of multiscale dynamics in governing the functionality of OMIECs. We discuss the current understanding and limitation of constitutive relations and present computational frameworks that integrate multiphysics. We synthesize mechanics-driven strategies—spanning strain modulation, material stretchability, and interfacial stability—from molecular design to macroscopic structural engineering. We conclude with our perspective on the outstanding questions and key challenges for continued research. This review aims to organize the fundamental mechanical principles of OMIECs, offering a multidisciplinary framework for researchers to identify, analyze, and address mechanical challenges in mixed conducting polymers and their applications. [DOI: 10.1115/1.4068298]

1 Introduction

Organic mixed ionic-electronic conductors (OMIECs) are a family of materials that have relatively high ionic conductivity [1,2] and electronic conductivity [3–5]. This review focuses on intrinsically mixed conductive π-conjugated materials, although other materials may also exhibit mixed conductivity, such as carbon nanotube composites with electrically insulating polymers and metal-organic frameworks (MOFs) [6]. Examples of π-conjugated materials include small molecules such as phenylene–bithiophene–phenylene (PTTP) [7,8], and polymers such as heterogeneous composite poly(3,4-ethylenedioxythiophene): polystyrene sulfonate (PEDOT:PSS) and homogeneous poly(3,3-dihexyl-3,4-dihydro-2H-thieno[3,4-b][1,4]dioxepine) (PProDOT-$(Hx)_2$) [9–11], Fig. 1(*a*).

Figure 1(*b*) shows the ionic and electronic conductivities of OMIEC materials [10] along with carbon and copper. As an example, MeOH/EtOH shear films of PEDOT:PSS achieved electrical conductivity of 8500 ± 400 S cm^{-1} [12,13], which is about the conductivity of tin. Electronic conduction of OMIECs is enabled by holes (electron vacancy) in p-type OMIECs, and by electrons in n-type OMIECs. Both intrachain and interchain conduction of charge carriers are present. Intrachain conduction is along the molecular backbone of π-conjugated materials, which is often simplified as alternating single and double bonds. The out-of-plane nature of the π bonds allows partial overlapping of electron clouds, or electron delocalization, enabling charge carriers to flow along the negative gradient of electrochemical potential. Interchain conduction occurs by hopping across molecules. This is sometimes assisted by a tie-chain from one crystalline domain to another [14], Fig. 1(*c*). Different models have been proposed to describe interchain electronic conduction in OMIECs, such as the variable range hopping model [7,15]. With more charge carriers, the electronic conductivity of the OMIEC backbone increases, and a percolative conduction network [16] is formed through intra- and interchain transport.

When OMIECs are in contact with an electrolyte, three typical processes take place near the OMIEC-electrolyte interface: solvation of the surface strands or partial dissolution [17], charge accumulation within the electrical double layer due to electrochemical potential difference and dipole interactions, and mass exchange across the interface. Mass exchange is through two mechanisms, Fig. 1(*d*). For relatively flexible chains where the persistent length of the chain is comparable to or smaller than the size of solvated ions [18], segment motion [19] wraps the solvents and ions, and assists with ion transport [20,21]. When the chains are relatively rigid, the solvents and ions diffuse in a "static" network of chains. The ingression of ions and solvents leads to mechanical swelling of OMIECs, microstructural annealing [22], softening [23], and charge redistribution [24], all of which subsequently influence

[1]X. Wang and X. Yang contributed equally to this work.
[2]Present address: Materials Science and Engineering, University of Illinois Urbana Champaign. Urbana, IL 61801.
[3]Corresponding author.
Manuscript received March 24, 2025; final manuscript received March 24, 2025; published online May 8, 2025. Assoc. Editor: Yonggang Huang.

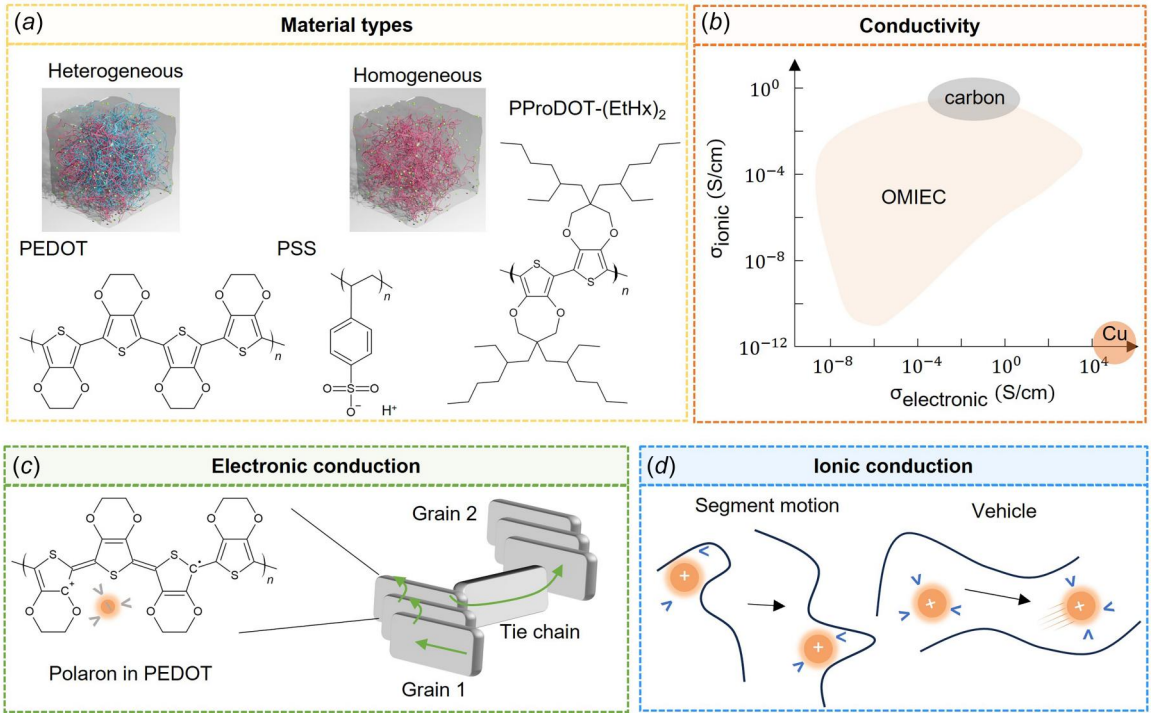

Fig. 1 Overview of OMIECs: (*a*) representative molecular structures of heterogeneous (PEDOT:PSS) and homogeneous (PProDOT-(EtHx)2) OMIECs, (*b*) electronic and ionic conductivities of OMIECs, (*c*) mechanism of electronic conduction in PEDOT, including polaron formation, intrachain and interchain transport, and (*d*) mechanism of ionic conduction, including segment motion and vehicle motion

the mass transport process. The phenomena are well documented in similar materials such as polyelectrolytes [25] and hydrogels [26].

Ionic and electronic conductions are intimately coupled in OMIECs and are both dictated by the microstructure of conducting materials and the external mechanical [27], chemical [28], electrical [29], and optical [30] fields. When electrons are extracted from a p-type OMIEC, electroneutrality requires injection of counteranions to (or ejection of complementary cations from) the vicinity of holes. In heterogeneous systems such as PEDOT:PSS, electronic conduction is through the semicrystalline PEDOT phase, and ion conduction is mostly in the amorphous PSS domain. For homogeneous materials, electronic conduction is along the molecular backbones while ionic conduction is through the side-chain region [31] or via unzipping/zipping mechanism in crystalline materials. The electrochemical redox reaction in OMIECs involving charge and mass transport is called doping and dedoping.

The charge (both electronic and ionic) and mass (such as solvent) transport induce mechanical strain and microstructural evolution such as change in crystallinity and phase segregation, which in turn, greatly affects the transport properties [32–34]. For example, the ionic conductivity of LiTFSI doped polyethers depends nonlinearly on water uptake, where the initial sorbed water slightly changes the conductivity, and a more significant increase in conductivity was observed with excessive swelling [35]. Recent work also argues that multicharged electronic complexes in OMIECs lead to structural ordering and disordering [36] and impact the mobility of charge carriers. These literature highlight the multiphysics complexity, both spatially and temporally, and call for a holistic perspective in understanding the working principle of OMIECs.

1.1 Emerging Applications of Organic Mixed Ionic-Electronic Conductors. The rich multiphysics in OMIECs have found many emerging applications, as shown in Fig. 2. The ability to volumetrically store charged ions provides OMIECs with high volumetric capacitance as supercapacitors [37]. Ion insertion/ejection-induced swelling/contraction can be utilized in double cantilever beam architectures acting as actuators for soft robots [38–40]. Charge extraction and insertion modulate the electronic structure of molecular backbones and absorption in the visible spectrum, which is used in electrochromic displays [41,42]. Notably, organic electrochromic displays have much shorter switching times and more color options than their inorganic counterparts thanks to the vast design space of molecular backbones. In an organic light-emitting electrochemical cell, the OMIEC is sandwiched between two metal electrodes, and light is emitted from the OMIEC layer when the electron and hole pairs recombine [43,44]. In organic thermoelectric devices [45], charge carriers redistribute and create an electrical potential difference when a thermal gradient presents across an OMIEC.

Another exemplary application is organic electrochemical transistors (OECTs) which take advantage of the mixed conduction and the insulator-to-conductor transition in an OMIEC [48]. An OECT consists of an electric circuit and an ionic circuit. The electric circuit is made of a source electrode (usually grounded) and a drain electrode separated by a semiconducting OMIEC channel. The electrical current in the electric circuit depends on the electrical conductivity of the OMIEC channel, which is modulated by the ionic circuit. The ionic flow is from the gate electrode in an electrolyte to the OMIEC channel. Therefore, the conductivity of the OMIEC channel and the drain current can be controlled by the gate voltage. OECTs are used in versatile applications, for instance, in chemical and biological sensing [49–51], where subtle differences in the gate voltage or the electrolyte condition can be amplified as large electrical current readout from the drain electrode. Also in logical circuits, OECT array-based complementary circuits [52] and neuromorphic computing [30,53] devices have been demonstrated.

1.2 Dynamics of Organic Mixed Ionic-Electronic Conductors. A salient feature of conducting polymers is that their molecular motifs, microstructure, and physiochemical properties evolve dynamically in the course of doping and dedoping. Figure 3 highlights a few examples of dynamics in OMIECs.

Packing motifs: Polymer chains stack with each other perpendicular to the backbone with a typical distance of $\sim 3-4$ Å ($\pi-\pi$

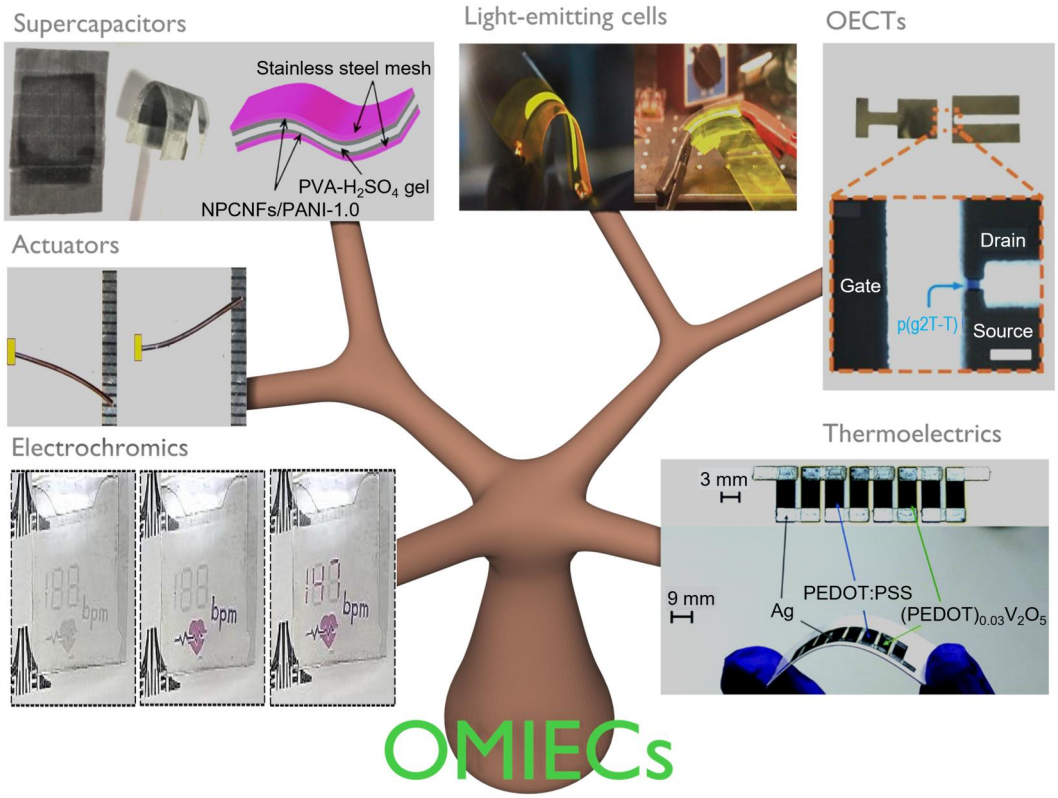

Fig. 2 Application of OMIECs owing to their mixed conduction nature. Examples include electrochromics (reprinted with permission from Ref. [46]), actuators (reprinted with permission from Ref. [38]), supercapacitors (reprinted with permission from Ref. [37]), light-emitting cells (reprinted with permission from Ref. [44]), OECTs (reprinted with permission from Ref. [47]), and thermoelectric devices (reprinted with permission from Ref. [45]).

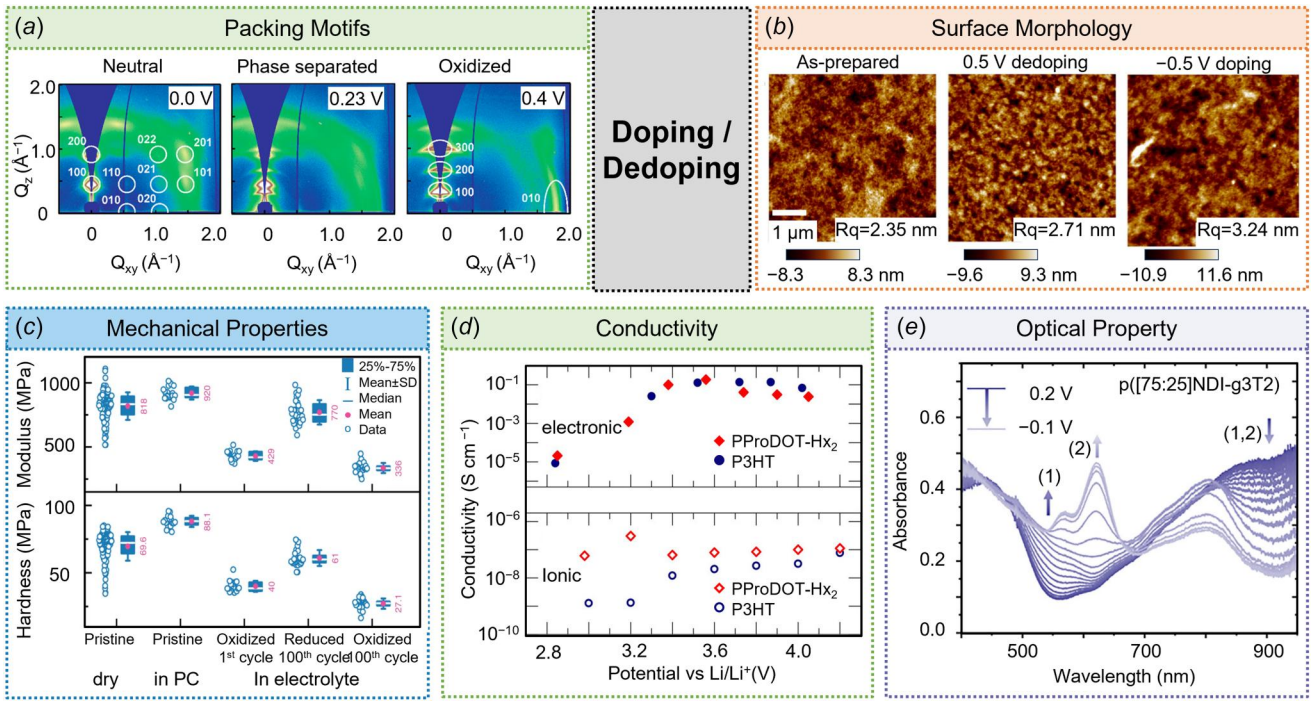

Fig. 3 Dynamic properties of OMIECs during doping and dedoping. (*a*) GIWAXS patterns of PB2T-TEG at neutral, phase-separated, and oxidized states. Reprinted with permission from Ref. [31]. (*b*) AFM height profiles of as-prepared, dedoped, and redoped PBFDO film. Reprinted with permission from Ref. [54]. (*c*) Elastic modulus and hardness of pristine dry, PC-immersed, first oxidized, 100th reduced, and 100th oxidized PProDOT thin film measured by in situ nano-indentation. Reprinted with permission from Ref. [55]. (*d*) The electronic and ionic conductivity of P3HT and PProDOT-Hx$_2$ as a function of doping level. Reprinted with permission from Ref. [56]. (*e*) Evolution of the absorbance spectrum of p([75:25]NDI-g3T2) during the first doping/dedoping cycle. Reprinted with permission from Ref. [57].

stacking). Stacks of the chains are then packed in a way such that the side chains are in contact (lamellar packing) [58]. Upon doping, insertion of ions and solvents disturbs molecular packing structures, which can be characterized by X-ray scattering techniques such as grazing incidence wide-angle X-ray scattering (GIWAXS) [31], Fig. 3(*a*). During doping of PB2T-TEG, the loss of crystallinity is inferred by the decrease of the number of distinct diffractions in the GIWAXS patterns. Structural annealing can also induce local crystallization as evidenced by the emergence of the (010) peak at full oxidation. Solvent aggregation in the side-chain region increases the lamellar packing distance as shown by the (h00) reflections.

Surface morphology: The surface morphology co-evolves with the molecular packing motif, and the microstructure may swell heterogeneously due to solvent and salt uptake during doping. Figure 3(*b*) shows the height profiles of PBFDO where the root mean squared roughness (R_q) increased from 2.35 nm to 2.71 nm upon dedoping and further to 3.24 nm after redoping [54].

Mechanical properties: The structural evolution and volumetric swelling during doping result in the variation of mechanical properties. The stiffness of polymers is related to the conformational entropy and enthalpic interactions of chains. Although a stiffer backbone is formed in the transition from the aromatic to quinoid structures by charge delocalization along the chains, material swelling usually has a larger effect on the stiffness which leads to decreased chain density and therefore reduced elastic modulus [29,55]. Figure 3(*c*) shows the elastic modulus and hardness of PProDOT thin films at the dry, wet, oxidized, and reduced states at different cycles measured by in situ nano-indentation.

Transport properties: Doping increases the density and mobility of electronic charge carriers, and the electronic conductivity can be increased by several orders of magnitude [56], Fig. 3(*d*). In contrast, the change of ionic conductivity during doping depends on the microstructure of the material. For crystalline-like OMIECs such as P3HT, doping causes loss of crystallinity and opens channels for ionic transport. Therefore, the ionic conductivity increases by about two orders of magnitude. However, for noncrystalline PProDOT-HX_2 with open structures, doping does not significantly change the ionic conductivity [22,56].

Optical properties: The electronic properties ultimately determine the absorbance spectrum of OMIECs. A precise control of the bandgap can be leveraged to tune the color and transparency of OMIECs. From the electronic structure view, charges on the backbone polarize its vicinity, interact with other charges, and form quasi-particles which are called polarons and bipolarons. Those charge carriers can be traced by the distinct peaks in the absorbance spectra, for example, polaron and bipolaron absorption of p([75:25] NDI-g3T2) are centered at ~575 nm and ~625 nm as shown in Fig. 3(*e*), respectively [57].

1.3 Strain Activation of Organic Mixed Ionic-Electronic Conductors. Strain activation is intrinsic to the operation of OMIECs in response to the local electrostatic interactions as well as the migration of compensating counterions and solvents from the surrounding electrolyte. The mechanical response of OMIECs should be tailored to their specific applications. In OMIECs that make use of strain activation for actuators, the volumetric strain is desired to be maximized for a large range of motion. Similarly, in a design of fluid microfilters [59] where polypyrrole (PPy) is coated on equal-spaced micropillar electrodes, Fig. 4(*a*), strain activation by sodium ion ingression determines the actual interpillar distance for sieving particles of various sizes. The accurate control of the doping level of OMIECs allows fine tune of the interpillar distance, and multisize selectivity of microfilter can then be achieved.

Mechanical swelling of conducting polymers can be detrimental to devices and their strain activation needs to be minimized. In applications such as organic electrochromic devices (OECDs), the conducting film is often bonded on a current-collector substrate which is mechanically inactive. Deformation of OMIECs causes

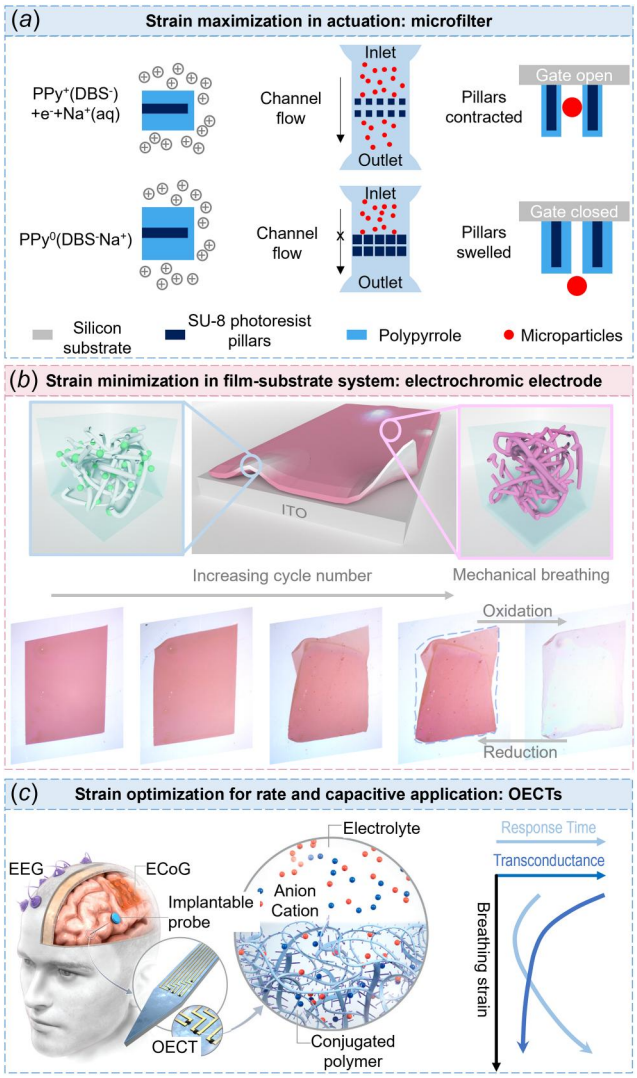

Fig. 4 Strain activation of OMIECs and its applications. (*a*) Strain actuation in microfilters where deformation is desired to be maximized. Reprinted with permission from Ref. [59]. (*b*) Breathing strain in film-substrate systems where minimized mismatch strain is needed for enhanced device durability. Reprinted with permission from Ref. [55]. (*c*) Strain activation in OECTs and bioelectronics where the swelling should be optimized for balanced rate and capacitive performance. Reprinted with permission from Ref. [60].

stress concentration at the interface [55] which induces wrinkling, cracking, and delamination of OMIEC films, Fig. 4(*b*). The structural disintegration disrupts charge transport and impairs the device's performance and durability due to the repetitive strain activation in each doping cycle. Yet, in other applications such as OECTs for biosensors [60], moderate electrolyte uptake and associated strain activation are necessary for a balanced high transconductance (ratio of the change in drain current to the change in gate voltage) and a fast rate performance, Fig. 4(*c*). While the transconductance often decreases nonlinearly with the volumetric strain, the response time of OECTs, determined by the conductivity of OMIECs, reaches a minimum before the percolation network for charge transport is disrupted by excessive strain activation.

1.4 Mechanical Failure in Organic Mixed Ionic-Electronic Conductor-Based Devices. Structural disintegration is one of the key mechanisms, along with the chemical and environmental degradation, that lead to the failure of OMIEC-based devices in

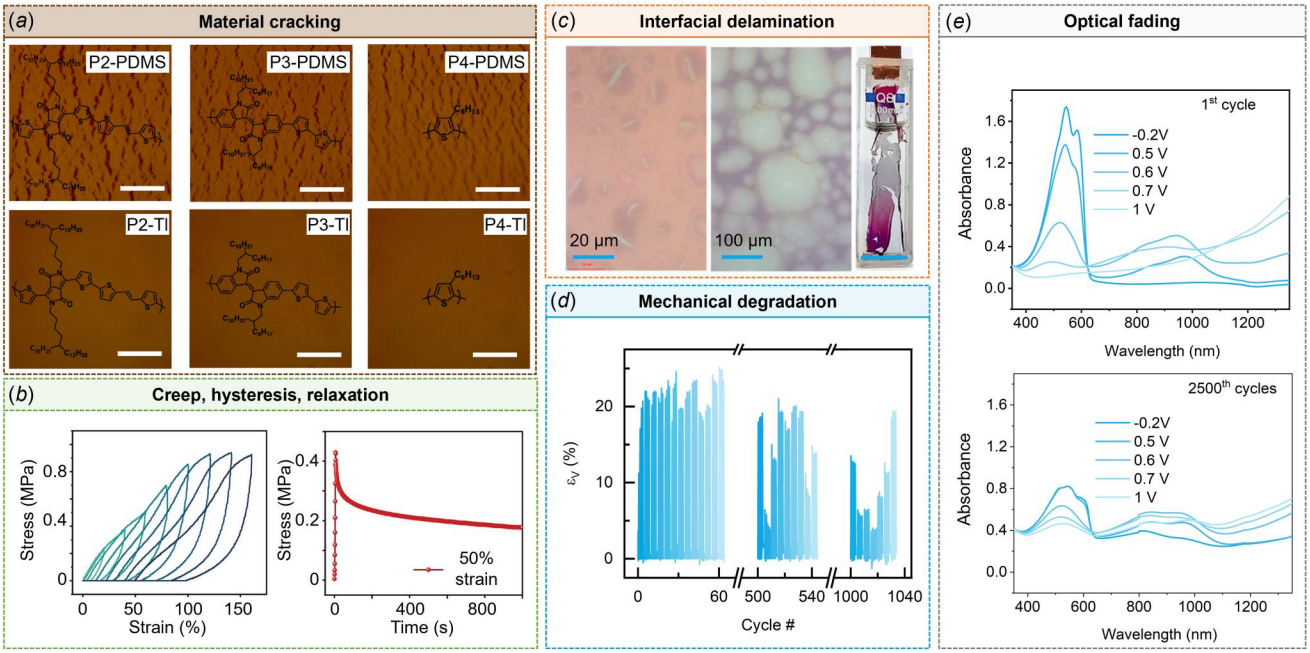

Fig. 5 Mechanical failure and its adverse consequence in OMIECs. (*a*) Cracking of OMIEC thin films shown by optical microscopy images of P*x*–PDMS (top) and P*x*–tough interface (P*x*-TI) (bottom) ($x = 2, 3, 4$). Scale bars: 20 μm. Reprinted with permission from Ref. [61]. (*b*) Creep, hysteresis, and stress relaxation in PEDOT:PSS/PAAMPSA/IL films. Reprinted with permission from Ref. [62]. (*c*) Interfacial delamination, (*d*) mechanical degradation, and (*e*) optical inactivity in PProDOT thin films over extended cycles. Reprinted with permission from Ref. [63].

long-term use. OMIECs are typically synthesized in solutions and coated as a thin film on a hard or soft substrate. Maintaining mechanical integrity, while allowing the breathing strain in the conducting polymers, has been a key challenge to retain the mixed conduction and functionality of the devices. Figure 5 demonstrates a few typical mechanical failure modes in OMIECs.

Thin film OMIECs bonded with soft substrates are often used for stretchable electronics such as wearable devices. Subject to the external stretch, channel cracking is found to be a dominating failure mode that disrupts charge conduction as shown in Fig. 5(*a*). At the material level, OMIECs also experience creep, stress relaxation, and hysteresis under external load, Fig. 5(*b*), making the electric output of actuators and soft robots less predictable.

Delamination derived from the edge of the interface with the current collector is another roadblock of the device durability. Figures 5(*c*)–5(*e*) show the observation of mechanical failure in poly (3,4-propylenedioxythiophene) (PProDOT) thin films on an indium tin oxide (ITO) coated glass substrate in an OECD. PProDOT gradually loses contact with the conductive substrate, which impedes the electronic and ionic conduction and ultimately causes uneven electrochromic color switching, reduced mechanical activity, and significantly reduced capability to modulate transparency in electrochromic devices. This example is a demonstration of how the mechanical response and degradation in OMIECs result in the convoluted consequences in their electrical, chemical, and optical properties. When it comes to the stability design of OMIEC devices in practical use, the multiphysics including the intimate coupling between strain activation, charge and mass transport, microstructure evolution, and structural mechanics must be taken into consideration.

1.5 Outline of the Review. The recent rapid development of organic electronics has catalyzed substantial progress in synthesizing and designing OMIECs. There are several notable reviews on the materials aspect of OMIECs [11,64,65], along with general reviews of the mechanics of soft and polymeric materials [66,67]. This review centers on the mechanics of OMIECs, emphasizing their dynamic behaviors, multiscale microstructural features, and the interplay between mechanical, electrochemical, and transport phenomena. We further explore how mechanics-driven design principles can optimize OMIEC performance. Specifically,

- Section 2 examines mechanical breathing—a phenomenon driven by mixed conduction—detailing passive/active swelling, electrochemical conditioning, microstructural annealing, and molecular-scale mechanisms of strain activation.
- Section 3 presents characterization techniques of mechanical properties across temporal and spatial scales, linking mechanical properties to doping kinetics for predictive material design and inferring doping kinetics from the mechanical measurements.
- Section 4 evaluates the constitutive models of polymeric materials and their strengths and limitations in describing OMIEC materials. This leads us to the physics-based continuum description of OMIECs and, in particular, the stress-transport coupling phenomena.
- Section 5 outlines design strategies to harness strain activation, enhance stretchability, and improve interfacial stability (e.g., adhesion, durability) through molecular engineering and structural optimization.

We conclude by identifying unresolved challenges—such as reconciling multiscale dynamics and improving device longevity—and opportunities for continued research. By structuring core mechanical principles of OMIECs, this review provides an interdisciplinary foundation for researchers to diagnose and tackle mechanical challenges in next-generation mixed conducting materials and devices.

2 Mechanical Breathing in Organic Mixed Ionic-Electronic Conductors

This section focuses on mechanical breathing—the repetitive volumetric swelling and shrinking—in OMIECs associated with electrochemical cycles of doping and dedoping. The deformation behavior of OMIECs is categorized into three distinct regimes: *passive swelling*, driven by thermodynamic absorption of solvent

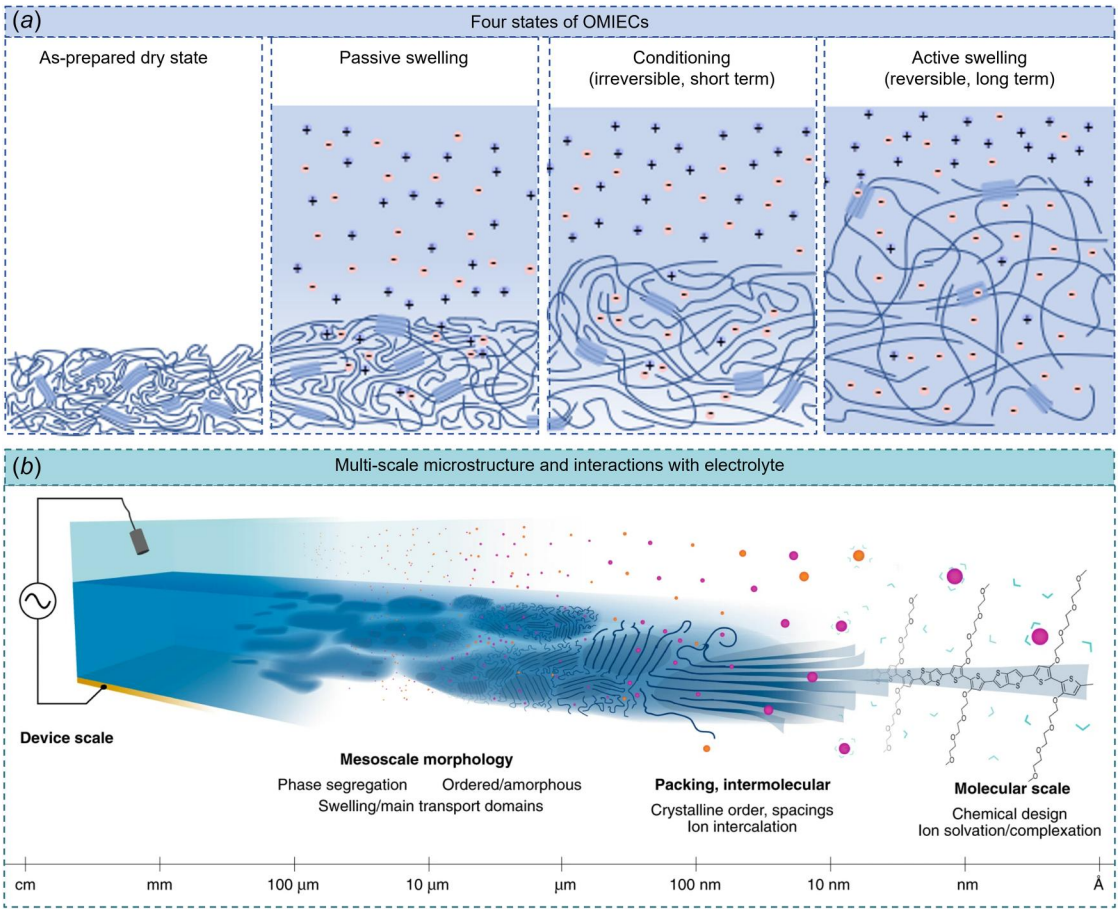

Fig. 6 Schematics of OMIECs at different states and microstructural features across different scales when OMIECs are in contact with the electrolyte. (*a*) OMIECs at the pristine dry, passive swelling, electrochemical conditioning, and breathing states. (*b*) Microstructural response of OMIECs populated at different scales, including chain conformational change at the molecular scale, packing motif at the intermolecular scale, texture evolution at the mesoscale, and overall volumetric change at the device level. Reprinted with permission from Ref. [11].

and ions in the absence of electrochemical bias; *electrochemical conditioning*, marked by irreversible microstructural reorganization during initial doping/dedoping cycles; and *active swelling*, involving reversible volumetric changes during sustained electrochemical operation. To elucidate these phenomena, we evaluate characterization techniques suited to different time and length scales, survey breathing strains in representative OMIECs, provide a mechanistic understanding of strain activation at the molecular scale, and correlate the kinetics of doping and dedoping of OMIECs with their mechanical response.

Figure 6(*a*) illustrates schematic representations of the polymer network in OMIECs at four distinct states. When submerged in a liquid electrolyte, dry OMIECs undergo passive swelling, where solvents and ions diffuse unevenly into the polymer matrix, driven by localized hydrophilicity (e.g., polar side chains). Active swelling initiates upon chemical or electrochemical introduction of dopants (charged species), triggering reversible volumetric changes. During the first few redox cycles, OMIECs with densely packed microstructures experience electrochemical conditioning, a reorganization process that stabilizes ion transport pathways and reduces irreversible deformation. Beyond this conditioning phase, swelling becomes predictable and cyclic during long-term operation. Concurrent with the breathing of OMIECs is the evolution of the structural features populated across several orders of magnitude spanning from molecular interactions to devices, Fig. 6(*b*). At the molecular/intermolecular scale, chain conformation depends on the doping level, side-chain hydrophilicity/lipophilicity (governing solvent uptake), and the solvation structure of dopants. At the mesoscale, heterogeneous phase domains (e.g., crystalline versus amorphous regions) modulate mechanical deformation. These domains, characterized by variations in crystallinity, composition, or hydrophilicity, influence swelling anisotropy and stress distribution. Notably, crystallite orientation relative to the substrate (e.g., edge-on versus face-on stacking) further impacts mechanical and electrochemical properties, as face-on stacked OMIECs exhibit higher resistance of ion permeability compared to the edge-on stacked counterparts [68]. At the macroscopic scale for devices, mechanical deformation is purposely harnessed in actuators, optimized for balanced rate and capacitive performance, or suppressed in film-substrate systems as discussed earlier.

2.1 Characterization Methods. Deformation takes place at different length scales such as macroscopic swelling, local microscopic deformation, and molecular packing and conformational change. Figure 7 provides a survey about the characterization methods of mechanical deformation in OMIECs at different scales spanning from the molecular scale to devices. The tensile test and electrochemical quartz crystal microbalance with dissipation (EQCM-D) method usually measure the macroscopic volumetric change of bulk materials; ellipsometry, nano-indentation, and AFM techniques provide morphological information at the micron down to nanometer scales; X-ray, electron microscopy, neutron scattering, and molecular dynamics (MD) modeling help understand the molecular scale behavior such as chain stacking and orientation. Therefore, deformation measurement should be put into the context of the characterization technique, working environment, and sample history. For instance, most conducting polymers exhibit strong

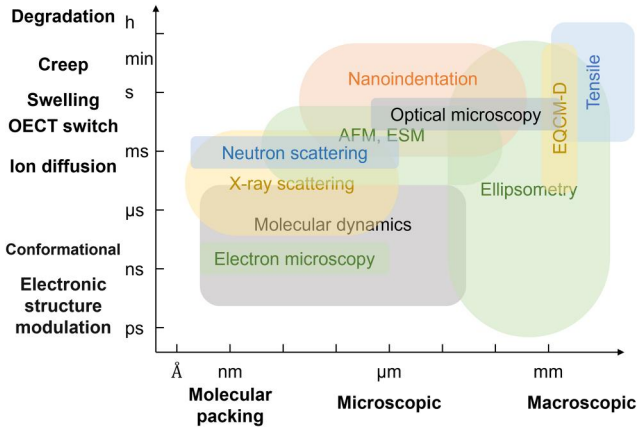

Fig. 7 Characterization methods of mechanical breathing. Methods include mechanical (tensile, EQCM-D) tests, imaging (optical and electron microscopy), ellipsometry, scanning probe microscopy (nano-indentation, AFM, ESM), scattering (X-ray, neutron, electron), and molecular simulations, which cover length scales from the molecular chain to device levels, and processes including degradation, creep, swelling, device operation, ion diffusion, chain vibration [69], and charge transfer [70].

heterogeneity in their microstructures, and local measurement of mechanical behaviors may largely deviate from the bulk property. When thin film samples are vitrified at the liquid nitrogen temperature in electron diffraction measurements, the result would only represent a snapshot of the dynamically evolving microstructure. In addition, OMIECs often show large irreversible deformation in the first few redox reactions—referred to as electrochemical break-in or conditioning—while their deformation becomes more reversible in subsequent cycles. In the following, we will briefly introduce each characterization method.

The optical imaging method [71] is facile to make a qualitative measurement of deformation. For example, >1000% volumetric swelling [72] is observed in a conjugated polymer poly-[3,3′-bis(2-(2-(2-methoxyethoxy)ethoxy)ethoxy)-2,2′-bithiophene], p(gT2), using optical microscopy. The large deformation is mostly due to solvent uptake by hydrophilic chains. Ellipsometry is a useful quantitative method [73,74], in which light interacts with the target material and the polarization change is quantified by the amplitude ratio and phase difference. Since the interaction is sensitive to the thickness and dielectric properties of the material, ellipsometry is a noncontact technique to measure the deformation of OMIECs during redox reactions.

The mechanical behavior of OMIECs is traditionally characterized by servomotor-based tensile tests [75–77]. A free-standing thin film is stretched between two conductive clamps in the electrolyte, and a small, constant ($\sim\mu$N) force is applied. The redox reaction triggers deformation of the thin film which is recorded by the tensile machine. Nevertheless, when the conducting polymer is thin, the processes of making free-standing films and sample clamping are challenging.

Developed in the 1980s, EQCM-D works for thin films of small area [78–81], where the materials are coated on the piezoelectric quartz crystal, and an alternating current is applied to excite the vibration of the composite of thin film and quartz crystal. When it deforms, the oscillation frequency is changed enabling the determination of change of the film thickness. Note that in EQCM-D, the frequency change and dissipation are often related to the stress–strain relationship, thickness, density, viscosity, and shear modulus of the film as well as the density and viscosity of the contacting liquid or gas. Such information is needed for accurate measurements.

Nano-indentation measures the force–displacement response of materials at microscale. We introduced two in situ methods to measure the mechanical breathing strain of OMIEC materials in a customized liquid cell [55,63]. In the static condition, we measure the breathing strain in a PProDOT film on ITO via the scratch test and targeted indentation. In the dynamic setting, we track the surface motion of thin-film electrodes during long redox cycles by applying a small force on the film. Atomic force microscopy (AFM) [82] and its most recent derivatives such as electrochemical strain microscopy (ESM) [83,84] probe deformation using a nanometer-sized tip. When an OMIEC film is immersed in the electrolyte, the conductive ESM tip taps its surface. The tapping mode induces local electrochemical reactions, and the mechanical response is measured by the deflection of the cantilever tip.

At the molecular level, crystalline domains of an OMIEC exhibit π-π and lamellar stackings surrounded by amorphous regions. Upon deformation, the stacking distance and chain conformation can change dramatically. Recently, X-ray [85] and neutron scattering [86], electron microscopy imaging [87], and electron diffraction [58,88] become the go-to methods for understanding the molecular information in OMIECs. Distinct peaks in the X-ray scattering and electron diffraction patterns can resolve the molecular packing distance and orientation in the crystalline domains and provide a ring pattern corresponding to the molecular spacing in the amorphous region. By measuring the distance between the direct beam and the scattered/diffracted beam, the stacking distance can be locally resolved. While X-ray scattering reports an averaged value in a micron-sized region, electron diffraction can resolve stacking spacing at the nanometer scale. In these measurements, potential damage by electrons and high-energy X-rays should be carefully controlled. By minimizing electron beam damage, π–π stacking [89] and even CH_2 groups [90,91] can be observed in conjugated polymers using high-resolution transmission electron microscopy. In parallel, neutron scattering [92–94] is particularly helpful in detecting the conformation and persistent length of polymer chains in OMIECs. OMIECs are generally stiffer compared to other hydrocarbon chains due to the ring-embedding bulky backbones, and the persistent length can range from a few to tens of nanometers [95].

Molecular dynamics simulations serve as "computational microscopy", which can capture material swelling, chain conformation changes, and even charge transport behaviors [72,96]. With the MD model, intermolecular packing motifs are characterized by computed XRD, radial distribution function, and coordination number, while chain conformation is represented by the end-to-end distance and persistence length. Two types of modeling—coarse-grained (CG) and all-atom (AA) MD—provide complementary hierarchical structural information of OMIECs. By treating a group of atoms as a single bead, CG models consisting of beads allow observation of heterogeneous ion and solvent absorption in OMIECs. The model size can be up to hundreds of nanometers, at the expense of resolving quantitative intermolecular structure and evolution. In comparison, AA MD describes all atoms explicitly and provides more quantified chain conformation and intermolecular packing structures of OMIECs upon strain activation with subnanosecond temporal resolution. Nevertheless, its size is limited to tens of nanometers and it is difficult to include mesoscale heterogeneity in the modeling.

The temporal resolution of the aforementioned techniques is largely different as well, representing physical processes related to mechanical deformation at different time scales. Generally, contact-based methods such as tensile test, nano-indentation, and AFM have a relatively low temporal resolution ($\sim$100 ms). They capture the material behaviors such as damage, creep, and active swelling. Ellipsometry and X-ray-based techniques are good tools for studying dynamic processes at shorter time scales (<100 ms) such as ion transport, device switching, and phase evolution [97].

2.2 Passive Swelling. Thermodynamically, passive swelling is driven by the entropy change of the polymer network from the unswollen to the swollen state [98], Fig. 8(*a*). Specifically, process (1) describes the formation of a network from chains, process (2) is associated with the mixing of chains with solvent molecules, and

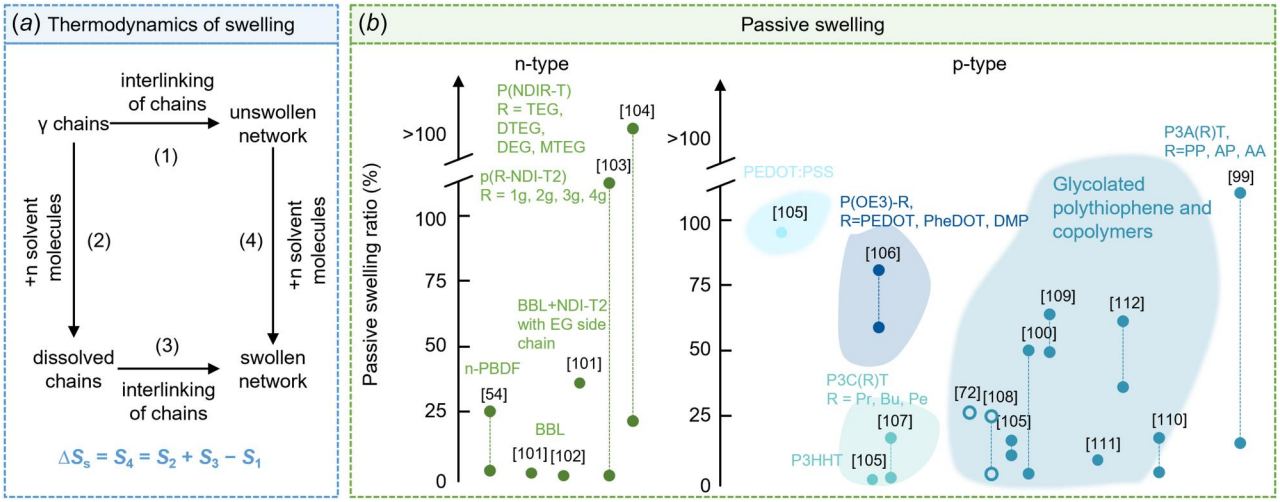

Fig. 8 Passive swelling of OMIECs: (*a*) thermodynamic origin of passive swelling of polymers in contact with electrolytes (reprinted with permission from Ref. [98]) and (*b*) survey of the passive swelling ratio of representative OMIECs. Data extracted from Refs. [54], [72], and [99–112].

process (3) relates to chain interlinking to form a network with the presence of solvents. Correspondingly, the entropy change of passive swelling of the OMIEC network in contact with solvent molecules (process (4)) can be calculated by the difference between the sum of entropies of processes (2) and (3) and that of (1).

Figure 8(*b*) gives a survey of the ratios of passive swelling mass (solid symbols) and volume (open symbols) in representative OMIECs which span a wide range from a few to more than one hundred percentages.

Recently, four-dimensional scanning transmission electron microscopy (4D-STEM) has been used to study the microstructural evolution in OMIECs. In 4D-STEM, a two-dimensional area is raster-scanned with a nanometer-sized electron beam, which generates a two-dimensional diffraction pattern at each scanning point. The technique reveals molecular and crystal stacking at nanoscale resolution. Notably, the Salleo group analyzed p(g3T2) in the dry, passively swollen, and subsequent dried states. The diffraction patterns are shown in Figs. 9(*a*)–9(*c*), and the radial-integrated intensity profiles reveal the lamellar, backbone, and $\pi-\pi$ stackings. The observations are insightful. First, the diffraction results show that the crystalline order at the mesoscale is preserved upon passive swelling. In addition, the lamellar stacking distance increased by ~50%, while the backbone and $\pi-\pi$ stacking signals show only subtle changes (<5%). These results indicate that water ingression into the side chain regions is the primary driving force for swelling, rather than the ions. The relative intensity changes of the lamellar, backbone, and $\pi-\pi$ stacking signals also suggest the drastic structural annealing upon swelling. Next, when the swollen

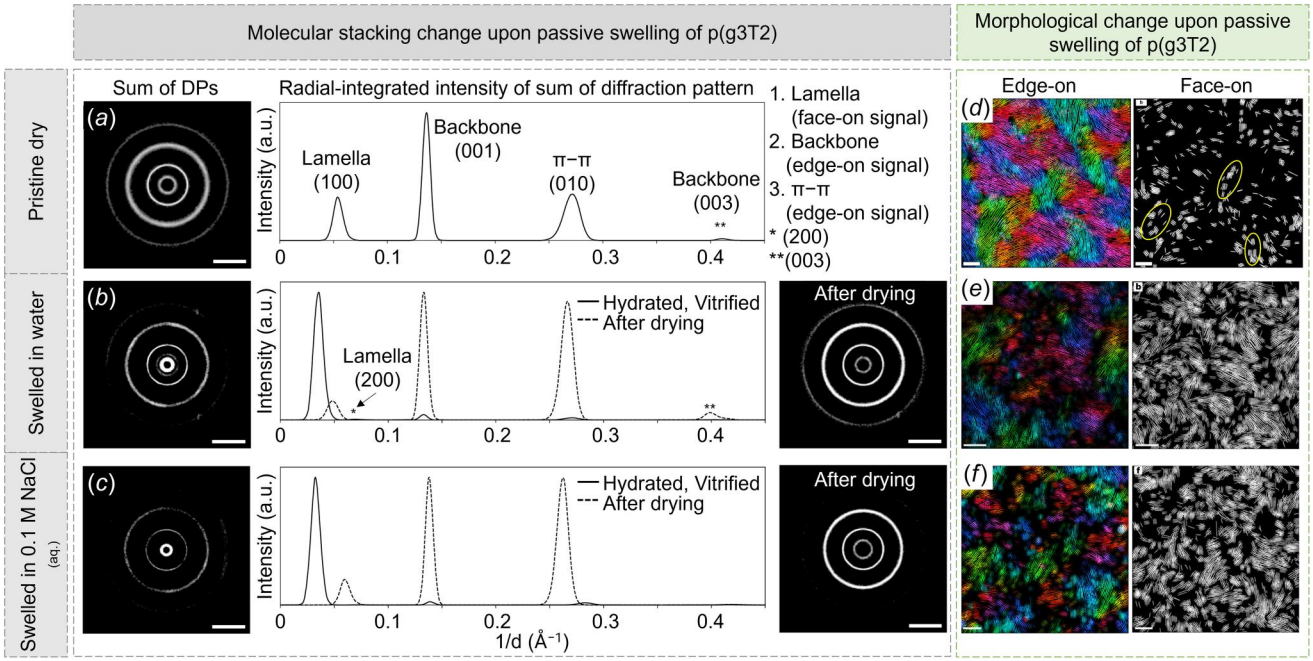

Fig. 9 Structural analysis of as-prepared and passively swollen p(g3T2). The diffraction patterns (DPs) and corresponding radial integrated intensity profiles for p(g3T2) films in (*a*) dry, (*b*) passively swollen in water, and (*c*) passively swollen in 0.1 M NaCl aqueous electrolyte. The DPs are in the swollen (left) and dried after swollen (right) state. 4D-STEM analysis of orientation of edge-on (colored) and face-on (grayscale) crystallites of p(g3T2) in (*d*) as-prepared dry, (*e*) passively swollen in water, and (*f*) passively swollen in 0.1 M NaCl aqueous electrolyte. Reprinted with permission from Ref. [58]. Scale bars: 2 nm^{-1}, 200 nm.

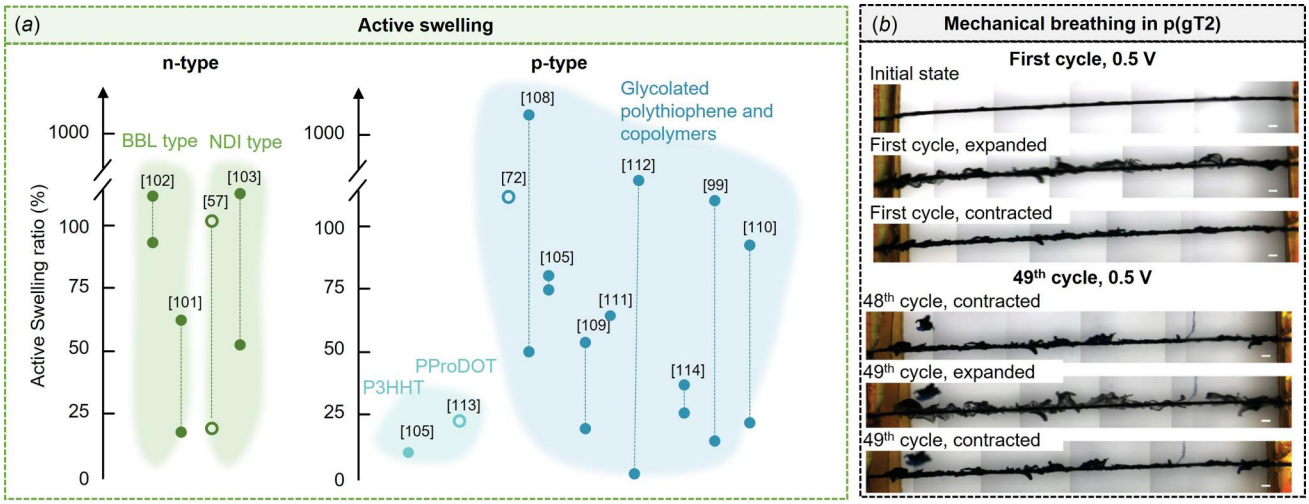

Fig. 10 Mechanical breathing of OMIECs. (*a*) Survey of the active swelling ratio of representative OMIECs. Data extracted from Refs. [57], [72], [99], [101–103], [105], and [108–114]. (*b*) Images of p(gT2) coated carbon fiber in the 1st and 49th electrochemical cycles. Scale bar: 100 μm. (Reprinted with permission from Ref. [72]).

polymer is dried in situ, the stacking signals are recovered, suggesting that the registry between polymers and the chain planarity remains. At each scanning point, the edge-on ($\pi-\pi$ stacking is parallel to the substrate) and face-on ($\pi-\pi$ stacking is perpendicular to the substrate) orientation maps of OMIECs are derived as shown in Figs. 9(*d*)–9(*f*). Lines in the maps show the direction of polymer chains, and the color code in the edge-on orientation represents different angles with respect to the horizontal direction. For as-prepared p(g3T2), the continuous edge-on orientation map demonstrates the liquid-crystal-like nature of the film. Yellow ellipses highlight noncontinuous face-on crystallites with long-range orientation correlations. Upon passive swelling, both edge-on and face-on orientation maps show similar "interrupted" regions. Such discontinuities suggest nonuniform ingression of the electrolyte, which primarily resides in the discrete intercrystalline regions. Due to the significantly enhanced lamella stacking signal, a network of face-on crystallites is uncovered upon swelling, which may have been below the detection limit or out of Bragg conditions in the dry film.

2.3 Active Swelling. Organic mixed ionic-electronic conductors "actively" swell when they are in contact with an electrolyte and subject to an external bias, which might be chemical dopants or electrical fields. The electrochemical bias alters the doping level of OMIECs, prompting an active change of volume and mass of the polymer mediated by electrolyte penetration. As a special case, electrochemical conditioning is often observed in OMIECs of high crystallinity which will be discussed separately in Sec. 2.4.

Figure 10(*a*) summarizes the ratios of active swelling mass (solid symbols) and volume (open symbols) for some representative OMIECs. Their values span a wide range from a few to more than a thousand percentages. As an example, Fig. 10(*b*) shows a set of optical images of p(gT2) coated on a carbon fiber in the 1st and 49th electrochemical cycles [72]. Oxidation of p(gT2) activates mechanical swelling. As p(gT2) is reduced to the charge-neutral state, the polymer partially contracts with the residual electrolyte inside p(gT2). The variability of active swelling provides a large space to tune the breathing strain in different applications as mentioned in Sec. 1.3. The design strategies will be discussed in Sec. 5.

Complementary to experimental measurements, MD modeling can unravel the molecular interactions and hierarchical structural responses including chain configuration, intermolecular packing motifs, and phase evolution. Figure 11 demonstrates the underlying mechanism of mechanical breathing of p(gT2) in an aqueous electrolyte. The active swelling is simulated by immersing self-aggregated p(gT2) into the electrolyte and the net charge on p(gT2) chains is updated to mimic different doping states upon oxidation. Meanwhile, counterions are added to the water to maintain the charge neutrality. The initial self-aggregated polymer chains rearrange in response to the electrostatic interactions and mass conduction of counterions and solvents. Upon reaching the equilibrated state, the active swelling volume is calculated by the overall morphology of p(gT2), as shown in the last column of Fig. 11, and representative chain aggregation and single chain configuration are used to demonstrate the local structural characteristics. Gradual electrolyte penetration into the polymer network and increased strain activation are observed when the oxidation increases from 5% to 30%. Chain aggregation shows pore formation and network expansion, and individual molecular chains continuously elongate from the coiled configuration to a relatively straight alignment which is quantified by the average end-to-end distance. In general, the packing motif including $\pi-\pi$ and lamellar stackings can be understood via simulated XRD patterns and radial distribution functions in MD simulations. In p-type OMIECs, lamellar stacking distance tends to increase due to electrolyte ingression between lamellae, whereas $\pi-\pi$ stacking distance usually decreases in active swelling because of chain elongation and increase of chain rigidity by the aromatic-to-quinoid transformation, which leads to a more planar chain configuration that facilitates the compact $\pi-\pi$ stacking. Nevertheless, opposite trends of $\pi-\pi$ stacking and lamellar packing have also been reported for some *p*-type and *n*-type OMIECs [115].

2.4 Electrochemical Conditioning. Electrochemical conditioning is also called "break-in," after which favorable paths for ion and solvent transport are formed and electrolyte uptake is stabilized. Conditioning is necessary before operation for some OMIECs of high crystallinity, and it can substantially change the morphology and various properties of OMIECs. However, this transition stage is often overlooked in literature. Here, we use Fig. 12 to demonstrate the dynamic changes of the packing motifs, optical property, redox reaction potential, and swelling volume of OMIECs in the conditioning cycles.

Packing motifs: For OMIECs with a relatively open structure such as PProDOT, little conditioning is observed over cycles. In other materials such as PCQTh of more crystallinity, significant conditioning occurs in the first ten cycles as shown in the diffraction profiles in Fig. 12(*a*) [116]. Compared to as-deposited PCQTh, the lamellar stacking peaks (100) at $q = 0.27\ \text{Å}^{-1}$ and (200) at $q = 0.54\ \text{Å}^{-1}$ disappear during conditioning, suggesting disruption of the regular packing as a result of electrolyte ingression and

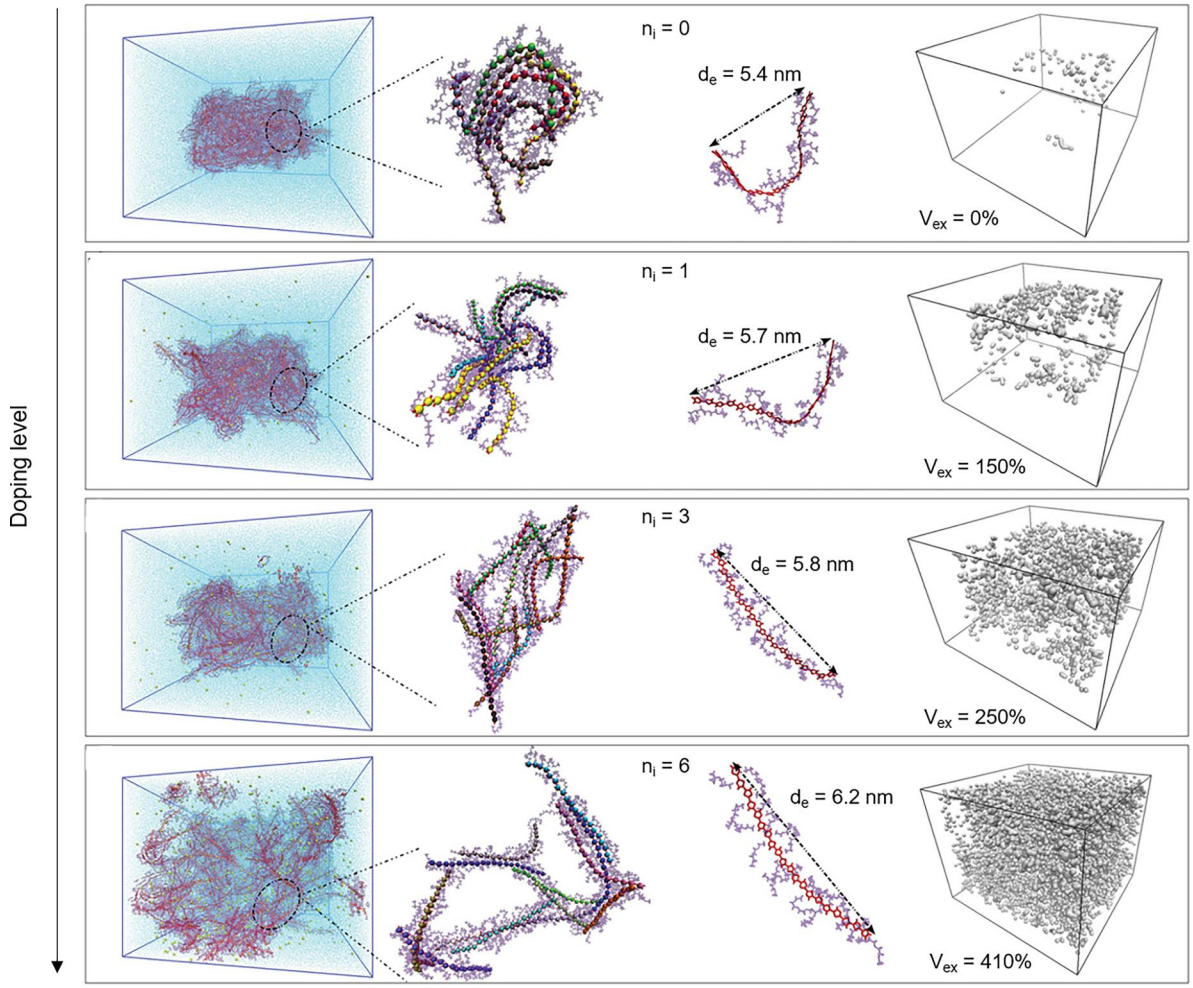

Fig. 11 Swelling of p(gT2) at various doping states in an aqueous electrolyte simulated by molecule modeling. The four sets of figures correspond to the doping level of 0%, 5%, 10% and 33%. n_i is the number of holes per p(gT2) chain which consists of 20 monomers. At each doping level, MD snapshots show an overview of p(gT2) in the aqueous electrolyte, a zoomed-in view of chain aggregate, a representative chain with the average end-to-end distance (d_e), and the volume of water uptake inside the polymer. Reprinted with permission from Ref. [72].

subsequent formation of amorphous PCQTh. Moreover, the emergence of the peak at $q = 1.1\ \text{Å}^{-1}$ indicates the presence of ionic crystal in the polymer from the electrolyte.

Optical property: Conditioning shifts the absorption spectrum of OMIECs, Fig. 12(*b*). For PProDOT-Am(Butyl)2, while little change in spectrum is observed in the organic electrolyte, a drastic redshift is identified after conditioning in the aqueous electrolyte [117]. Possible reasons are that organic electrolyte uptake facilitated by the amide functional groups requires minimum morphological rearrangement in the polymer, however, the limited amount of hydrophilic (polar) side chains may require significant structural reorganization for insertion of the hydrated polar ions.

Redox reaction potential: Upon the formation of favorable ion transport pathways, the overpotential reduces for doping and dedoping. The oxidation onset potential of DHPP-co-ProDOT shifts toward a smaller value and the slope of the reduction cyclic voltammetry (CV) trace increases after conditioning [118], Fig. 12(*c*). This is likely due to the structural rearrangement of DHPP-co-ProDOT during conditioning, leading to more rapid ion and solvent movement inside the polymer.

Active swelling volume: Fig. 12(*d*) shows the volumetric change of ethylene glycol functionalized polythiophenes during long doping/dedoping cycles [108]. The swelling ratio increases in the first tens of cycles before reaching the reversible state. Note that during deswelling, some solvent retains in the polymer, leading to a residual strain upon contraction.

2.5 Mechanistic Understanding of Mechanical Breathing. Electrostatic interactions and mass conduction of ions and solvents contribute to mechanical swelling of OMIECs. Taking p-type OMIEC during doping as an example in Fig. 13(*a*), several intertwined factors might be considered, including (I) volume expansion by electrostatic repulsion among the polymer chains of the same charge, (II) volume shrinkage induced by electrostatic attraction between the chains and compensating anions and also the electrostatic screening effect, (III) volume expansion due to the injection of anions, and (IV) volume expansion induced by the absorption of the solvent.

In experiments, swelling from absorption of the solvent and salt can be separately determined, for example, in EQCM-D [103]. The total number of injected charges during doping can be obtained from integration of current passed with respect to time, assuming Faradaic reactions. Then the contribution from solvent is the difference between the total mass increase and that of the dopants. This method works well for OMIECs with hydrophilic sidechains like ethylene glycol functionalized polythiophenes, which exhibit large active swelling. However, an overestimation can be made for OMIECs of relatively small deformation, because certain charges might be associated with oxygen reduction reactions as well as the possible cation/anion exchange [80,119,120]. In general, any non-Faradaic or side reactions that are not contributing to the carrier density would undermine the accuracy of the derived number of counterions in this method. Apart from counting the mass exchange, electrostatic

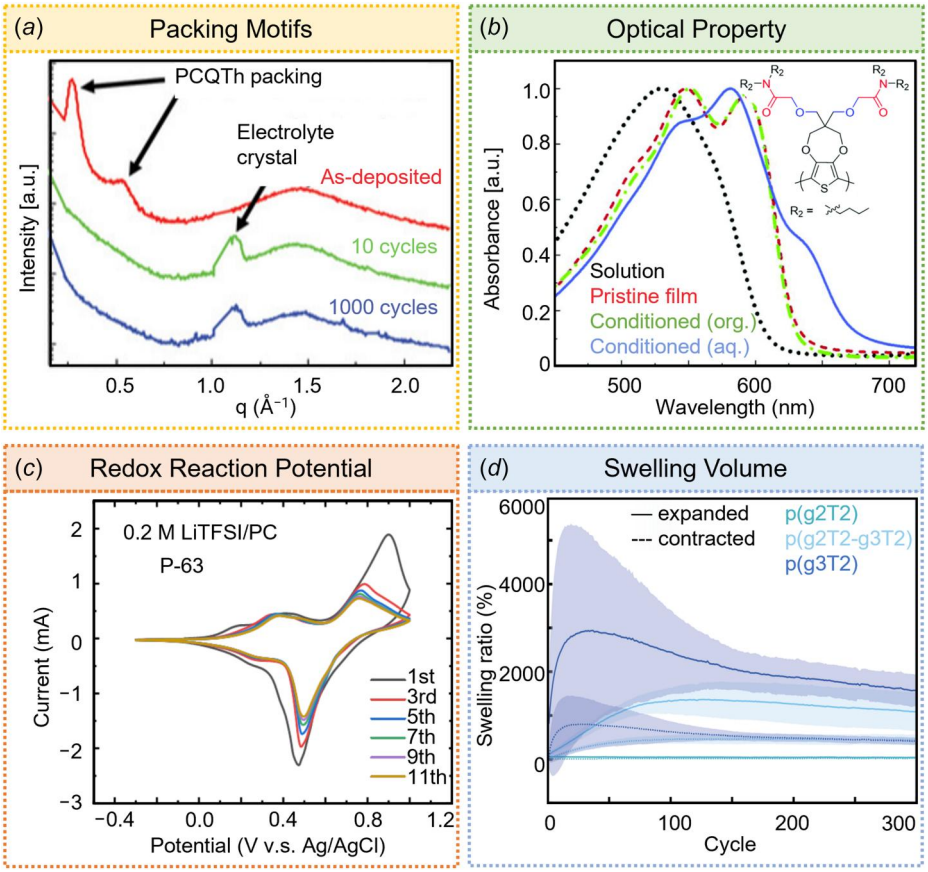

Fig. 12 Evolution of the microstructure and properties upon electrochemical conditioning in terms of the (*a*) packing motifs, reprinted with permission from Ref. [116], (*b*) optical property, reprinted with permission from Ref. [117], (*c*) redox reaction potential, reprinted with permission from Ref. [118], and (*d*) swelling volume, reprinted with permission from Ref. [108]

interactions between locally charged polymer chains and counterions cannot be directly captured in EQCM-D.

Molecular dynamics simulations offer mechanistic understanding of the underlying mechanism of strain activation in OMIECs. To decouple and quantify the contributions from different factors as discussed earlier, we built three molecular models as shown in Fig. 13(*b*) [22], where model 1 represents charge-neutral PProDOT as the reference, model 2 consists of oxidized PProDOT at the oxidation level of 33% and compensating counterions BF_4^-, and model 3 includes oxidized PProDOT immersed in the electrolyte of 1 M $LiBF_4$ in PC. Here model 2 considers electrostatic interactions and mass injection of counterions, while model 3 adds the solvent. The modeling shows an overall swelling volume of PProDOT of 21.3% upon full oxidation while the contribution from dopants is about 5.1%. In this case, mechanical swelling of PProDOT is predominant by the mass transport of the liquid electrolyte and particularly by absorption of the organic solvent (16.2%). This behavior is demonstrated via a pronounced decrease of the coordination number between PProDOT atoms when considering solvent ingression, as presented by Fig. 13(*c*) left panel, indicating a large expansion of the polymer network. The gradual solvent molecule and ion absorption upon doping is elucidated by the coordination numbers between PC and ClO_4^- with PProDOT as shown in Fig. 13(*c*) middle and right panels. The inset MD snapshots show visualization of the coordination environment.

2.6 Kinetics of Organic Mixed Ionic-Electronic Conductors Related to Mechanical Breathing. Kinetics of mass transport and swelling in hydrogels are well documented. In comparison, the mixed conduction in OMIECs renders strong coupling between ion transport and electronic conduction. Two examples in the following highlight the strong coupling and its relation to the breathing strain in conducting polymers.

The doping and dedoping kinetics can be inferred by monitoring the optical, electrical, or mechanical properties. Using multimodal nano-indentation as shown in Figs. 14(*a*) and 14(*b*), we showed that mechanical response of PProDOT thin films in organic solvent during doping is much faster than that in dedoping [63]. Recently, Ginger and coworkers summarized the asymmetric switching times in the doping and dedoping cycles in accumulative OECTs and concluded shorter times during switching off (dedoping), Fig. 14(*c*) [121]. Using optical microscopy, they observed that turn-on occurs in two stages—propagation of a doping front followed by uniform doping—while turn-off occurs in one stage. The faster turn-off is attributed to the intrinsic factors such as the carrier-density-dependent mobility, and the extrinsic factors including the channel geometry. The carrier-density-dependent mobility used to explain the rapid turn-off of OECTs is shown in Fig. 14(*d*). The discrepancy in the relative kinetics of doping and dedoping found in the two studies may be related to the materials structure, where amorphous PProDOT features more open channels for transport. Nevertheless, following this asymmetric kinetic behavior, the time scales of swelling and deswelling are also expected to be asymmetric.

Another manifestation of the strong coupling of mass transport and electronic conduction is the hole-limited electrochemical doping [122,123], as shown in Figs. 14(*e*) and 14(*f*). In PEDOT:PSS with a high hole mobility, the doping front initiates from the electrolyte. However, for p(g1T2-g5T2) with a low hole mobility in the dedeoped state, two moving fronts appear, where the first initiates from the ITO side which drains electrons until it meets the electrolyte, and then the second front propagates from the electrolyte toward ITO. Clearly, the mechanical activations of PEDOT:PSS and

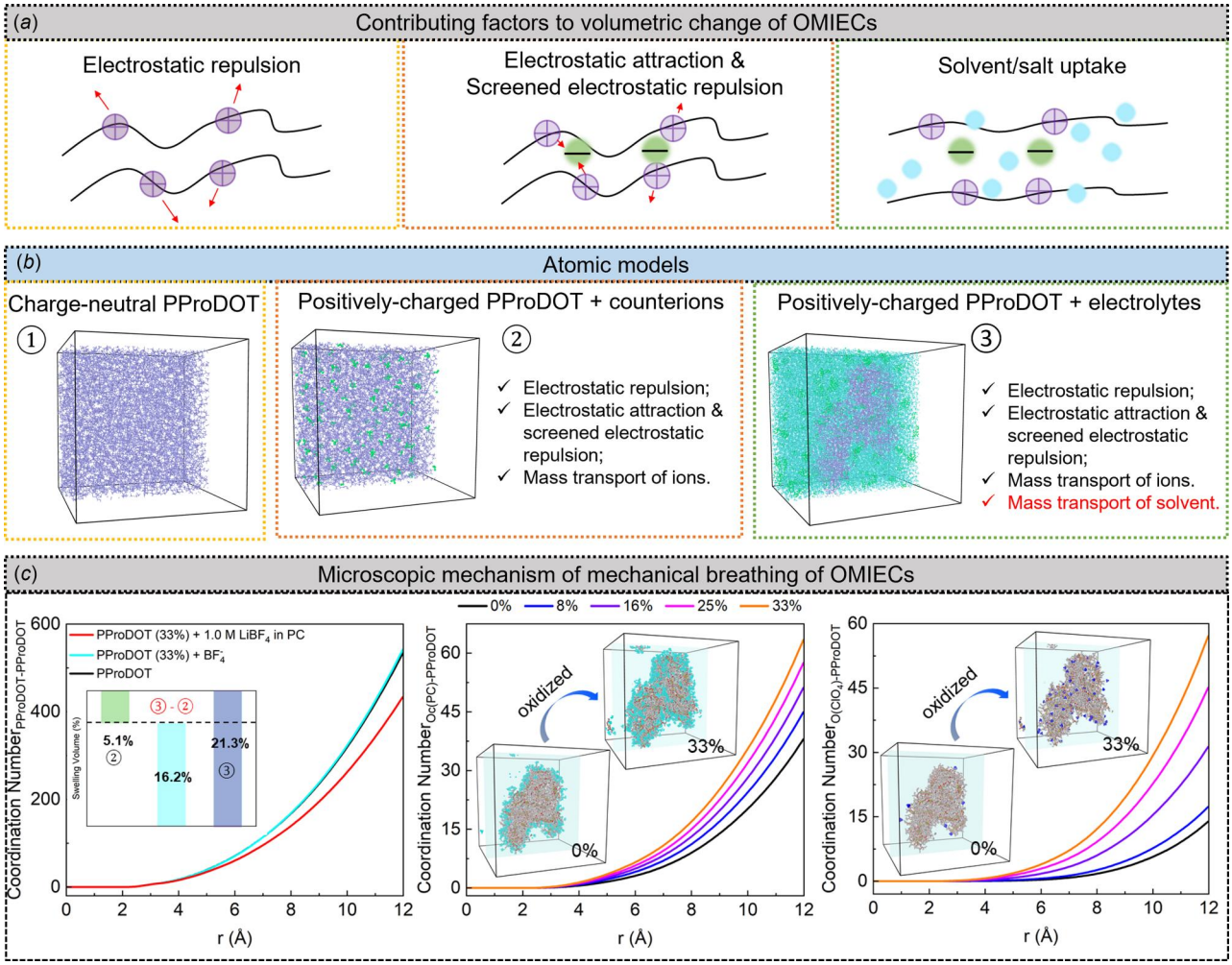

Fig. 13 Mechanistic understanding of mechanical swelling of OMIECs at different doping levels. (*a*) Schematics of volumetric change due to electrostatic interactions and salt/solvent uptake. (*b*) Three atomic models for MD simulation, including charge-neutral PProDOT as the reference system, positively-charged PProDOT and counterions BF_4^-, and positively-charged PProDOT in 1.0 M $LiBF_4$ in PC. (*c*) Cumulative coordination number of PProDOT-PProDOT in the three models in (*b*) and calculated volumetric changes. Cumulative coordination number of carbonyl oxygen (Oc) in PC and O in ClO_4^- with PProDOT, and representative MD snapshots of coordinating PC and ClO_4^- with PProDOT at various doping levels, respectively. Reprinted with permission from Ref. [22].

p(g1T2-g5T2) are different due to the drastic difference in their conduction behaviors.

3 Mechanical Properties of Organic Mixed Ionic-Electronic Conductors

This section will focus on understanding the mechanical properties of OMIECs using experimental measurements (Sec. 3.1) and simulations (Sec. 3.2). We highlight the dynamic nature of conducting polymers in the course of doping/dedoping in Sec. 3.3. Using the correlation between the mechanical properties and the chemical state, we demonstrate the potential leverage of mechanical tests to inform doping kinetics and material chemistry in Sec. 3.4.

3.1 Experimental Characterizations. Figure 15 summarizes the experimental characterization methods for the mechanical properties of OMIECs at different length scales and the typical sample size associated with each method [65]. Using these methods, many mechanical properties of OMIECs have been measured including modulus, hardness, yield strength, crack onset strain, toughness [124,125], and viscous properties [126].

Empirically, five basic molecular properties can be used to determine the elastic modulus and hardness of polymer materials [127,128]. They are the molecular weight, van der Waals volume, the length and number of rotational bonds in the repeat unit, as well as the glass transition temperature of the polymer. This method is powerful and tested on 18 polymers against the bulk measurement method as shown in Fig. 15(*b*).

Amongst the methods for bulk materials, tensile test is a versatile technique for a variety of properties such as Young's modulus, yield strength, tensile strength, toughness, and fracture strain [129]. Often, dedicated transfer techniques are used for free-standing samples due to the fragile nature of OMIECs [130,131]. Film-on-substrate and film-on-water experiments are also introduced as alternatives. They can be integrated with optical microscopy to monitor the morphological features of the sample such as the crack onset strain and crack propagation during loading. In the film-on-substrate method [132], Fig. 15(*c*), the mechanical properties of the OMIEC film are extracted from the stress–strain curve of the composite. A few drawbacks of the method are noted. First, the extraction becomes challenging if the conducting film is significantly thinner than the substrate, since the contribution of the film is indistinguishable from that of the substrate [133]. Second, the derived mechanical properties are influenced by the mechanical properties of the substrate and the interfacial condition [129]. Film-on-water is a pseudo-freestanding tensile test [133,134]. Water has a

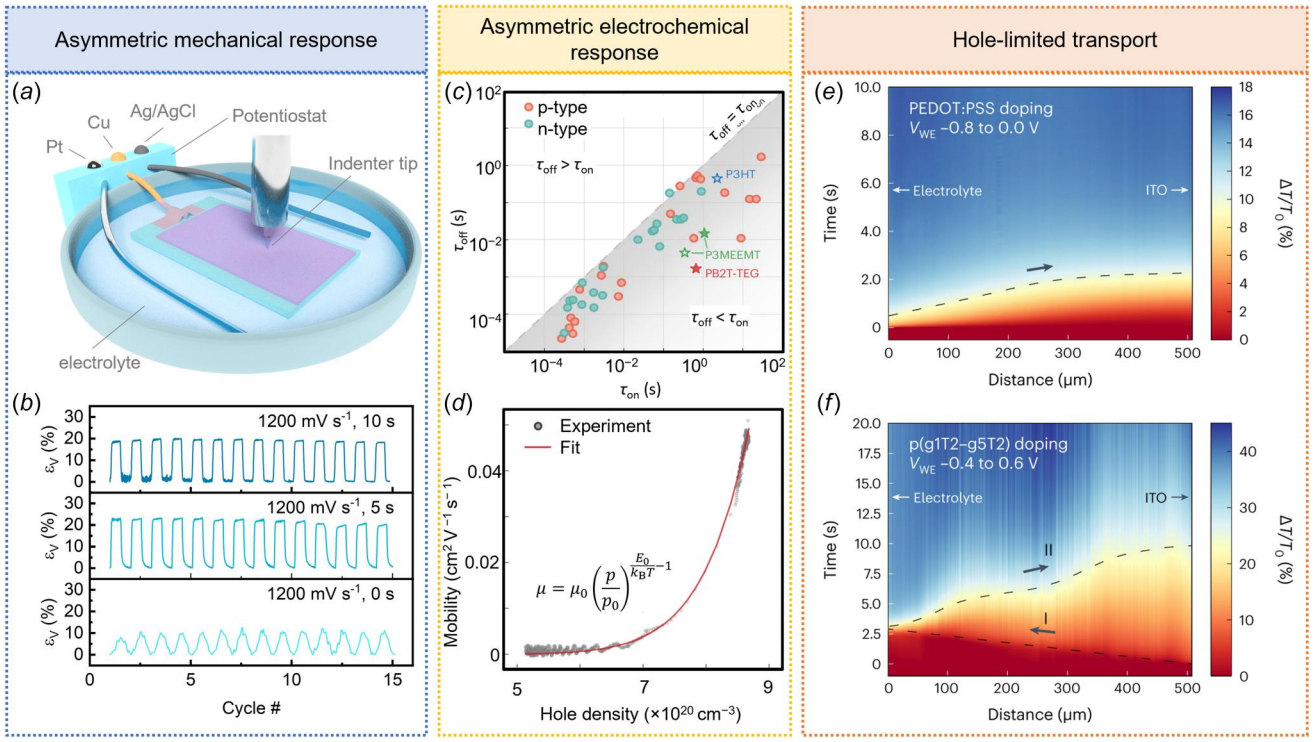

Fig. 14 Kinetics of swelling in OMIECs with strong ionic and electronic coupling. (*a* and *b*) Experimental setup of multimodal nano-indentation (*a*) and volumetric swelling during redox cycles of a PProDOT thin film (*b*). Reprinted with permission from Ref. [63]. (*c* and *d*) Switching times in accumulation model OECT (*c*) and carrier-density-dependent mobility explaining the rapid turn-off of OECTs (*d*). Reprinted with permission from Ref. [121]. (*e* and *f*) Transmittance change along thin films of PEDOT:PSS (*e*) and p(g1T2-g5T2) (*f*) during doping. Reprinted with permission from Ref. [122].

high surface tension that keeps OMIEC films afloat, and low viscosity that adds negligible friction as the film slides. However, water uptake into hydrophilic samples makes them ductile, leading to an overestimation of fracture strain. Figure 15(*d*) shows the strain at fracture of P(NDI2OD-T2) with varying molecular weights before and after annealing.

In the buckling method shown in Fig. 15(*e*), an OMIEC film is integrated onto a prestretched polymer substrate (such as PDMS). As tension is released, one-dimensional periodic wrinkles occur in the composite film. Similarly, wrinkles can be generated via direct compression or thermal mismatch strains in the film-substrate composite [131]. The wavelength of the wrinkles is measured by optical microscopy or laser dictation [135], and Young's modulus can be obtained by

$$\frac{\overline{E_f}}{\overline{E_s}} = 3\left(\frac{\lambda}{2\pi h}\right)^3 \tag{1}$$

where h is the film thickness, $\overline{E_f} = E_f/(1-\nu_f^2)$ and $\overline{E_s} = E_s/(1-\nu_s^2)$ are the plane-strain modulus of OMIECs film and the substrate [136], ν_f and ν_s are Poisson's ratio of the film and the substrate, respectively [137]. Equation (1) is valid for small prestrains and a stiff film on a compliant substrate. The buckling method is also used for measuring the yield strength of conjugated polymers [135]. In such measurements, stepwise tensile strains with an increasing magnitude are applied and released, and the surface is monitored by laser. In the elastic regime, wrinkles do not form upon release of the tension. As plastic deformation sets in, wrinkles occur after relaxation of the tension and thus diffracts the laser [135].

Nano-indentation can be also used to measure a variety of mechanical properties of OMIEC films. Using the force–displacement curve, the reduced modulus E_r is typically calculated by the Oliver–Pharr relation

$$E_r = \frac{\sqrt{\pi}}{2\beta}\frac{S_u}{\sqrt{A(h_m)}} \tag{2}$$

where β is a constant depending on the indenter tip shape, S_u is the initial slope of unloading, $A(h_m)$ refers to the projected contact area at the maximum indentation depth h_m. Young's modulus of the film can be calculated from E_r by

$$\frac{1}{E_r} = \frac{1-\nu_f^2}{E_f} + \frac{1-\nu_i^2}{E_i} \tag{3}$$

where E_f (E_i) and ν_f (ν_i) are Young's modulus and Poisson's ratio of OMIEC film (indenter tip), respectively. Hardness is calculated from the maximum load

$$H = \frac{P_{max}}{A(h_m)} \tag{4}$$

Figure 15(*f*) shows the load–displacement curves of PProDOT thin films at pristine and oxidized states. Electrolyte injection during oxidation reduces both Young's modulus and hardness of PProDOT, indicating a more compliant and softer PProDOT film.

For ultrathin OMIECs films, nano-indentation is difficult to apply because of the substrate effect. Atomic force microscopy (AFM) is an alternative for films of subhundred-nanometer thickness [138], Fig. 15(*g*). Here, the force is the adhesive/repulsive force between the film and the cantilever tip. To ensure linear elastic deformation, a blunted tip such as a spherical one is used. During the test, a force-separation (F_{tip}-δ) curve is recorded, from which Young's modulus can be extracted via contact models such as the Hertz model, Derjaguin–Müller–Toporov (DMT) model, and Johnson–Kendall–Roberts (JKR) model [139]. The Hertz model considers only contact within the elastic limit

$$F_{tip} = \frac{16E_r}{9}R^{\frac{1}{2}}\delta^{\frac{3}{2}} \tag{5}$$

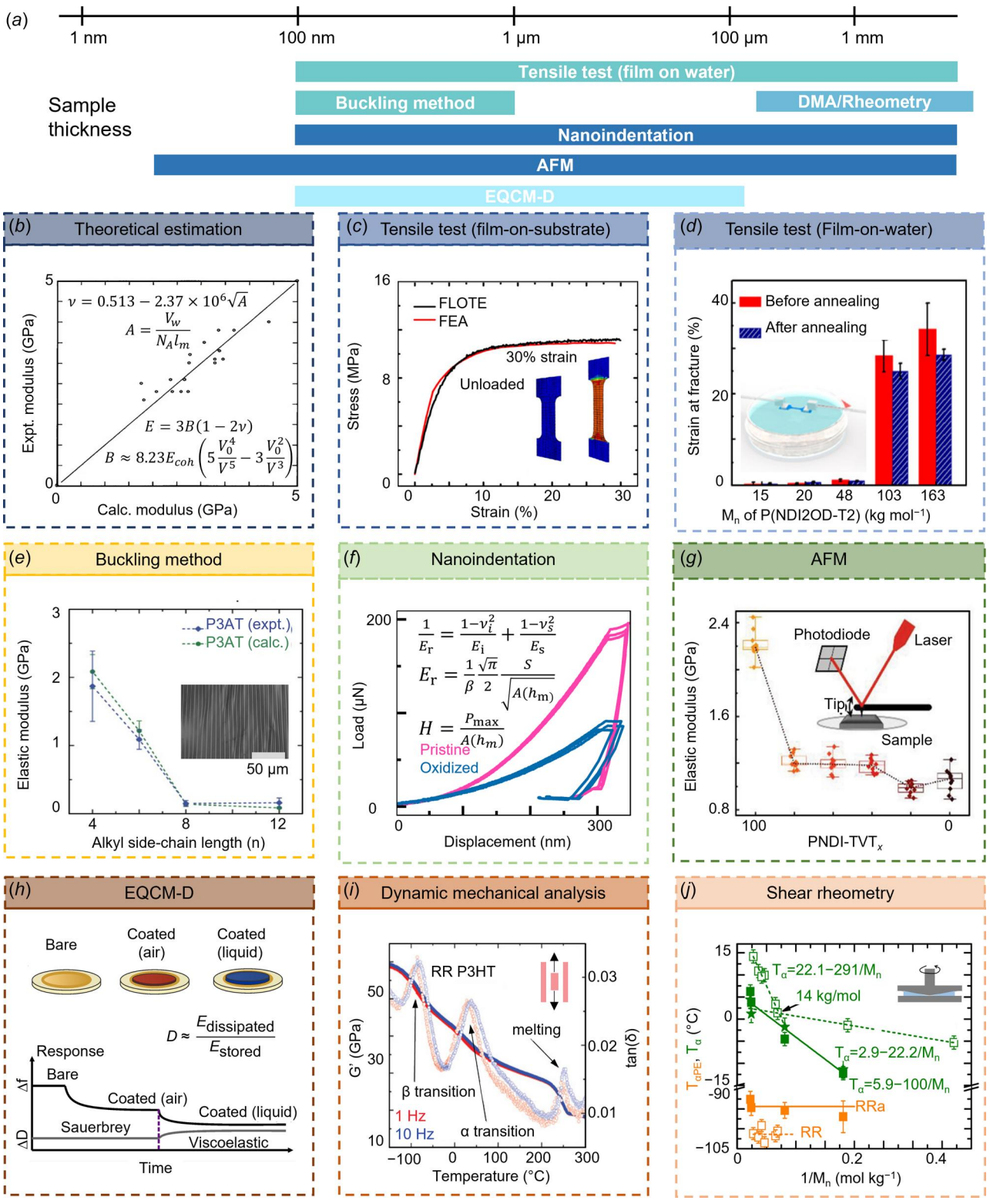

Fig. 15 Characterization methods for the mechanical properties of OMIECs. (*a*) Summary of experimental techniques and typical sample thickness. (*b*) Estimation of elastic moduli of 18 polymers from the thermodynamic theory. Reprinted with permission from Refs. [127] and [128]. (*c*) Film-on-substrate and (*d*) film-on-water tensile tests for the elastic modulus and strain at fracture. Reprinted with permission from Refs. [132] and [134]. Measurement of the elastic modulus from the buckling method (*e*), nano-indentation (*f*), and AFM (*g*). Reprinted with permission from Refs. [55], [128], and [137]. Measurement of the viscoelastic properties from EQCM-D (*h*), dynamic mechanical analysis (*i*), and shear rheometry (*j*). Reprinted with permission from Refs. [79], [142], and [153].

where R is the tip radius. Again, E_r takes the form in Eq. (2), and is obtained by fitting the unloading portion of the force-separation curve. The DMT model considers the tip-sample adhesion force F_{adh} [140] explicitly

$$F_{tip} = \frac{4E_r}{3}R^{\frac{1}{2}}\delta^{\frac{3}{2}} + F_{adh} \quad (6)$$

Figure 15(*g*) shows the addition of TVT reduces the elastic modulus of PNDI films. Note that for both nano-indentation and AFM, raster

scanning is possible to map the spatial heterogeneity of the samples [141].

Electrochemical quartz crystal microbalance with dissipation (EQCM-D) is commonly utilized to quantitatively determine the mass uptake of OMIEC films, which is linearly proportional to the frequency changes of overtones in the Sauerbrey range [79], Fig. 15(*h*). Assuming viscoelasticity such as that implemented in the Voigt model, the frequency curve can be used to extract the elastic properties [143,144]. However, the uptake of hydration water or wetting of sensor causes damping of the crystal oscillation. Therefore, dissipation must be compensated when fitting the elastic properties.

Dynamic mechanical analysis (DMA) and rheometry measure the rheological properties of OMIECs, such as the transition temperatures, Fig. 15(*i*). Specifically, stress–strain curves of samples subject to oscillating load are recorded under controlled temperatures, from which the storage modulus G′, loss modulus G″, and phase lag δ can be derived. Transition temperatures associated with side chain relaxation T_β and backbone relaxation T_α or T_g are identified via the distinct peaks of the tanδ profile. Figure 15(*i*) shows G′ (solid circles) and tan(δ) (open circles) of regioregular (RR) P3HT with two oscillating frequencies of 1 Hz (red) and 10 Hz (blue). Three distinct peaks are identified in the damping factor curve and are ascribed to β transition, α transition, and melting.

Rheometry is mainly for polymer melts, which are loaded between the rotating cone and stationary plate. Viscosity of the melts can be calculated by the ratio between shear stress and strain rate. Figure 15(*j*) shows the glass transition temperatures of regioregular (RR, empty symbols) and regiorandom (RRa, filled symbols) P3HT as a function of molecular weight. While the transition at T_α (green, ~0°C) related to backbone segmental relaxation is M_n dependent, $T_{\alpha PE}$ (orange, ~ −100°C) related to side chain relaxation is immune to molecular weight.

3.2 Molecular Modeling. Molecular dynamics (MD) simulations offer the flexibility to isolate the otherwise convoluted factors underlying the mechanical behavior. More importantly, molecular modeling provides key insights into local microscopic features, such as polymer chain conformation and entanglement, which are hardly accessible by experiments. However, MD simulations are limited by the model size and simulation time scales, requiring careful validation and comparison with experimental measurements.

All-atom (AA) and coarse-grained (CG) MD simulations allow access to multiscale structural features such as chain alignment, packing motifs, and entanglement. To represent chain entanglement and structural heterogeneities in practical OMIECs, polymer chains must be sufficiently long, often necessitating CG MD simulations. Figure 16(*a*) shows entanglement lengths in P3HT from the modified S-coil estimator (orange, upper) and S-kink estimator (black, lower), as a function of P3HT chain length [145]. With increasing chain length, entanglement lengths from both estimators converge, and the modified S-coil estimator approaches a physically reasonable value of 60 monomers.

By mimicking nano-indentation in experiments, Fig. 16(*b*), Young's modulus can be extracted from the MD models by

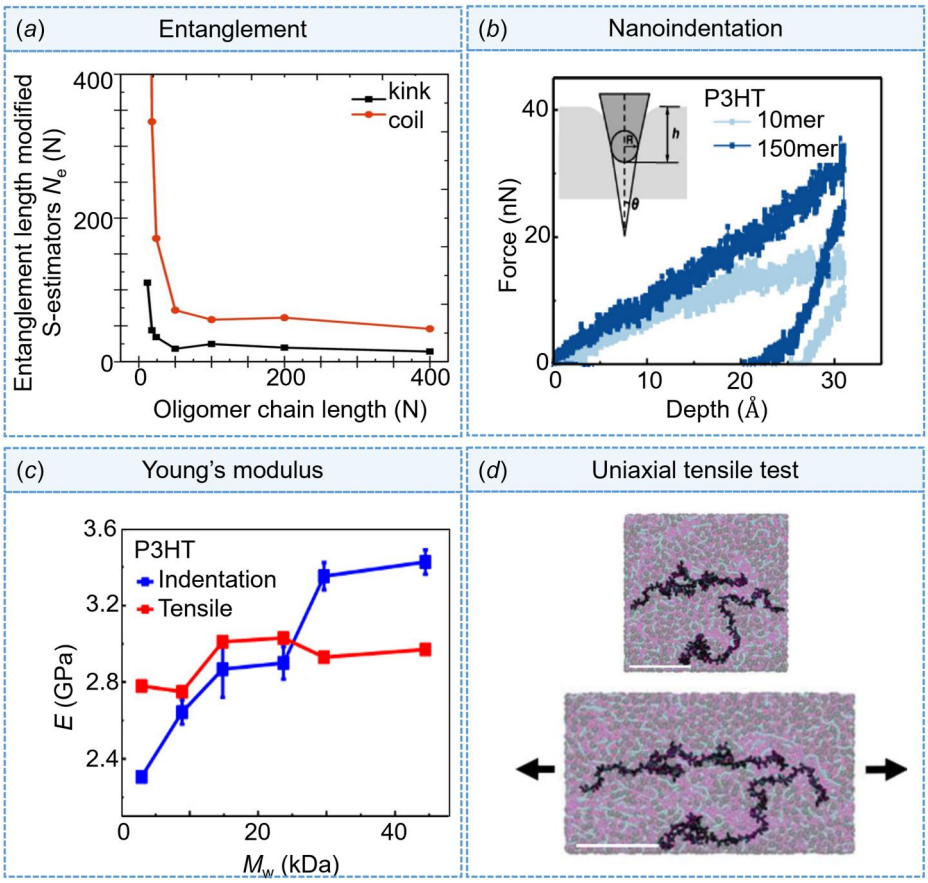

Fig. 16 Molecular dynamics simulations of the mechanical properties of OMIECs. (*a*) Entanglement length of P3HT from the modified S-coil estimator (orange, higher) and S-kink estimator (black, lower) as a function of the P3HT chain length. Reprinted with permission from Ref. [145]. Force-displacement curve (*b*) and Young's modulus (*c*) of P3HT versus molecular weight (M_w) by CG MD modeling. Reprinted with permission from Ref. [146]. (*d*) MD snapshots of P3HT:C60 heterojunction in uniaxial tensile simulation. Reprinted with permission from Ref. [147].

Table 1 Mechanical properties of Poly(3-hexylthiophene)

Property	Values	Characterization method
Young's modulus	1.23 GPa [147], 1.6 GPa [145], 3.0 GPa [146]	MD simulation—tension
	3.4 GPa [146]	MD simulation—indentation
	0.27 GPa [148]	Film on water method
	1.3 GPa [149]	Buckling method
	0.26 ± 0.027 GPa [150]	Viscoelastic nano-indentation
	1.7 GPa pristine, 1.1 GPa doped [151]	AFM
Hardness	0.21 ± 0.05 GPa [152]	Nano-indentation test
Yield strain and strength	4.3%, 44 MPa (–10 °C); 8%, 4 MPa (50 °C) [132]	Film on elastomer method
Tensile strength	4.5 ∼ 17.1 MPa (Mn: 15 kDa to 80 kDa) [148]	Film on water method
Strain at fracture	50% [130]	Tensile test (freestanding)
	100% (thickness:(∼80 nm), 70% (∼105 nm) [130] 4.5% to 95.6% (Mn: 15 kDa to 80 kDa) [148]	Film on water method
Storage/Loss modulus G′/G″	G′(RR) = 0.1 GPa [153]	DMA
Toughness	3–17 J/m^2 [125]	Four-point bending
Crack onset strain	2.83 ∼ 31.17% (Mn: 15 ∼ 80 kDa) [130]	Film on elastomer method
Shear modulus	0.93 GPa (AA MD); 1.28 GPa (CG MD) [154]	MD simulation

$$F = \frac{2E}{\pi(1-\nu^2)}\left[2Rh(1-\tan(\theta)) + h^2\tan(\theta)\right] \tag{7}$$

where F is the force on the indenter, E is the Young's modulus, ν is Poisson's ratio, R is the radius of curvature of tip apex, h is the indentation depth, and θ represents the half-opening angle of the tip. Figure 16(*c*) shows Young's modulus of P3HT as a function of the molecular weight in CG MD simulation [146]. Interestingly, the simulation reveals a stronger molecular-weight (Mw) dependence of modulus compared to that in the tensile test. The difference arises from different deformation mechanisms: tensile tests uniformly stretch polymer chains, whereas nano-indentation imposes localized, compressive deformation beneath the indenter. Also, low M_w P3HT fractures via chain pullout during tension, while high M_w sample experiences more substantial chain rearrangement, enhancing toughness and delaying fracture. Figure 16(*d*) shows CG MD snapshots of P3HT:C60 heterojunction before and after simulated uniaxial tension at the strain rate of 10^{-3} ps^{-1} [147]. Highlighted P3HT chains demonstrate the chain elongation from coiled conformations to extended, aligned structures under tension.

To contextualize the mechanical property data from both experimental and simulation methods discussed here, Table 1 tabulates the mechanical properties of a representative OMIECs—P3HT. The large variation in mechanical properties underscore the factors that need to be considered, including characterization methods, sample preparation procedures, molecular weight, sample geometry (such as film or fiber), and sample dimensions, into account.

3.3 Dynamic Mechanical Properties. The mechanical properties of OMIECs dynamically evolve upon doping and dedoping due to the changes in chain rigidity, intermolecular packing motifs, and electrolyte ingression, as shown in Fig. 17. For ease of illustration, p-type OMIECs, which are typically charge neutral at the as-prepared state, are used as examples in this subsection.

Upon doping, conjugated backbones undergo an aromatic-to-quinoid transformation, Fig. 17(*a*). This transformation renders polymer chains more planar and rigid, facilitating tighter $\pi-\pi$ stacking [108,155]. Additionally, as polymer expands in response to electrolyte uptake, coiled chains become elongated and align more readily, further enhancing intermolecular packing. Both experiments and MD simulations have reported that the $\pi-\pi$ stacking distance in swollen, doped p-type OMIECs becomes smaller—a seemingly counterintuitive observation—due to increase in the chain rigidity and planarity, as well as improved chain alignment.

Injected counterions inside OMIECs may serve as ionic crosslinkers (Fig. 17(*b*)), reinforcing polymer networks and influencing the mechanical behavior of OMIECs [156]. This crosslinking effect is pronounced in chemical doping and dedoping, where the solvent injection is absent or negligible, leaving the ion crosslinker to be dominant; otherwise, the effects of ions cannot be clearly separated from those of the simultaneously injected solvent molecules. On the other hand, solvent uptake causes swelling and decreases the chain density which reduces stiffness. Also, solvent molecules can act as plasticizers, making OMIECs film more compliant and stretchable [130]. For instance, the modulus of a dry, freestanding P3HT film is about 6% higher as compared to that in the film-on-water tensile test, Fig. 17(*c*).

3.4 Using Mechanical Properties to Inform Doping Kinetics. Accurate measurement of the doping level or the charge carrier density in OMIECs is essential to understand their behaviors because the electronic structure at a given doping level determines the mechanical, optical, and transport properties. Even for identical OMIECs, doping kinetics can differ widely depending on the dopant type and electrolytes [119], thus giving OMIECs of distinct properties.

One common approach to determine the number of charge carriers is to integrate the current with respect to time in experiments [113]. This method assumes that all charges contribute to doping,

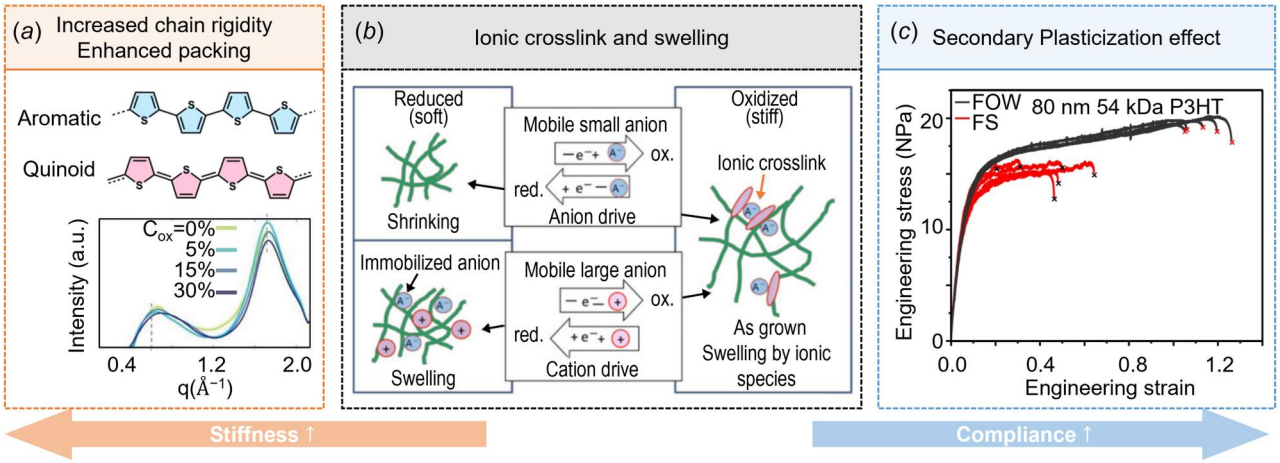

Fig. 17 Doping/dedoping-dependent mechanical properties of OMIECs. (*a*) Increased chain rigidity and enhanced packing promote the stiffness of OMIECs film. Reprinted with permission from Refs. [108] and [155]. (*b*) Schematics of injected counterions inside OMIECs serving as ionic crosslinkers which influence the mechanical properties of OMIECs. Reprinted with permission from Ref. [156]. (*c*) The secondary plasticization effect makes OMIEC films more compliant. Reprinted with permission from Ref. [130].

without considering non-Faradaic processes or Faradaic side reactions such oxygen reduction reactions (ORR), therefore resulting in an overestimation of charge density in OMIECs. Alternatively, in situ ultraviolant-visible spectroscopy qualitatively monitors doping through characteristic absorption peaks associated with quasi-particles such as polarons and bipolarons. Specifically, during doping, lattice distortions coupled with added charges create new electronic states, leading to distinct spectral signatures including neutral polymer $\pi-\pi^*$ transition around 400-600 nm, polaron absorption at 700–1200 nm, and bipolaron absorption between 1200 and 2000 nm. Other quantitative approaches such as X-ray photo-electron spectroscopy (XPS), nuclear magnetic resonance (NMR), and electron-spin resonance (ESR) are also useful. Reference [157] discussed the limitations of these methods.

Apart from the above-mentioned methods, a complementary approach to determine the local doping level of OMIECs is to use the doping-dependent mechanical properties. Although complicated by interactions among polymer chains, ions, and solvent molecules, mechanical properties could serve as a valuable fingerprint to decode the doping level. Figure 18 summarizes the methodology to determine the state of charge in a Si electrode by measuring the local Young's modulus, hardness, and film thickness [158]. The Li concentration-dependent mechanical properties and expansion coefficient are calibrated by nano-indentation as a reference, as illustrated in the upper panel of Fig. 18(*a*). Subsequently, a Si film undergoing lithiation in a moving front experiment is probed to obtain the spatial distribution of mechanical properties. Finally, by comparing the spatial profiles of mechanical properties to the reference, Li concentration distribution within Si is determined, as shown in the upper right panel. A similar principle can be adopted to map the local doping level in OMIECs using their mechanical property fingerprints.

4 Continuum Descriptions of Organic Mixed Ionic-Electronic Conductors

In this section, we discuss the constitutive modeling of polymeric materials and potential shortfalls of current models in describing the mechanical behavior of OMIECs. Using OECT as an example of OMIEC-based devices, we review two sets of phenomenological models in the literature – the electric circuit model and physics-based models including mechanics, electrostatics, charge conduction and mass transport, and microstructure evolution in OMIECs. We highlight stress-transport coupling in OMIECs observed in moving front experiments.

4.1 Constitutive Models of Polymeric Materials. Mechanical constitutive models describe the stress–strain relationship in materials. Excellent reviews of such topics are reported [66,67]. Our goal here is not to replicate the extensive discussions of those constitutive models. Instead, we will use a few representative examples to show the varieties of models, as summarized in Fig. 19. Phenomenological models are often applied in specific cases that are derived from considerations of certain physics and microstructural features in a given class of polymers. They use combinations of elastic springs and viscous dashpots to describe the stress–strain relationship in soft materials or define the strain energy using internal variables that describe the internal dissipation processes. In contrast, studies of polymer physics stem from statistical mechanics of polymer chains and consider the entropy and enthalpy components of the free energy of the chains. Regardless of the origin, one can define the free energy of the material as a function of the strain invariants, and stress and strain are then defined as work conjugates of the free energy. When damage happens due to chain scission or conformation changes, deformation becomes irreversible. Damage models describe these history-dependent stress–strain relationships.

Mooney–Rivlin model is a nonlinear hyperelastic phenomenological constitutive relationship for isotropic materials [159,160]. The strain energy density is expressed from experimentally determined materials constants C_1 and C_2 as

$$W = C_1\left(\overline{I_1} - 3\right) + C_2\left(\overline{I_2} - 3\right) \tag{8}$$

where W is the free energy, $\overline{I_1}$ and $\overline{I_2}$ are the first and second invariant (trace) of where W is the free energy, $\overline{I_1}$and $\overline{I_2}$are the first and second invariant of the $\bar{\boldsymbol{B}} = (\det \boldsymbol{B})^{(1/3)}\,\boldsymbol{B}$, respectively, and are expressed as the invariants I_1 and I_2 of the Right Cauchy Green deformation tensor $\boldsymbol{C}$ as shown in Figure 19(*b*).

Maxwell and Kelvin–Voigt models are the two most widely used linear viscoelastic phenomenological models. Both models can be generalized to include more springs and dashpots, so long as they are physically related to the underlying deformation mode. For example, the Maxwell representation of the standard linear solid model consists of a parallel circuit of a spring and Maxwell element of a spring-dashpot series. The free energy is expressed as

$$W = W_A + W_B \tag{9}$$

where W_A and W_B represents the energy stored in the springs. The deformation gradient of the material can be multiplicatively decomposed for the series subsection

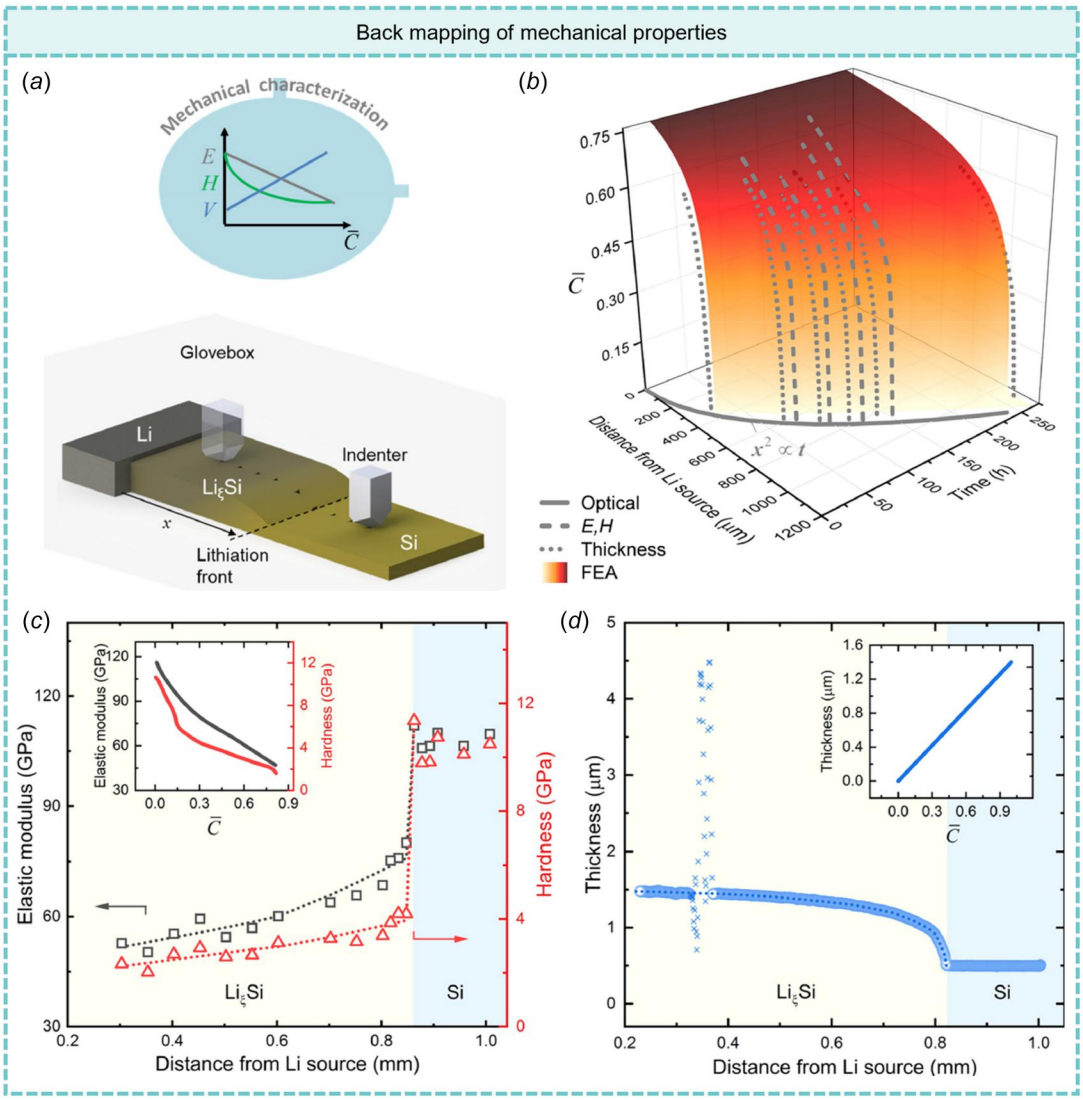

Fig. 18 Mapping Li distribution inside Si using the Li concentration-dependent mechanical properties. (*a*) Schematic illustration of chemical mapping using nano-indentation. (*b*) Spatiotemporal distribution of Li obtained from the optical imaging, local modulus/hardness, local film thickness, and finite element analysis (FEA). (*c*) Spatial distributions of elastic modulus and hardness of lithiated Si film. (*d*) Thickness measurement of lithiated Si film as a function of the distance from the Li source. Reprinted with permission from Ref. [158].

$$\boldsymbol{F} = \boldsymbol{F}_{\mathrm{A}} = \boldsymbol{F}_{\mathrm{B}} = \boldsymbol{F}_{\mathrm{Be}}\boldsymbol{F}_{\mathrm{Bv}} \tag{10}$$

where $\boldsymbol{F}_{\mathrm{Be}}$ and $\boldsymbol{F}_{\mathrm{Bv}}$ denote the elastic part and viscoelastic part of the series as shown in Fig. 19(*c*).

In general, the stress is obtained by

$$\boldsymbol{S} = \frac{\partial W}{\partial \boldsymbol{F}} \tag{11}$$

Therefore, the Mooney–Rivlin model gives

$$\boldsymbol{S} = \frac{2\partial W}{\partial \boldsymbol{C}} - p\boldsymbol{C}^{-1} \tag{12}$$

where p is the pressure. The stress for generalized Maxwell model is

$$\boldsymbol{S} = \boldsymbol{S}^{\mathrm{A}} + \boldsymbol{F}_{\mathrm{Bv}}^{-1}\boldsymbol{S}_{\mathrm{Be}}\boldsymbol{F}_{\mathrm{Bv}}^{-\mathrm{T}} \tag{13}$$

and to satisfy the second law of thermodynamics

$$\boldsymbol{C}_{\mathrm{Be}}\boldsymbol{S}_{\mathrm{Be}} : \boldsymbol{D}_{\mathrm{v}} \geq 0 \tag{14}$$

Physics-based models mainly consider the entropic effect of the molecular chains that are generally far from straight state without covalent bond stretching. In general, a polymer chain can be considered as N freely joined segments of length b, where b is the Kuhn length and $L = Nb$ is the chain length, as shown in Fig. 19(*e*). Using small-angle neutron scattering, the persistent length (half of the Kuhn length) of a polymer chain can be detected. The end-to-end length of a polymer chain is often significantly smaller than its length, and statistically related to its conformation. For example, if the Kuhn segments are all randomly and independently oriented, the distribution of the end-to-end distance is Gaussian

$$p(r) = \left(\frac{3}{2\pi Nb^2}\right)\exp\left(-\frac{3r^2}{2Nb^2}\right) \tag{15}$$

And the average end-to-end distance of the Gaussian chain is

$$\left\langle R \right\rangle = \sqrt{N}b \tag{16}$$

The entropy of a single chain s and the change upon deformation Δs is

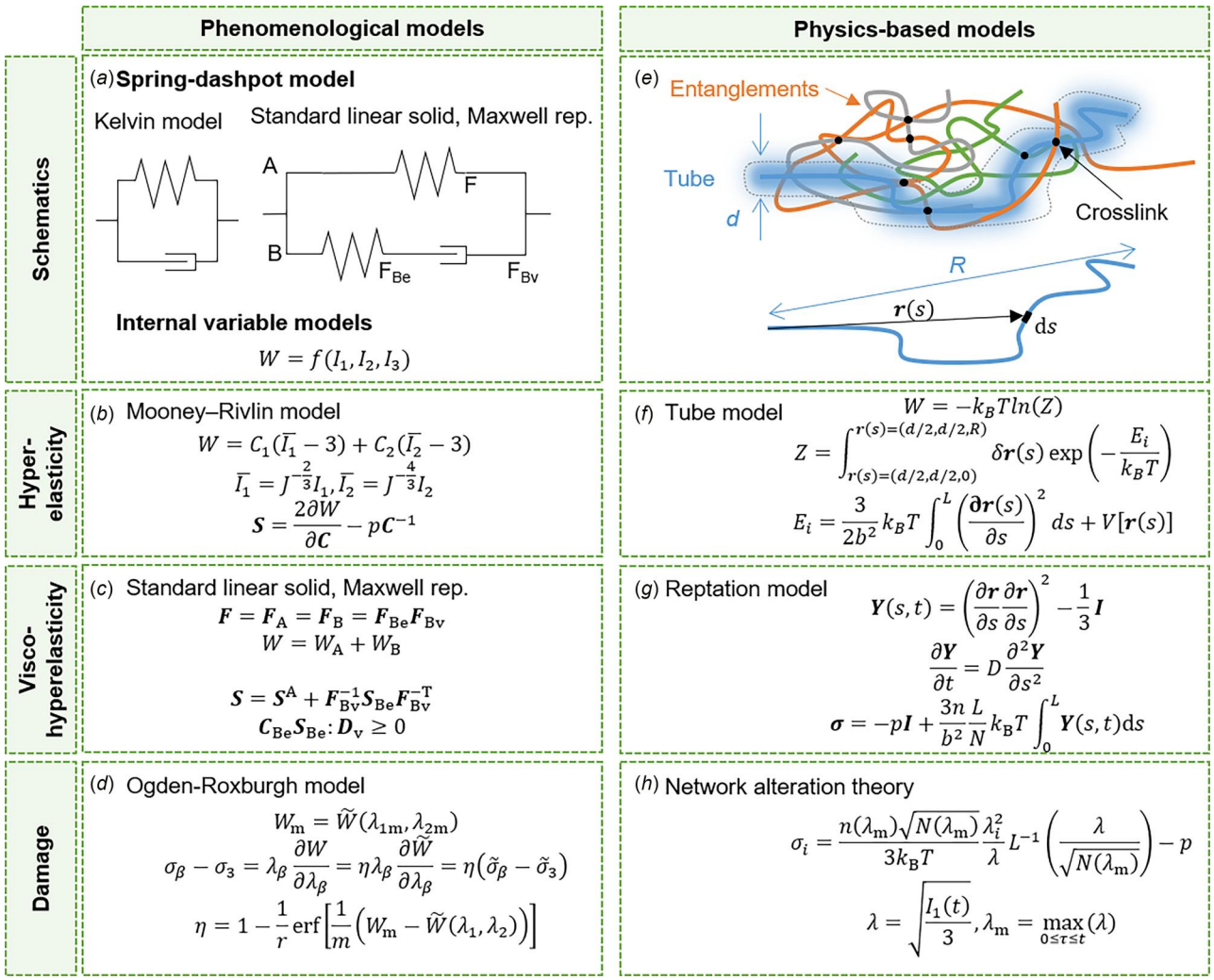

Fig. 19 Constitutive models of OMIEC polymers. (*a–d*) Phenomenological and (*e–h*) physics-based constitutive models for OMIECs. Schematics of spring-dashpot models (*a*) and a tube model (*e*). Representative models for hyper-elasticity (*b*, *f*), visco-elasticity (*c*, *g*), and damage (*d*, *h*).

$$s = k_B \ln(p(r)\mathrm{d}\tau) \tag{17}$$

$$\Delta s = s - s_0 = k_B \left[\ln\left(\frac{p(r)}{p(r_0)}\right) + \ln\left(\frac{\mathrm{d}\tau}{\mathrm{d}\tau_0}\right) \right] \tag{18}$$

where k_B is Boltzmann's constant, r (r_0) and $\mathrm{d}\tau$ ($\mathrm{d}\tau_0$) is the end-to-end length of the chain and the infinitesimally small volume element in the deformed (undeformed) states, respectively. Assuming incompressibility

$$\Delta s = -\frac{3}{2Nb^2} k_B \left(r^2 - r_0^2\right) = -\frac{3}{2Nb^2} k_B \frac{r_0^2}{3} \left(\lambda_1^2 + \lambda_2^2 + \lambda_3^2 - 3\right) \tag{19}$$

where λ_i is the stretch along the principal directions. Since $r_0 = \langle R \rangle = \sqrt{N}b$ in the undeformed state

$$\Delta s = -\frac{k_B}{2} \left(\lambda_1^2 + \lambda_2^2 + \lambda_3^2 - 3\right) \tag{20}$$

And the free energy density in a volume with chain density n is

$$W = -T\Delta s = \frac{1}{2} n k_B T \left(\lambda_1^2 + \lambda_2^2 + \lambda_3^2 - 3\right) \tag{21}$$

where T is the absolute temperature. This reduces to the Neo-Hookean model $W = \frac{1}{2}G(I_1 - 3)$ where $G = nk_BT$.

In the tube model, a polymer chain is considered to fluctuate in a tube with a diameter d enclosed by other surrounding chains [161]. The energy of a polymer chain can be expressed as the sum of contributions from conformational entropy and thermodynamic enthalpy

$$E_i = \frac{3}{2b^2} k_B T \int_0^L \left(\frac{\partial \boldsymbol{r}(s)}{\partial s}\right)^2 \mathrm{d}s + V[\boldsymbol{r}(s)] \tag{22}$$

where k_BT is the thermal energy, $\boldsymbol{r}(s)$ is the position vector of the segment $\mathrm{d}s$. $V[\boldsymbol{r}(s)]$ is the enthalpic energy which describes how the chain interacts with other chains. A partition function is defined which relates the energy of a specific conformation to its probability

$$Z = \int_{\boldsymbol{r}(s)=(d/2,d/2,0)}^{\boldsymbol{r}(s)=(d/2,d/2,R)} \delta \boldsymbol{r}(s) \exp\left(-\frac{E_i}{k_B T}\right) \tag{23}$$

where the summation goes through all possible conformation i. For tubes defined by the cross section parameter α_0, Z can be expressed as

$$Z = \left(\frac{3}{2\pi N b^2}\right)^{\frac{1}{2}} \exp\left(-\frac{3R_0^2}{2Nb^2}\right) \left(\frac{2}{d}\right)^2 \exp\left(-\alpha_0 \frac{Nb^2}{d^2}\right) \tag{24}$$

where R_0 is the end-to-end distance of the chain in the undeformed state, d is the tube diameter. The free energy of the chain is then

$$W = -k_B T \ln(Z) \tag{25}$$

The reptation model is based on the tube model, and describes the motion of polymer chains in the tube model [161,162]. The stress is defined as

$$\boldsymbol{\sigma} = -p\boldsymbol{I} + \frac{3n}{b^2}\frac{L}{N}k_B T\int_0^L \boldsymbol{Y}(s,t)\mathrm{d}s \tag{26}$$

where n is the number of molecules per unit volume, and $\boldsymbol{Y}(s,t)$ is a symmetric tensor representing the state of conformation of the polymer chain at time t

$$\boldsymbol{Y}(s,t) = \left(\frac{\partial \boldsymbol{r}}{\partial s}\frac{\partial \boldsymbol{r}}{\partial s}\right)^2 - \frac{1}{3}\boldsymbol{I} \tag{27}$$

The deformation dynamics is expressed as

$$\frac{\partial \boldsymbol{Y}}{\partial t} = D\frac{\partial^2 \boldsymbol{Y}}{\partial s^2} \tag{28}$$

where D is the diffusion constant.

In damage models, internal variables such as damage factors are often defined which relate the stress in an ideal material to the damaged material. For example, the Ogden-Roxburgh model [163] relates the damage factor η to the difference between the strain energy of a damaged material at stretch of λ_β and that of an ideal material at stretch of λ_m by an error function

$$\eta = 1 - \frac{1}{r}\mathrm{erf}\left[\frac{1}{m}\left[W_\mathrm{m} - \tilde{W}(\lambda_1, \lambda_2)\right]\right] \tag{29}$$

where $W_\mathrm{m} = \tilde{W}(\lambda_{1\mathrm{m}}, \lambda_{2\mathrm{m}})$ is the strain energy of the damaged material upon unloading at $\lambda_{1\mathrm{m}}$ and $\lambda_{2\mathrm{m}}$, and $\tilde{W}(\lambda_1, \lambda_2)$ is the strain energy of ideal material. The stress is expressed as

$$\sigma_\beta - \sigma_3 = \lambda_\beta \frac{\partial W}{\partial \lambda_\beta} = \eta\lambda_\beta \frac{\partial \tilde{W}}{\partial \lambda_\beta} = \eta(\tilde{\sigma}_\beta - \tilde{\sigma}_3) \tag{30}$$

where $\tilde{\sigma}_\beta$ is the stress in ideal material.

At the molecular scale, the linker chain scission at the junctions increases the number density of chains and the number of Kuhn segments in a chain. This is described in the network alternation theory [164] based on the incompressible Arruda–Boyce model by $N = N(\lambda_\mathrm{max})$ and $n = n(\lambda_\mathrm{max})$, where Nn = constant. The stress in the damaged state is

$$\sigma_i = \frac{n(\lambda_\mathrm{m})\sqrt{N(\lambda_\mathrm{m})}}{3k_\mathrm{B}T}\frac{\lambda_i^2}{\lambda}L^{-1}\left(\frac{\lambda}{\sqrt{N(\lambda_\mathrm{m})}}\right) - p \tag{31}$$

$$\lambda = \sqrt{\frac{I_1(t)}{3}} \tag{32}$$

$$\lambda_\mathrm{m} = \max_{0\le\tau\le t}(\lambda) \tag{33}$$

where L^{-1} is the inverse Langevin function.

4.2 Limitation of Current Models and Unique Features of Organic Mixed Ionic-Electronic Conductors. Classical constitutive models such as the Neo-Hookean model, Arruda-Boyce model, and others work well for rubbers and hydrogels due to their crosslinking and long, linear polymer chains (molecular weight of the order of MDa [165]). Similarly, polymer chains in hydrogels have hydrophilic side groups and are often crosslinked as shown in Figs. 20(*a*) and 20(*b*).

In contrast to rubber and hydrogels, the complexity of both polymer chains and the microstructure poses a significant challenge

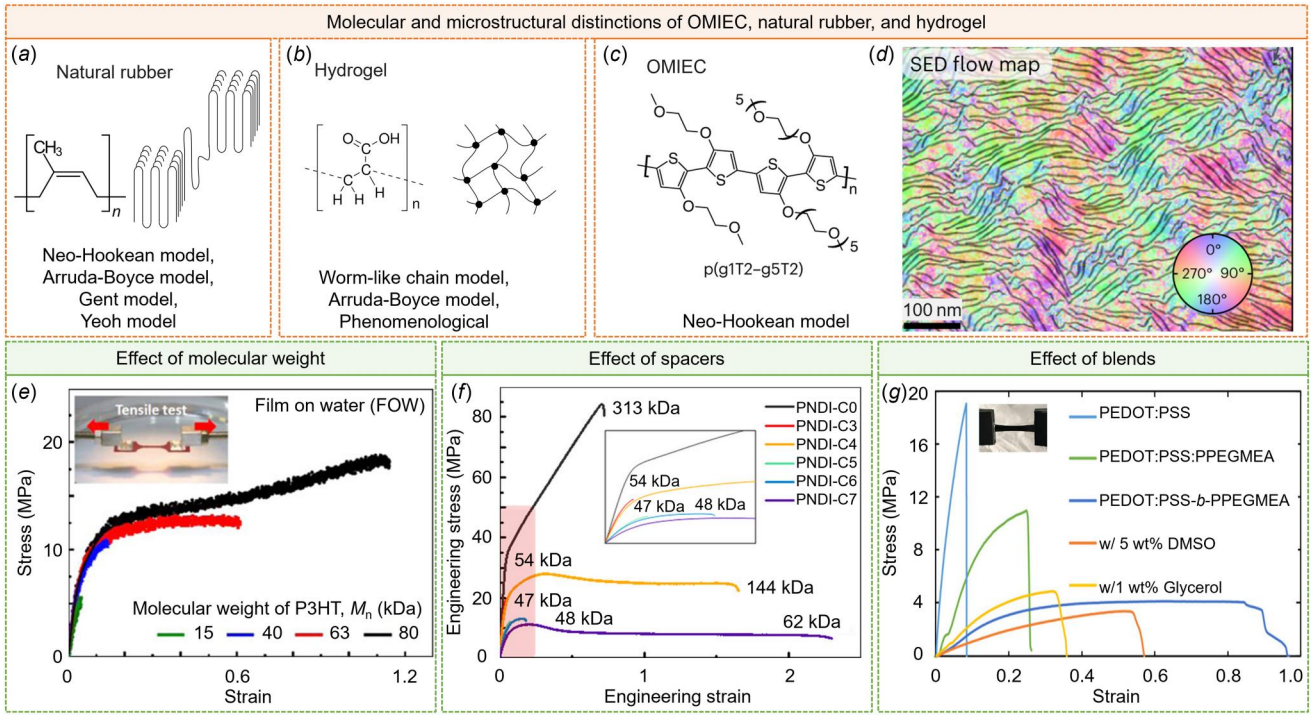

Fig. 20 Microstructural features of OMIECs in comparison with natural rubber and hydrogel. Representative molecular structures and schematic of microstructures of (*a*) natural rubber, (*b*) poly(acrylic acid) hydrogel, and (*c*) p(g1T2-g5T2) OMIEC. Flow lines in (*d*) represent the normal direction of the π–π stacking of the molecular chains. Reprinted with permission from Ref. [122]. Stress–strain curves of three representative OMIECs, highlighting the effect of (*e*) molecular weight in P3HT, reprinted with permission from Ref. [148], (*f*) spacers between conjugated units of PNDI, reprinted with permission from Ref. [166], and (*g*) blending of additives to PEDOT:PSS, reprinted with permission from Ref. [167].

for constitutive modeling of OMIECs. OMIEC molecular chains are often short (molecular weight of the order of 10–100 kDa), consisting of noncrosslinked, ring-structured backbone and side groups. Therefore, the microstructural assumptions for rubber and hydrogels are not fully applicable. Under mechanical stretching, conformation of the backbone changes, and complexity arises from the interchain interactions which are mostly weak van der Waals forces and intermolecular entanglements. Irreversible changes may be more significant and lead to earlier fracture compared to other crosslinked polymers. Recent 4D-STEM experiments on p(g1T2-G5T2) show the polymer flow map shown in Fig. 20(*d*), where the color coding corresponds to the spatial orientation of the polymer chain alignment and the intensity corresponds to the local diffraction intensity. The result indicates spatial heterogeneity in OMIEC polymers, consisting of crystalline domains surrounded by and tied to each other by amorphous domains [58]. In the following, we will highlight the effects of three aspects of the stress–strain behavior in OMIECs.

Molecular weight determines the chain length and material response to external load. Film-on-water tensile tests of P3HT thin films show a high stiffness response followed by a low stiffness shown in Fig. 20(*e*) [148]. Upon increasing the molecular weight from 15 kDa to 80 kDa, the tensile modulus of the polymer increases slightly from 0.203 GPa to 0.270 GPa, while the strength increases from 4.5 MPa to 17.1 MPa, and the strain at fracture increases from 4.5% to 95.6%. Coarse-grained molecular dynamics simulations show that in low molecular weight samples ($Mn = 15$ kDa), fracture occurs by chain pullout. Conversely, in high molecular weight samples ($Mn > 25$ kDa), entanglements concentrate the stress on a few chains and the chain scission becomes the dominant mode of fracture.

In parallel, disruption of the conjugation backbone by alkyl spacers does not change the molecular weight and the entanglement molecular weight (∼15 kDa) of polynaphthalene diimide (pNDI), however, the Kuhn length decreases from 521 Å for fully conjugated PNDI-C0 to 36 Å for PNDI-C6 [166]. Therefore, the stiffness of the conjugation of broken polymers decreases accordingly. These results suggest that the molecular structure, chain length, and local segment all contribute to the stress–strain response of OMIECs.

Another complication is due to chemical blending or electrochemical straining, for instance, with solvent absorption, deformation of the polymer network is localized at the amorphous regions by the large access to the hydrophilic side chain groups. The crystalline domains remain intact and the π–π stacking distance remains ∼3.5 Å. On the other hand, under electrochemical reactions, the backbone of the molecules is charged, and ions and solvents are inserted between the π–π stacking planes. The heterogeneous microstructure dictates the nonuniform deformation and history-dependent behaviors under various conditions. In one study, the composition of PEDOT:PSS is systematically varied to study its mechanical properties using tensile tests [167]. The base PEDOT:PSS film is stiff and brittle, showing <10% strain at fracture. When PEDOT:PSS is blended with PPEGMEA or the PSS is copolymerized with PPEGMEA, the polymer becomes more compliant and ductile. The change in the mechanical properties due to the blend and copolymerization informs different deformation mechanisms. Polar solvents such as DMSO and glycerol are known to induce phase segregation in PEDOT:PSS films, which also changes the ductility and stiffness of the polymer.

The above examples suggest a few principles in constitutive description of OMIECs. First, the stress–strain relationship highly depends on the molecular structure, including the molecular weight, chain rigidity, and side chain properties such as hydrophobicity and steric interactions. A slight change of the molecular chemical structure may drastically change the stress–strain response of the polymer. Second, postprocessing of conducting polymers modulates the microstructure, such as crystallinity, crystal domain distribution, and residual strains, all of which impact the deformation mechanism of OMIECs. Finally, the microstructure self-evolves upon deformation due to mechanical, chemical, and electrochemical straining factors. The necessity and approaches to incorporate such complexity of OMIECs present an active challenge to the research community.

4.3 Computational Modeling Integrating Multiphysics in Organic Mixed Ionic-Electronic Conductors. The multiphysics in OMIECs lead to many emerging applications as discussed in Sec. 1.1. Computational modeling integrating the relevant physical principles provides invaluable insights into the performance of metrics, structural dynamics, and degradation mechanism in conducting polymers and their devices. Following the discussion in the previous two subsections, we will use OECTs as an example to review continuum modeling of OMIEC-based devices including electric circuit models [168] and physics-based models [169].

Electric circuit models: Such models offer simple yet quantitative descriptions of electric characteristics of OMIECs under operation in a device. The conducting polymer is treated as a combination of electrical capacitors and resistors. For example, the Bernards model considers the OMIEC channel in an OECT as a series of circuits, which consist of a resistor and a capacitor series [168]. The resistor R_s resembles the semiconducting OMIEC, and the capacitor represents the double layer capacitance c_d. The circuit is subject to a gate voltage V_g and a voltage within the OMIEC $V(x)$. For a channel of length L, width W, and thickness T, the doping level at location x is defined by the electronic charge density c and the total charge Q in the region bounded by dx

$$\frac{c}{c_0} = 1 - \frac{Q}{ec_0 v} \tag{34}$$

where c_0 is the reference charge density, e is the elementary charge, and $v = WT\mathrm{d}x$ is the volume. In the steady-state, charges stored in the slice dx can be calculated by the applied voltage $(V_G - V(x))$ on the capacitor with capacitance $c_d W\mathrm{d}x$

$$Q(x) = c_d(V_G - V(x))W dx \tag{35}$$

and the charge flux along the channel is

$$J(x) = e\mu c_0 \left[1 - \frac{V_G - V(x)}{V_p}\right] \frac{\mathrm{d}V(x)}{\mathrm{d}x} \tag{36}$$

where μ is the charge mobility and $V_p = \frac{ec_0T}{c_d}$ is the pinch-off voltage upon which the current is saturated. Depending on the relative electrical potential of the gate and drain electrodes, the current flow can be calculated. Since the source electrode is grounded and $V_G > 0$ upon dedoping, the steady-state response is divided into three cases as shown in Fig. 21(*c*). First, when the entire OMIEC is dedoped

$$I = G\left(1 - \frac{V_G - 0.5V_D}{V_p}\right)V_D, \quad V_G > V_D > 0 \tag{37}$$

where $G = \frac{e\mu c_0 WT}{L}$ is the transconductance of the OMIEC channel. Second, dedoping occurs for regions where $V(x) < V_G$

$$I = G\left(V_D - \frac{V_G^2}{2V_p}\right), \quad V_D > V_G \tag{38}$$

when $V_D < 0$, complete dedoping might be possible and current approaches zero.

In the transient state, under a constant gate voltage, the capacitor characteristics requires

$$Q(t) = C_d \Delta V\left[1 - \exp\left(-\frac{t}{\tau_i}\right)\right] \tag{39}$$

where C_d is the total capacitance, ΔV is the voltage applied across the electrolyte, $\tau_i = C_d R_s$ is the characteristic time scale of the ionic

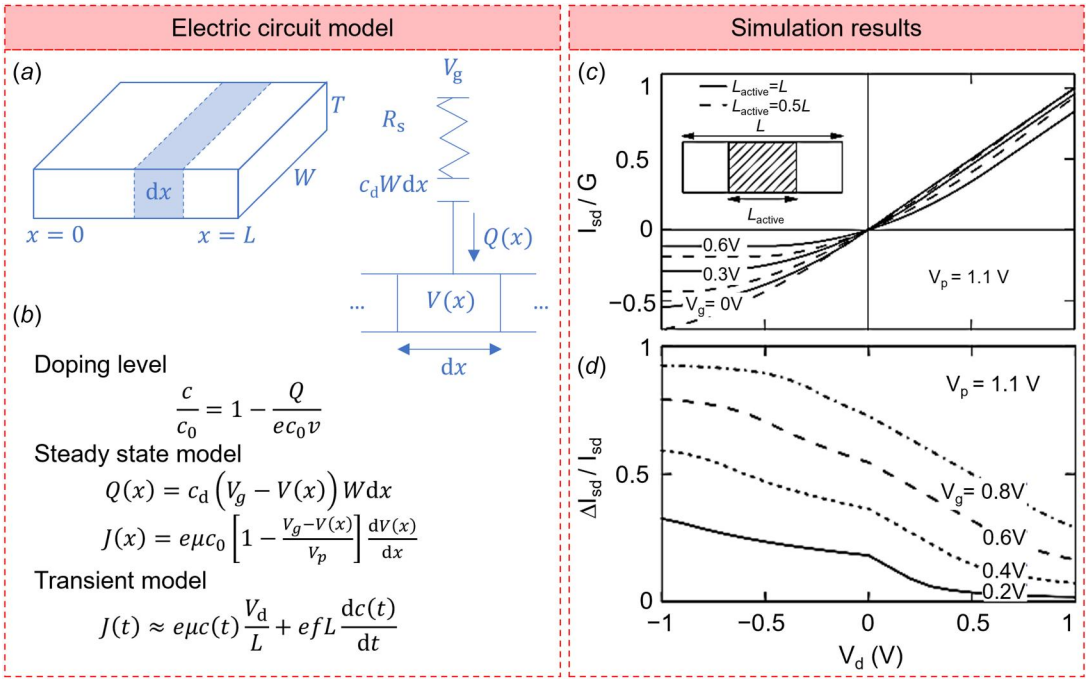

Fig. 21 An electric circuit model of OECTs. (*a*) Geometry of an OECT channel and the corresponding electric circuit model with the key equations shown in (*b*). Organic semiconductor film with the source is located at $x=0$ and the drain at $x=L$. Charge (Q) from the ionic circuit is coupled to the voltage in the electronic circuit at a position x along the organic semiconductor. (*c*) Simulated steady-state current–voltage characteristics for an ideal device geometry (solid lines) and for a device with an additional series resistance (dashed lines) at $V_p=1.1$ V. (*d*) Simulated steady-state current as a function of the drain voltage for a series of gate voltages at $V_p=1.1$ V, where I_{sd} is the source-drain current without an applied gate voltage and ΔI_{sd} is the change in source-drain current upon the application of a gate voltage. Reprinted with permission from Ref. [168].

circuit. Note the total charge that passes through the circuit is $C_d\Delta V$. The transient state charge flux across the channel is

$$J(t) \approx e\mu c(t)\frac{V_d}{L} + efL\frac{dc(t)}{dt} \tag{40}$$

where f is a factor that ranges from 0 to 0.5. The analytical solutions to the transient response can be derived for specific cases. For example, when dedoping occurs everywhere in the channel without the saturation effect, an average voltage drops between the channel and the gate electrode ($\Delta V = V_G - \frac{1}{2}V_D$) and can be selected to ensure that the transient behavior is consistent with the steady-state characteristics. Therefore, a simplified OECT can be described as

$$I(t, V_G) = I_{ss}(V_G) + \Delta I_{ss}\left(1 - f\frac{\tau_e}{\tau_i}\right)\exp\left(-\frac{t}{\tau_i}\right) \tag{41}$$

$$\Delta I_{ss} = I_{ss}(V_G = 0) - I_{ss}(V_G) \tag{42}$$

where $I_{ss}(V_G)$ is the steady-state current in the channel from the source to the drain, and $\tau_e = \frac{L^2}{\mu V_D}$ is the characteristic time scale of the electronic circuit.

Physics-based continuum models: Such models consider the multiphysics field in the space occupied by the OMIEC channel and the supporting electrolyte [24] and represent the electrodes by proper boundary and initial conditions. The solution to the initial- and boundary-value problems gives the charge distribution, current flow, mechanical deformation, and other field variables. Physics-based modeling is powerful. First, they work well for proper boundary values and initial conditions, which is more realistic than electric circuit models. Second and more importantly, they provide a powerful platform to study the multiphysics coupling and dynamics in the OMIEC materials, such as how molecular interactions change the interphase diffusion [170], how electrical stimuli at the gate change the ionic and electronic current, how charge redistribution causes mechanical deformation and microstructural evolution (e.g., phase separation), how mechanical deformation and stress impact the charge transport and current flow. Third, the physics-based models can describe the microstructural heterogeneity that governs a variety of processes at different scales, for example, local crystallinity impacts the swelling behavior [171,172] and kinetics of charge and mass transport [33], phase separation occurs in multiphase materials [31,102,173,174], and morphology changes that influence the tradeoffs between the charge transport and mechanical properties [34,175]. The seamless integration of the different physics modules fully captures the dynamic processes in heterogeneous OMIECs.

We introduced physics-based continuum modeling of OECT, which is represented by a two-domain geometry as shown in Fig. 22. The gate electrode is on the top of the electrolyte domain, and the source and drain electrodes are at two sides of the channel in the lower OMIEC domain. The electrolyte domain contains the variables of the concentrations of solvent C_s, cations C_c, anions C_a, and the electrostatic potential V, which are solved using the transport equations for the mobile species and the electrostatics. The OMIEC in the channel domain hosts variables of the concentrations of solvent C_s, cations C_c, holes C_h, the electrical potential V, the displacement $\boldsymbol{u}$, and the phase parameter ϕ, which are solved using the transport equations for the mobile species, evolution of the phase parameter, electrostatics, and the mechanics equations. Note that the phase parameter can be used in various scenarios to study the heterogeneous microstructure or heterogeneous properties of OMIECs. For OMIEC blends (PEDOT:PSS) or heterojunctions (P3HT:PCBM), the phase parameter can be the volume fraction of the components. For semicrystalline OMIEC, the phase parameter can represent crystallinity. For an OMIEC that might be damaged to lose its dual transport capability, the phase parameter can represent the damage parameter. For the boundary conditions, the electrode

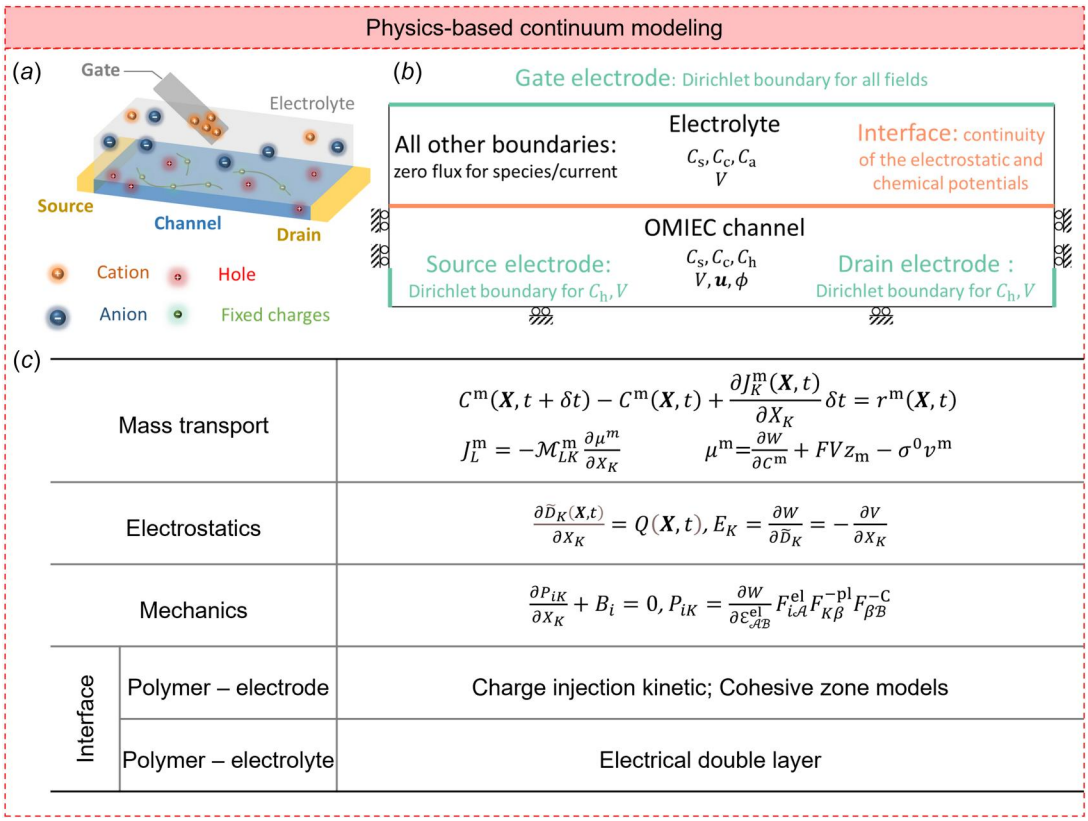

Fig. 22 Physics-based continuum modeling of an OECT. (*a*) Geometry of an OECT with the gate, source, and drain electrodes, along with the electrolyte and OMIEC channel. (*b*) Computational model of an OECT, where variables in the electrolyte domain include electrostatic potential, solvent, and ion concentrations, variables in the OMIEC domain include electrostatic potential, concentrations of solvent, ions, holes/electrons, displacement, and other parameters (such as phase parameter). The gate electrode on the top is specified as a Dirichlet boundary condition. The electrostatic and chemical potentials are continuous across the electrolyte/OMIEC interface. The hole/electron concentration and electrostatic voltage are specified with a Dirichlet condition for source and drain electrodes. All other boundaries are held at zero flux for all species. (*c*) Table of the key governing equations, including mass transport, electrostatics, and mechanical equilibrium. Special conditions may be applied at interfaces, such as charge injection kinetics and cohesive zone models at the OMIEC-current collector interface, and electrical double layer at the OMIEC-electrolyte interface. Reprinted with permission from Ref. [24].

voltage, ionic and electronic charge carrier concentration, and the solvent concentration can be specified at the three electrodes. When the OMIEC is mounted on a substrate, a cohesive zone model or fracture interface can be defined to study how mechanical breathing induces structural degradation at the interface [55]. The interface between the OMIEC and the electrolyte can be described by a free surface for mechanics modeling, and by a discontinuous interface for the mobile species and the electrical field due to the presence of the electrical double layer.

The multiphysics equations are briefly summarized in the following. The electrical field is determined by the electrical potential of electrodes and the space charge is determined by the mobile ions and electrons/holes. Flux of mobile charges is driven by the gradient of the electrochemical potential, which is related to their concentration and mechanical stress as

$$\mu^m = \frac{\partial W}{\partial C^m} + FVz_m - \sigma^0 v^m \tag{43}$$

where W is the Helmholtz free energy of the material, F is the Faraday's constant, z_m and v^m are the charge and molar volumes of the mobile charge carrier, respectively. σ^0 is the hydrostatic pressure, which is induced by deformation caused by transport species and solvents. The phase parameter can be used to regulate field evolution. For example, a change in the volume fraction of one component in an OMIEC blend may induce internal stresses that perturb the charge distribution. And the resulting electrical field may also cause the drift of the charged OMIEC molecules. Therefore, a perturbation in the field variables initiates a dynamic evolution of the system, until a new equilibrium is established.

We showcase one example of physics-based modeling, where the phase parameter represents the volume fraction of PEDOT in a PEDOT:PSS blend [24]. The source electrode is grounded, and the drain electrode is kept at $V_D = -0.1$ V. The voltage of the gate electrode changes as a trapezoidal waveform to allow the OMIEC channel in the OECT to be doped and dedoped to mimic the ON-OFF of a transistor. Plotted in Fig. 23(*a*) are the contours of the variables after 12 doping-dedoping cycles, including the local volume fraction of PEDOT ϕ, the electrostatic potential V, the hydrostatic pressure σ^0, the effective cation concentration $\frac{C_c(1-\phi)}{C_{h0}}$, the effective hole concentration $\frac{C_h\phi}{C_{h0}}$, and solvent concentration $\frac{C_s}{C_{s0}}$.

The distribution of the charge carriers is determined by the electrical field and the phase structure. With a negative gate voltage, holes are injected from the source electrode to the PEDOT phase while cations are expelled from the PSS phase to the electrolyte. At a positive gate voltage, holes are removed from the OMIEC, and cations are recovered. The inhomogeneous phase structure influences the spatial distribution of the electrostatic potential and the concentration of the charge carriers in the OMIEC. This is shown in the contour plots of the 12th doped state. In the PSS-rich region (smaller ϕ), the presence of the fixed charges reduces the local voltage. And cations are transported to the PSS-rich region driven by

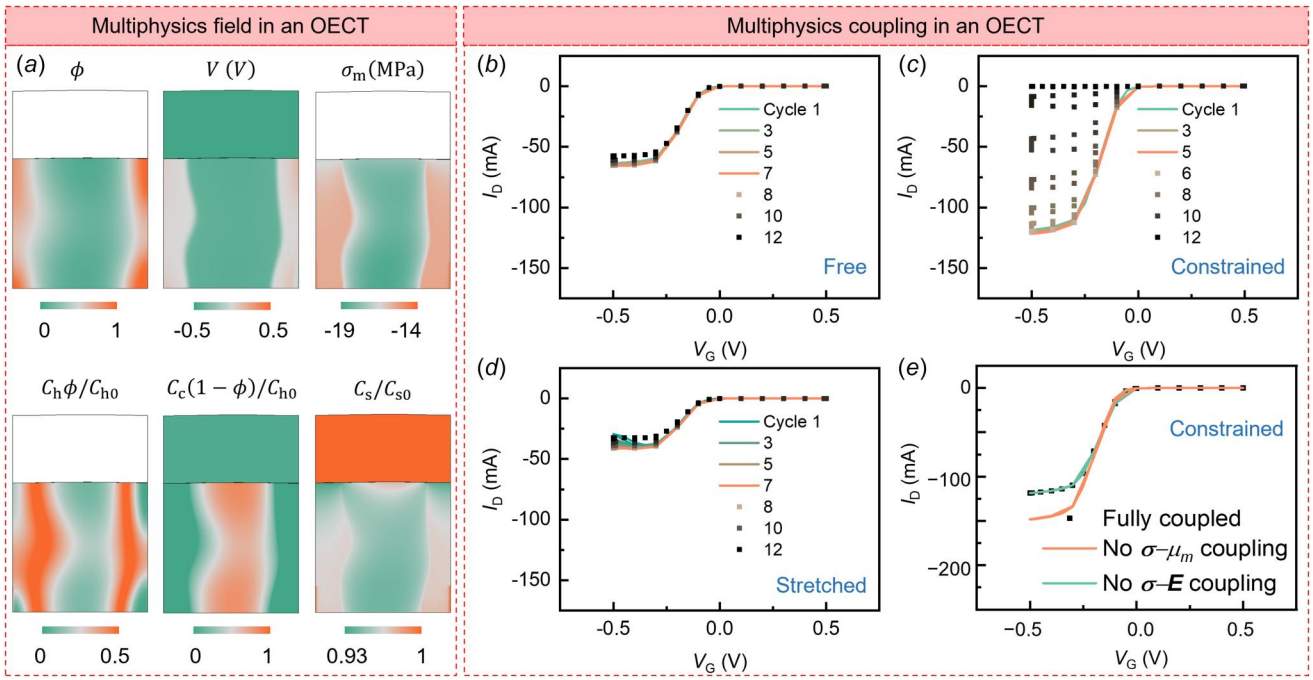

Fig. 23 Results from the physics-based continuum modeling of an OECT. (*a*) Contour plots of the local volume fraction of PEDOT ϕ, electrostatic potential V, hydrostatic stress σ_m, effective hole concentration $C_h\phi/C_{h0}$, effective cation concentration $C_c(1-\phi)C_{h0}$, and normalized solvent concentration in the OECT after 12 ON/OFF cycles. Transfer curves of the OECT in the first 12 ON/OFF cycles at the (*b*) free expansion state along the channel, (*c*) constrained state, and (*d*) stretched state along the channel direction. (*e*) Comparison of the transfer curves in the fully coupled model and that without considering the electromechanical coupling or the stress-transport coupling in the first ON/OFF cycle. Reprinted with permission from Ref. [24].

the electrical field. In the meantime, the effective hole concentration is much higher at the two-phase interfaces than that in the PEDOT-rich domain because of the low hole conductivity in the crystallized PEDOT domains. The excessive number of holes at the two-phase interface explains the origin of the so-called capacitive current in conjugated polymers.

One of the prominent features of OECTs is their ability to modulate the output current at the drain electrode using a small input voltage at the gate. To switch the OECT between the "ON" and "OFF" states for current modulation, we apply an alternating gate voltage from −0.5 to 0.5 V and a fixed drain voltage $V_D = -0.1$ V. The drain currents are plotted as solid lines in Fig. 23(*b*). The model successfully captures the current modulation between the ON-OFF states of an OECT. At negative gate voltages, the OMIEC is doped and the OECT is at the "ON" state which outputs a large current. Nevertheless, the drain current is nearly saturated when the gate voltage is beyond −0.5 V. At positive gate voltages, the OMIEC is dedoped and the OECT is turned off with a vanishingly small current.

Organic mixed ionic-electronic conductors present a vivid example of multiphysics coupling at the interface between mechanics and electrochemistry. As discussed above, material deformation due to electrochemical breathing and an external load modulates the phase evolution and eventually the OECT performance. For example, the OMIEC channel in the stretched and constrained states during 12 ON-OFF cycles are plotted in Figs. 23(*c*) and 23(*d*), in comparison to the free state in Fig. 23(*b*). The shape of the transfer curves is similar to those in Fig. 23(*b*) but the peak current in the "ON" state changes. The large-scale phase separation sets in during cycling and the current starts to drop due to its influence on the conducting path. For the constrained OECT, in-plane phase separation occurs and the PEDOT phase accumulates near the source and drain electrodes which causes a high mobility of the phase parameter in the horizontal direction. As a result, PSS-rich regions emerge in the middle of the channel and hinder the electronic conduction from the source to the drain electrode. Therefore, the drain current diminishes after the 12th cycle in Fig. 23(*c*) even at the negative gate voltage which would have turned the transistor on. For the free and stretched OECTs, the mobility of the OMICE is more homogeneous and the complete phase separation has yet to occur. The longer channel length for free and stretched OECTs requires a longer time for the transport of carriers from the source to the drain electrode and therefore the peak drain current is smaller than that in the constrained OECT.

The extent and significance of the coupling terms are discussed by studying the electromechanical coupling (Maxwell stress, represented by $\boldsymbol{\sigma} - \boldsymbol{E}$) and the stress-transport coupling (represented by $\boldsymbol{\sigma} - \mu^m$) in OECTs. By eliminating the Maxwell stress and the $\sigma^0 v^m$ terms in the chemical potential of the mobile species, the transfer curves of the OECT are compared. The model without $\boldsymbol{\sigma} - \mu^m$ coupling shows a higher peak current at the ON state. Notably, the model without the Maxwell stress shows little difference in both the mechanical and electrochemical responses from the fully coupled model.

4.4 Stress-Transport Coupling in Organic Mixed Ionic-Electronic Conductors. Among the multiphysics, here we highlight the stress-transport coupling as we observed in moving front experiments, which are often conducted to understand the doping kinetics in OMIECs. Figure 24 shows a modified electrochromic device [29] for moving front observation, consisting of stacking layers of an OMIECs thin film (PProDOT), a gel electrolyte for ion conduction, a counterelectrode for charge balancing, and indium-tin oxide (ITO)-coated glass substrates as current collectors. An in situ optical microscopy is used to observe the time evolution of the moving front. With an applied voltage of 1 V, the PProDOT film in contact with the gel electrolyte is doped with holes/anions and bleached to transmissive light blue. The redox carriers move toward the pristine magenta domain ahead of the moving front on the right. The microscopic images (scale bar 100 μm) in Fig. 24(*b*) captured at 0, 1 h, and 10 h show the propagation of the front. The front

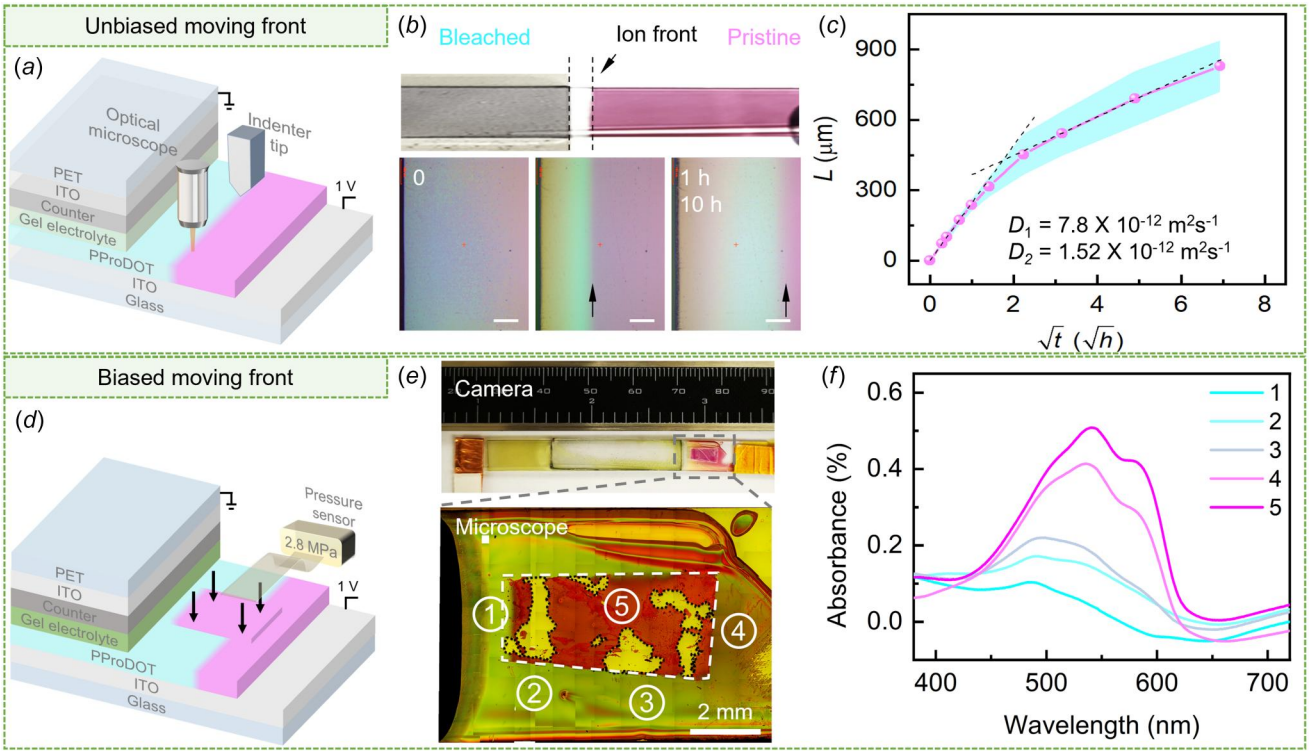

Fig. 24 Moving front experiments to demonstrate stress-transport coupling in OMIECs. (*a*) Schematic of the moving front experiment to study doping kinetics. (*b*) Camera photos (upper panel) and optical microscopy images (lower panel) at 48 h and snapshots at 0, 1 h, and 10 h of the PProDOT film under 1 V bias voltage. The scale bar is 100 μm. (*c*) Moving front displacement as a function of the square root of time. (*d*) Schematic of the pressure-biased moving front experiment. (*e*) Camera photos and an optical image of the sample showing the contrast between the doped and undoped regions under pressure. (*f*) Absolute absorbance across the visible spectrum for five locations labeled in (*e*). Reprinted with permission from Ref. [29].

propagation length L is defined as the distance from the ion source to the front position as seen visually from the microscopic images. As expected, the front displacement L follows a bilinear relationship against the square root of time, indicating the diffusional characteristic of the front propagation.

The strong stress-transport coupling is demonstrated in Fig. 24(*d*). A pressure is applied to the film and the voltage is applied as normal to observe the front propagation. The region in direct contact with the electrolyte is completely bleached to transmissive light blue, and the moving front continues to propagate toward the undoped domain. For the pressured region, as seen in the camera photo-and circled by the white dashed box in the microscope image in Fig. 24(*d*), a clear color contrast is presents compared to the pressure-free region. The PProDOT film within the irregular regions outlined by the black dots is peeled off when the PET-PE plate is removed, leaving the bare ITO coated glass visible. The color change and film absorbance are further quantified by the UV–VIS spectroscopy at five different locations in the film, covering the pressured and stress-free regions, as shown in Fig. 24(*e*). The result shows that at locations 1, 2, and 3, where the color is light, the absorbance is low or intermediate, implying that the moving front has passed through. In contrast, in the pressured region 5, the absorbance is very high, on par with the absorbance of pristine PProDOT magenta films. This indicates that the mobile ions have not yet reached the region in magenta and the doping process has not started. Region 4 has the second-highest absorbance among all. Overall, we observe that an applied pressure as low as 2.8 MPa can significantly retard the electrochemical redox reaction. While the doping level is estimated to alter the ionic diffusivity by ~300 times, the mechanical stress has a comparable effect on ionic transport. Detailed theoretical modeling on the doping kinetics of PProDOT under stress and finite element analysis on the moving front experiments can be found in Ref. [29].

5 Mechanics-Focused Design Strategies for Materials and Interface

Following extensive discussion on strain activation, mechanical properties, dynamics and heterogeneity, multiphysics coupling, and continuum modeling of materials and devices of OMIECs, this section reviews design strategies to regulate the mechanical response of OMIEC polymers. We categorize the solutions into four classes: (1) strain modulation through backbone design, side group engineering, and postprocessing, (2) enhancement of material stretchability through molecular, intermolecular, and microstructural engineering, (3) optimization of chemical environment to harvest/suppress mechanical breathing of OMIECs in the conduction process, and (4) interfacial engineering through chemisorption and physisorption.

5.1 Strain Activation. This section explores strategies for tailoring strain activation, emphasizing the multiscale approaches. The material design strategies are developed in terms of the backbone, sidechain polarity, length, regiochemistry, and post-processing. The backbone crosslink density and molecular weight are effective tuning knobs for controlling strain activation. A higher crosslinking ratio yields a stiffer network with lower electrolyte uptake and reduced irreversible network expansion. For example, in polypyrrole (PPy) derivatives, beta substitutions of the methyl group deactivate the crosslinking sites (Fig. 25(*a*)) [176], leading to progressively higher electrolyte uptake and larger irreversible expansion. Note that the relatively lower expansion of poly (3,4DMPy-Py)(DBS) compared to poly(3MPy-Py)(DBS) at low substitution fractions is attributed to film fracture and delamination. Regarding the molecular weight, it determines the packing and microstructure, which both impact the electrolyte uptake. As shown in Fig. 25(*b*), increasing the molecular weight of P3MEEET from

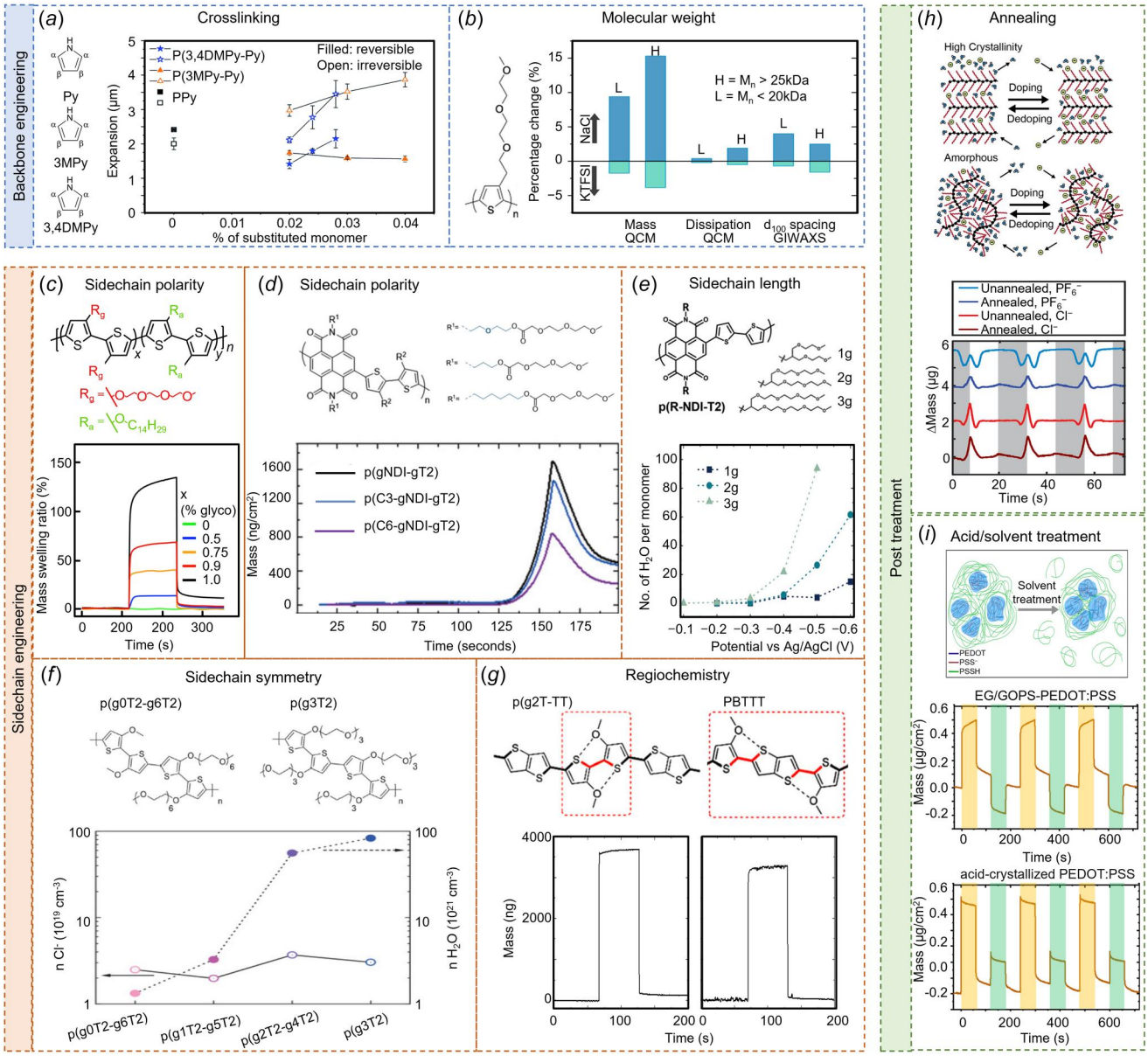

Fig. 25 Polymer design strategies to tune strain activation. (*a* and *b*) Backbone engineering. (*a*) The maximum reversible (filled symbols) and irreversible (open symbols) volume expansions as a function of fractional amount of substitution in pyrrole (PPy), beta-substituted 3-methyl-1H-pyrrole (P(3MPy-Py)) and 3,4-dimethyl-1H-pyrrole (P(3,4DMPy-Py)). Reprinted with permission from Ref. [176]. (*b*) Percentage changes of mass, dissipation, and lamellar stacking spacing (d_{100}) during doping of low (L) and high (H) molecular weight poly(3-[2-(2-methoxyethoxy)ethoxy]ethylthiophene-2,5-diyl) (P3MEEET). Reprinted with permission from Ref. [177]. (*c–g*) Sidechain engineering. (*c*) Mass changes during doping in *x*-p(gT2):*y*-p(aT2) copolymers, where *x* is the ratio of polar triethylene glycol and apolar alkoxy side chain. Reprinted with permission from Ref. [178]. (*d*) Mass changes during doping of naphthalene diimide-bithiophene (NDI-T2) copolymer functionalized with hybrid alkyl-glycol side chains. Reprinted with permission from Ref. [179]. (*e*) Chemical structure of NDI-T2 copolymer and sidechain variants and their water uptake as a function of the potential. Reprinted with permission from Ref. [103]. (*f*) Chemical structure of p(g0T2-g6T2) and p(g3T2) with asymmetric and symmetric sidechain distribution, and numbers of Cl^- and water uptake. Reprinted with permission from Ref. [112]. (*g*) Regiochemically different poly(2-(3,3′-bis(2-(2-(2-methoxyethoxy)ethoxy)ethoxy)-[2,2′-bithiophen]-5-yl)thieno[3,2-b]thiophene) (p(g2T-TT)) and poly(2-(4,4′-bis(2-methoxyethoxy)-5′-methyl-[2,2′-bithiophen]-5-yl)-5-methylthieno[3,2-b]thiophene) (pgBTTT), and their corresponding temporal mass change upon doping. Reprinted with permission from Ref. [111]. (*h–i*) Post-treatment. (*h*) Schematic of ion distribution and temporal mass changes of unannealed amorphous and annealed crystallized P3MEEMT. Reprinted with permission from Ref. [171]. (*i*) Schematic of morphological transformation of PEDOT:PSS after solvent treatment, and the temporal mass changes of EG-GOP PEDOT:PSS and acid-crystallized PEDOT:PSS upon doping (green shaded regions, smaller mass change) and dedoping (yellow shaded regions, larger mass change). Reprinted with permission from Refs. [180] and [181].

13.9 to 32.5 kg/mol shifts the microstructure from chain-extended crystals to interconnected lamellae inside amorphous regions [177]. In a NaCl aqueous electrolyte, high molecular weight P3MEEET exhibits more pronounced swelling, attributed to anion injection into amorphous regions which is evidenced by greater mass gain, increased dissipation, and smaller lamellar spacing changes. By contrast, low molecular weight P3MEEET swells less, and electrolyte accommodation within its highly crystalline region is more difficult. In a KTFSI aqueous electrolyte, high molecular weight P3MEEET demonstrates larger mass loss, driven by cation expulsion, along with larger dissipation and lamellar spacing changes. Despite the dependence on electrolytes, the observations

underscore that tuning molecular weight is an effective strategy for tailoring breathing strain in OMIECs.

Sidechain engineering includes tuning the side chain polarity, sidechain length, and regiochemistry. Side chain polarity is a commonly used strategy for OMIECs in aqueous electrolytes. Apolar alkyl side chains are hydrophobic, limiting water uptake during doping and dedoping. Conversely, polar side chains, such as ethylene glycol sidechain, significantly boost water absorption due to their hydrophilic characteristics. Breathing strain can thus be fine-tuned by synthesizing copolymers with varying ratios of apolar to polar side chains. As exemplified in Fig. 25(*c*), 0%-p(gT2):100%-p(aT2) with entirely apolar side chains show minimal swelling, whereas 100%-p(gT2): 0%-p(aT2) with purely polar side chains exhibits the largest swelling [178]. Varying the spacer length within polar side chains can also tailor the chain polarity. As shown in Fig. 25(*d*), p(gNDI-gT2) with no apolar spacer in the side chain, exhibits the largest swelling, while p(C6-gNDI-gT2), with the longest spacer, shows the lowest swelling due to reduced sidechain polarity [179]. Polar sidechain length determines the proportion of hydrophilic segments and influences the lamellar packing motifs, thus affecting breathing strain. For example, naphthalene-1,4,5,8-tetracarboxylic-diimide-bithiophene (NDI-T2) polymers with longer EG sidechain, such as p(3 g-NDI-T2), exhibit considerably greater swelling than their shorter chain counterparts [103] as shown in Fig. 25(*e*). OMIECs with the same average sidechain length but different sidechain symmetry or distribution display markedly different breathing strains, Fig. 25(*f*). For instance, p(g3T2), featuring symmetric side chains, swells much more than p(g0T2-g6T2) whose asymmetric sidechain arrangement reduces overall hydrophilicity and thus lowers breathing strain [112]. Regiochemistry refers to sidechain positioning that influences the intermolecular packing and the electrolyte accessibility of OMIECs. Comparison of p(g2T-TT) and pgBTTT in Fig. 25(*g*)— two OMIECs with the same backbone and sidechain but different sidechain placements—reveals dissimilar breathing strains [111]. The sulfur-oxygen interactions in pgBTTT yield a more planar structure and tighter packing, restricting electrolyte penetration.

Post-treatment of OMIECs can tune mechanical breathing by modulating their composition, morphology, and microstructure. Thermal annealing, for instance, increases polymer crystallinity, affecting passive and active swelling, Fig. 25(*h*). Unannealed amorphous P3MEEMT exhibits more pronounced passive swelling compared to its annealed, highly crystalline counterpart [171]. During subsequent doping (grey regions) in KPF_6 and KTFSI aqueous electrolytes, the unannealed P3MEEMT undergoes dehydration followed by anion uptake; the annealed P3MEEMT instead predominantly exhibits anion uptake with minimal dehydration. Similarly, acid or polar solvent treatment removes excess PSS^- and induces nanofibrillar crystallization in PEDOT:PSS [180]. The compositional and morphological differences lead to distinct swelling behavior as shown in Fig. 25(*i*) [181] where EG/GOPS treated PEDOT:PSS undergoes mass decrease due to cation expulsion, while acid-crystallized PEDOT:PSS experiences a mass increase caused by concurrent cation ejection and anion injection.

5.2 Material Stretchability. The rise of soft and wearable electronics calls for stretchable OMIECs. The stretchability of OMIECs originates from the hierarchy of the structural characteristics—spanning from the molecular structure, intermolecular interactions, to the microscopic and bulk-level structural design and postprocessing.

At the molecular level, the molecular structure including the rigidity of the backbone and length of side chains determines the extent of entanglement and chain slipping, which are the ladders of stretchability. The conjugated breaking spacers shown in Fig. 20(*f*) are a great example. The alkyl spacers significantly decrease the backbone rigidity, which allows more conformational changes of the OMIEC during deformation, and thus higher stretchability. Another effect of molecular structure is the ability of OMIECs to crystallize and its impact on morphology. For example, the indacenodithiophene-cobenzothiadiazole (IDTBT) polymer with rigid backbone is found to have much higher stretchability than the softer thieno[3,2-b]thiophene-diketopyrrolopyrrole (DPPTT) [182], Figs. 26(*a*) and 26(*b*). Microstructural analysis shows that IDTBT is amorphous and DPPTT is semicrystalline. The stretchability comes from the large free volume of polymer chains which helps dissipate the strain energy. Also, IDTBT polymer chains are observed to be better aligned during stretching, which contributes to the stretchability.

The intermolecular forces such as hydrogen bonding and covalent dynamic bonds can also be introduced to increase stretchability. For example, conjugation breakers with different H-bonding units (urea, amide, and urethane) and linker flexibilities (alkyl or ether chains) are incorporated into a diketopyrrolopyrrole (DPP)-based conjugated polymer backbone [183], Figs. 26(*c*) and 26(*d*). The two parameters can effectively tune the intermolecular interactions and the size and distribution of the H-bonding zones. Results show that with increased H-bonding energies, the material stretchability is enhanced. Further investigation of the relative degree of crystallization shows that the main energy dissipation mechanism for the H-bonding embedded polymers is the breakage of H-bonding interactions. By contrast, other less stretchable polymer films dissipate the strain energy through breakage of crystalline domains.

At mesoscale, the microstructure effectively changes the strength and ductility of OMIECs. This can be achieved by modulating the crystallinity and distribution of the crystalline domains using postprocessing, such as thermal annealing, and blending OMIECs with other stretchable polymers. When doped with p-dopant 2,3,5,6-tetrafluoro-7,7,8,8-tetracyanoquinodimethane (F4TCNQ), p(g32T-T) polymer showed significant increase in both the stretchability and stiffness, which agrees with the effect of doping induced π-stacking of the polymer [184], Fig. 26(*e*). Blending p(g2T-T)with hydrogel forming acrylic acid following crosslinking of hydrogels leads to a highly stretchable hydrogel OMIEC [185], Fig. 26(*f*). Leveraging the crosslinking ratios of the hydrogel, the overall stretchability of the hydrogel OMIEC can be increased to over 100%.

At the macroscopic level, structural design induces heterogeneous components that distribute deformation and enhance stretchability. For instance, a honeycomb porous structure [186] of poly (2,5-bis(2-octyldodecyl)-3,6-di(thiophen-2-yl)-2,5-diketo-pyrrolopyrrole-alt-2,5-bis(3-triethyleneglycoloxy-thiophen-2-yl) (DPP-g2T) with a biaxially prestretched platform is designed, Fig. 26(*g*). The hetero-structure distributes the load and stabilizes the effective electronic and ionic transport pathways under deformation, leading to OECTs with a high normalized transconductance and stable output characteristics. Eventually, material failure initiates from local breaking of the honeycomb lattice. By adding the ethylene-glycol side chains, the structural stretchability is further increased by one-fold as shown in Fig. 26(*h*).

5.3 Optimization of Chemical Environment to Harvest/Suppress Strain Response. The solvation structure of electrolytes largely affects the strain response of OMIECs. In this section, we discuss the selection and design strategies of aqueous and organic electrolytes, focusing on the effects of salt concentration, ionic size, and organic solvent. Our discussion is within the dilute electrolytes since high salt concentrations increase viscosity, slowing ionic transport. In dilute electrolytes, ions mainly move with their solvation sheath instead of cation-anion pairs, leading to larger breathing strains. For example, PBDF in a lower concentration NaCl aqueous electrolyte exhibits larger passive swelling due to amplified osmotic pressure [54], and larger breathing strains persist in the subsequent electrochemical cycles as shown in Fig. 27(*a*). Similarly, PProDOT in dilute organic electrolytes experiences more pronounced breathing strain as revealed by MD simulations and in situ nano-indentation (Fig. 27(*b*)) [22], driven by enhanced PC uptake. The inset MD snapshots of Fig. 27(*b*) show visualization, and the radial distribution function in Fig. 27(*c*) validates larger injection of

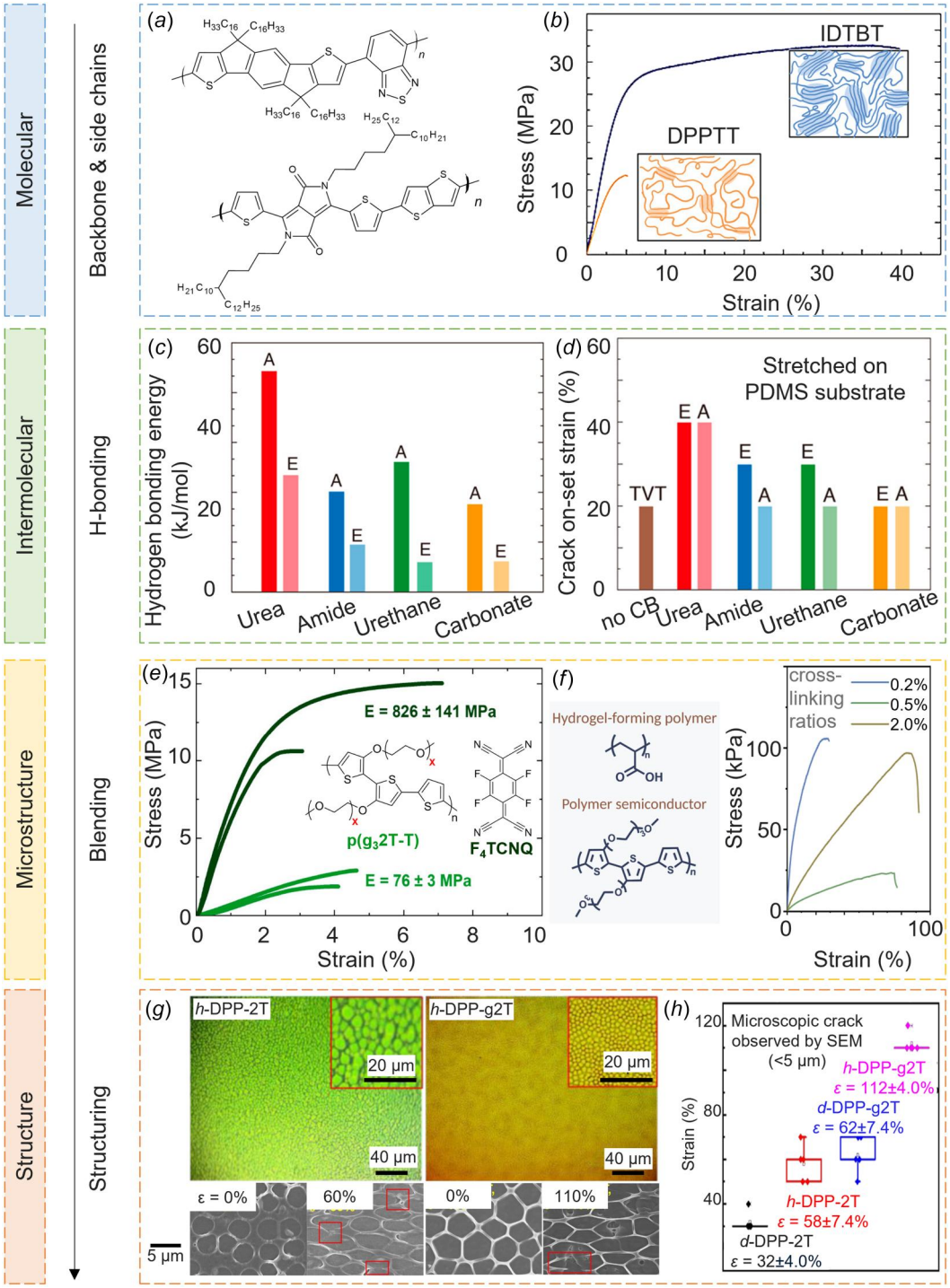

Fig. 26 Design strategies to enhance material stretchability. (*a* and *b*) Molecular backbone and sidechain engineering. Reprinted with permission from Ref. [182]. (*a*) Molecular structure of indacenodithiophene-co-benzothiadiazole (IDTBT) and thieno[3,2-b]thiophene diketopyrrolopyrrole (DPPTT). (*b*) Stress–strain curves for IDTBT and DPPTT. (*c* and *d*) H-bonding. Reprinted with permission from Ref. [183]. (*c*) H-bonding energy for different conjugation breakers (CBs) from DFT calculations. (*d*) Summarized crack on-set strains for different H-bonding polymers. (*e*–*f*) Blending. (*e*) Stress–strain curves recorded by tensile deformation of free-standing films of neat p(g32T-T) (light green, E = 76 MPa) and p(g32T-T) doped with 20 mol.% F4TCNQ (dark green, E = 826 MPa). Reprinted with permission from Ref. [184]. (*f*) Stress–strain curves of p(g2T-T): AAc hydrogel semiconductors (hydro-SCs) films with different cross-linking ratios measured in 100 mM NaCl solution. Reprinted with permission from Ref. [185]. (*g*–*h*) Structural engineering. Reprinted with permission from Ref. [186]. (*g*) Optical (top) and SEM (bottom) images of h-DPP-2T (left) and h-DPP-g2T (right) films at the pristine and stretched states. The inset shows a zoomed-in view of the images. The red squares highlight cracks. (*h*) Microscopic crack onset strains extracted from SEM imaging. All data are calculated from five samples.

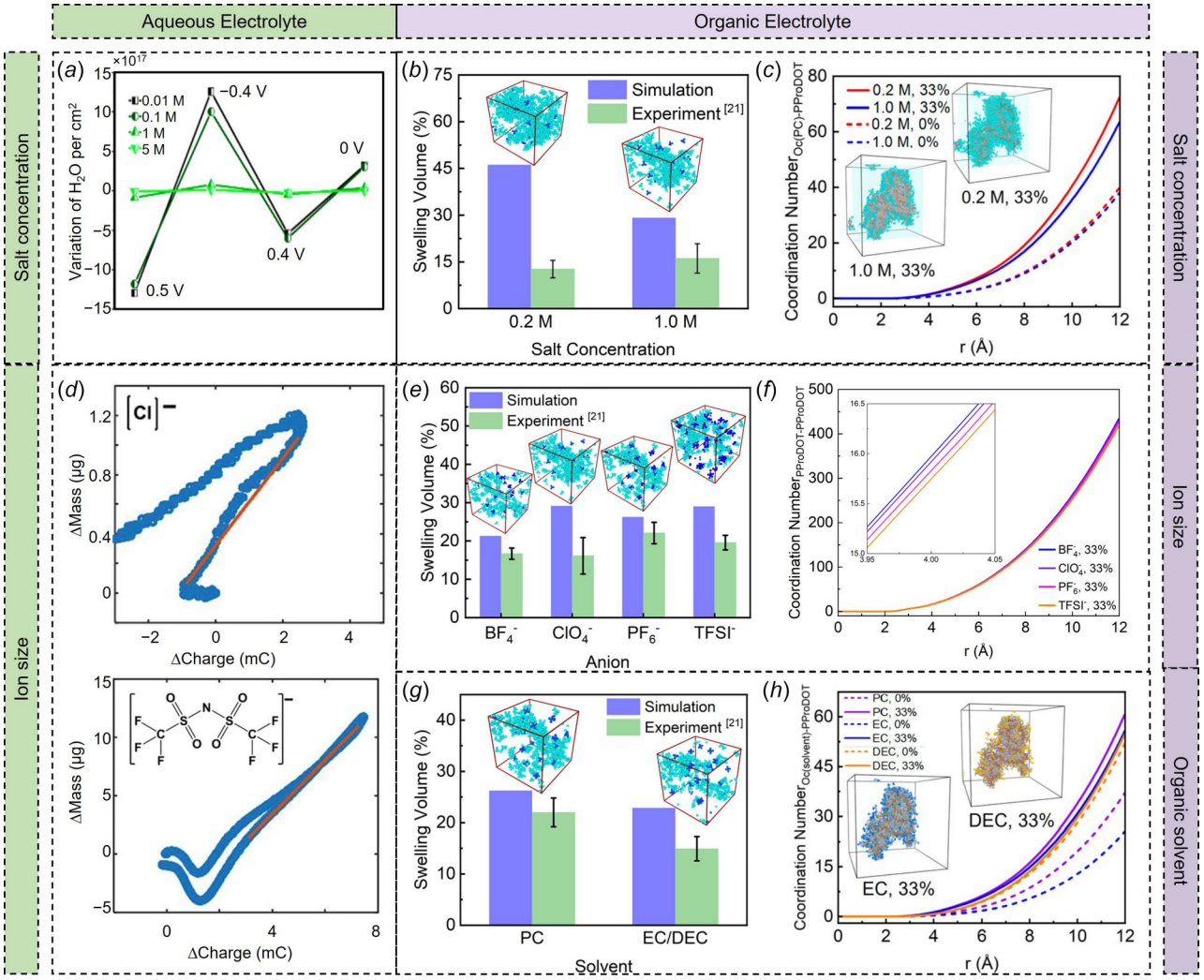

Fig. 27 Selection of electrolytes to tune mechanical breathing strain. (*a*–*c*) Salt concentration. (*a*) Water uptake of poly (benzodifurandione) (PBDF) films in NaCl aqueous electrolytes with varying salt concentrations upon doping and dedoping. Reprinted with permission from Ref. [54]. (*b*) Swelling volumes of PProDOT in 0.2 M and 1.0 M $LiClO_4$ in PC from MD simulations (blue) and in situ nano-indentation (green). (*c*) Coordination number between carbonyl oxygen (Oc) and PProDOT atoms at passive swelling (0%) and active swelling (33%) states. The inset figures are MD snapshots showing coordination of PProDOT with PC molecules. (*d*–*h*) Ion size. (*d*) Mass changes of P3HT as a function of charge consumed (blue) in a redox cycle with KCl (upper) and KTFSI (lower) aqueous electrolytes. Reprinted with permission from Ref. [187]. (*e*) Swelling volumes of PProDOT in 1.0 M $LiBF_4$, $LiClO_4$, $LiPF_6$, and LiTFSI in PC from MD simulations (blue) and in situ nano-indentation (green). (*f*) Coordination number between PProDOT atoms at the doped state in the four electrolytes. The inset figure shows the enlarged region between 3.95 and 4.05 Å. (*g*–*h*) Organic solvent. (*g*) Swelling volumes of PProDOT in 1.0 M $LiPF_6$ in PC and EC/DEC from MD simulations (blue) and in situ nano-indentation (green). (*h*) Coordination number between Oc in organic solvent and PProDOT atoms at passive swelling (0%) and active swelling (33%) states. The inset figures are MD snapshots showing coordination between PProDOT and EC/DEC molecules. (*b*–*c*, *e*–*f*, *g*–*h*) are reprinted with permission from Ref. [22].

PC which contributes to the increased swelling in the dilute electrolyte.

Ionic size also plays a critical role in determining the swelling behavior of OMIECs, particularly in aqueous electrolytes where ions are categorized as either small, hydrophilic, kosmotropic or large, hydrophobic, and chaotropic. As illustrated in Fig. 27(*d*), P3HT exhibits a substantial mass change in $TFSI^-$ based electrolyte where mostly isolated $TFSI^-$ are injected, compared to Cl^- based electrolyte despite Cl^- enters the film with a bulkier hydration shell [187]. Although the mass change does not directly quantify the breathing strain without the knowledge of mixture density, this contrast still highlights the importance of ionic size in regulating strain activation of OMIECs. In organic electrolytes, PProDOT also demonstrates greater swelling with larger ions with comparable solvent injection [22], visualized by MD snapshots in Fig. 27(*e*) and validated by radial distribution function between PProDOT atoms shown in Fig. 27(*f*). For organic solvents, PProDOT swells more in PC electrolyte than EC/DEC mixture as revealed in Fig. 27(*g*). In EC/DEC electrolyte, both EC and DEC contribute to the swelling, validated by the increased coordination with PProDOT after doping and by the MD snapshots shown in Fig. 27(*h*). The molar volume of EC/DEC is smaller/larger than that of PC. The resulting number averaged volume of injected EC and DEC remains smaller than that of injected PC, resulting in less breathing strain. It is noteworthy that material design and electrolyte selection can be combined. In such synergistic scenarios, breathing strain may differ significantly compared to the cases where these strategies are applied separately as shown in Fig. 25(*b*). Moreover, besides the breathing strain at the static state, the temporal evolution of swelling—illustrated in Fig. 25(*h*)—is important to understand the dynamic interactions of ions and solvents with OMIECs.

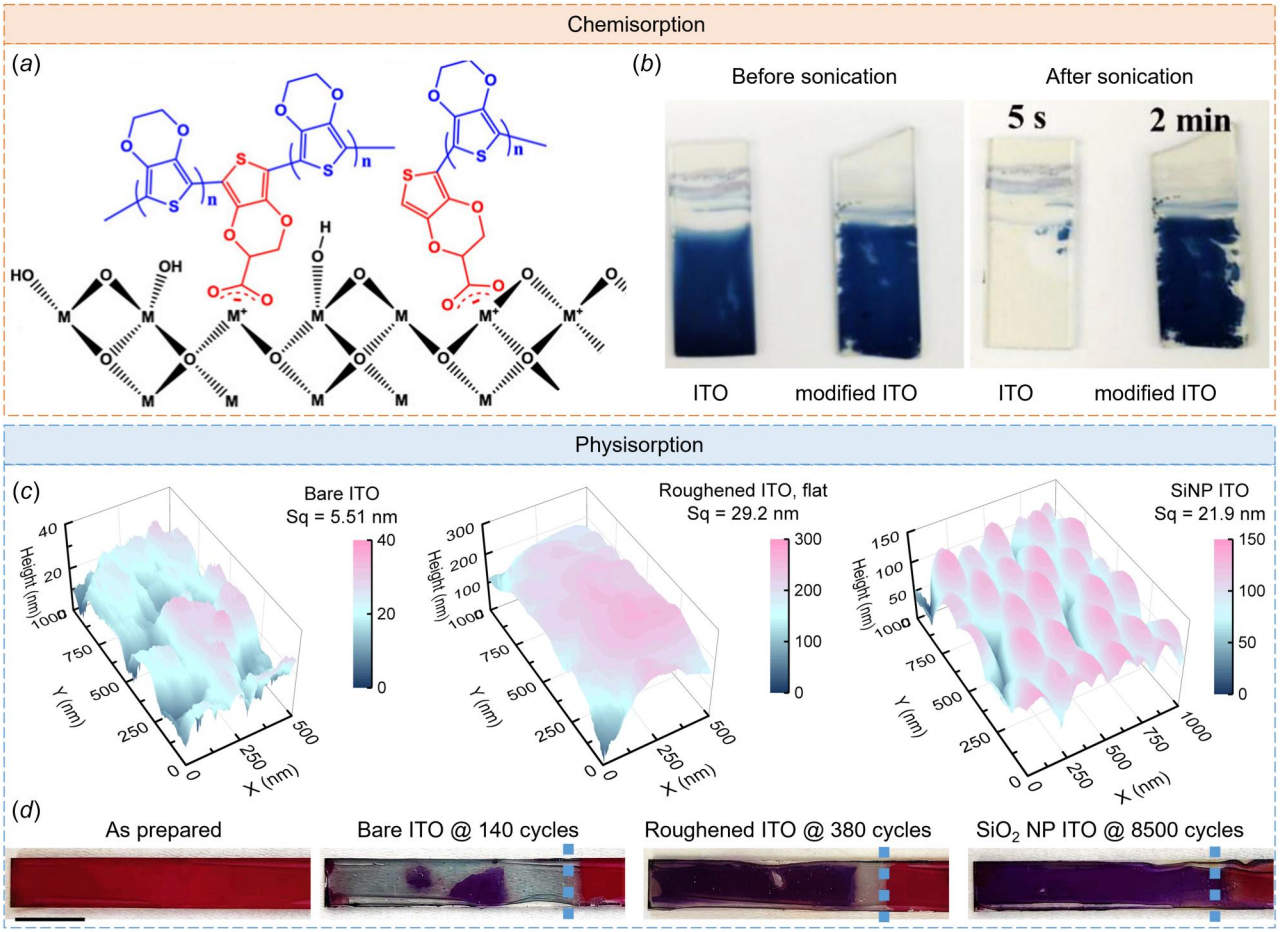

Fig. 28 Strategies to enhance interfacial stability. (*a* and *b*) Chemisorption. Reprinted with permission from Ref. [188]. (*a*) Chemisorption of EDOT-Acid (red, linker monomer) onto ITO (black, metal oxide base) and electrodeposition of PEDOT (blue, polymer). (*b*) Optical images of PEDOT films on ITO and modified ITO before and after ultrasonication adhesion tests. PEDOT on ITO is tested for 5 s and PEDOT on modified ITO is tested for 2 min. (*c* and *d*) Physisorption. Reprinted with permission from Ref. [55]. (*c*) Surface roughness of PProDOT thin films on different substrates including bare ITO, a flat region in roughened ITO, a scratched region in roughened ITO, and a SiO_2 NP-treated ITO. Sq denotes the root-mean-square height roughness. (*d*) Images of as-prepared PProDOT films on bare ITO, PProDOT on bare ITO after 140 cycles, PProDOT on roughened ITO after 380 cycles, and PProDOT on SiO_2 NP treated ITO after 8500 cycles. The cyan dotted lines indicate the electrolyte front. Scale bar is 1 cm.

5.4 Interfacial Stability. In OMIEC-based devices, the passive and active swelling of conducting thin films is usually bounded by the underneath inactive substrate, such as the current collector ITO. This mismatch induces mechanical stresses in both the film electrode and the substrate. The growth of the internal stress in the organic film as well as the interfacial stress between the soft polymer and the hard substrate can cause bending of the thin double layer, wrinkling of the film electrode, crack at the interface, and debonding of the thin film from its electron conduction network.

Previous efforts in modifying the interfacial adhesion fall into two major categories, chemisorption [188–190] and physisorption [55,191]. In general, chemosorption starts by activating the substrate surface with functional groups, which are ready to covalently link to the polymer chains. Chemisorption of EDOT-Acid (Red) onto ITO (black) substrate followed by electrodeposition of PEDOT showed a significant enhancement of PEDOT thin film adhesion, Figs. 28(*a*) and 28(*b*). The modified thin film remained mostly intact on the substrate after sonication for two minutes, while the untreated thin film was delaminated completely in five seconds. Other examples include electrografting of the amine moieties followed by in situ electrodeposition. Chemosorption is often the strongest to maintain electrical conductivity. However, in situ electrodeposition limits the generalizability of the method.

Physisorption methods enhances interfacial adhesion by increasing the roughness of the substrate surface before polymer coating, Figs. 28(*c*) and 28(*d*). We demonstrated two facile methods of enhancing physisorption: scratching the substrate with sandpaper and coating it with nanoparticle monolayers [55]. The base ITO interface with roughness of 5.51 nm shows a large dysfunctional area without electrochromic color switching due to interfacial delamination, while the roughened ITO surface and the silica nanoparticle coated ITO surface of >20 nm roughness enable orders of magnitude increase in the lifetime of a thin film OMIEC electrode with minimal change in the electrochromic functionality, indicating the intact interface.

6 Conclusions

Organic mixed ionic-electronic conductors are a fast-evolving field, and the mechanics associated with mixed conduction must be understood for their deployment in energy, biotechnology, and computing. Built upon extensive studies on OMIECs in the past decade and knowledge of similar materials such as polyelectrolytes and hydrogels, this review summarizes the key elements of mechanics in OMIECs, including strain activation, mechanical properties and mechanics descriptions, multiphysics coupling, and mechanics-guided design for durable electrochemical devices. The key features underlying these topical themes are the dynamics and heterogeneity that spans over multiple time and length scales as shown in Fig. 29.

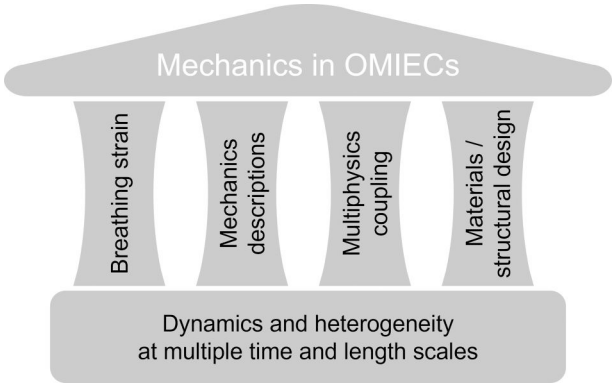

Fig. 29 The central elements of mechanics research in OMIECs

This section concludes the review by reiterating some of the outstanding questions, and outlining the remaining challenges at the interface between mechanics and electrochemistry where continued research could contribute to the fundamental understanding and practical adoption of OMIECs.

How does the strain response populate in OMIECs from molecules to devices? More specifically, (i) How do the chain structure and local chemical environment shape conformational changes at the molecular scale? The conformation and coordination of OMIEC chains are complex, depending on the chain structure (rigidity and hydrophilicity) and the chemical environment such as the electrolyte (salt, solvent, molarity). Future characterizations at the molecular level would heavily rely on scattering techniques, scanning tunneling microscopy [192], and electron microscopy [193] as well as molecular dynamics simulations. (ii) How does microstructural heterogeneity regulate strain activation under chemical and mechanical load? OMIECs are highly heterogeneous, where domains of different crystallinities and hydrophilicity respond entirely differently under swelling, dopant insertion, and mechanical load. Recent experimental and simulation results [22,58] showed local segregation of dopants and solvent in the OMIEC chain aggregates. Also, the spatially heterogeneous structure evolves over time under the external stimuli. We highlight in situ and operando techniques as well as coarse grained MD simulations to unveil the deformation behavior at the mesoscale. (iii) Toward the practical use, how to mitigate mechanical degradation of OMIEC-based devices? OMIECs are utilized in various electrochemical devices, and mechanical degradation associated with the breathing strain is one of the key failure mechanisms in their long cycles. Future research should identify the specific mechanism of degradation in each application, as discussed in Sec. 1.5, define and evaluate the mechanical stability of OMIEC-devices, determine the quantitative relation between mechanical degradation and performance metrics, and formulate engineering solutions to enhance the mechanical reliability of the electrochemical devices.

What is the constitutive law in OMIECs? Constitutive description is considered a holy grail in applied mechanics. As discussed in Sec. 4, OMIECs feature abundant entanglement through the complex chain configurations and are usually not crosslinked. Also, the microstructure of OMIECs differs by the synthesis conditions and further evolves with doping, hydration, and postprocessing. A systematic evaluation and modification of the classical constitutive models, calibrated against new experimental data, are likely needed to describe the mechanical behaviors of OMIECs.

How to decode multiphysics coupling in OMIECs? More specifically, (i) How does the electronic-ionic coupling dictate the kinetics? OMIECs are inherently more complex than conventional polyelectrolytes in multiphysics coupling. While the mobile electronic charges hop at a short time and disturb the local chemical and electrical environment, the chain conformational changes and mass transport occur at much larger time and length scales. For instance, in bio-electronic transistors and neuromorphic computing, high frequency ($\sim$100 kHz) of doping/dedoping and electronic switching may impede mass transport of slower response, which ultimately limits the capacity of OMIECs [194]. These unusual scenarios may induce unprecedented behaviors that are limited by multiple kinetic processes due to the high frequencies. Theoretical frameworks that evaluate the degree and mechanism of coupling are highly needed for a fundamental understanding of mixed conduction in OMIECs. (ii) How does the coupling differ in p-type and n-type OMIECs? Recently, n-doped PBDF stands out as an innovative n-type OMIEC [5,195], distinct from conventional p-type counterparts like PEDOT:PSS. Unlike traditional mixed conductors, which rely on hole transport and often incorporate hydrophilic additives (e.g., PSS) to enable ion mobility, n-PBDF achieves electron-dominated conduction through its fused benzodifurandione backbone. The ion transport in n-PBDF remains unclear. The distinct chemical structure of n-PBDF also gives rise to critical questions about its mechanical behavior. (iii) How do heterogeneity and dynamics interact with multiphysics coupling? As discussed throughout the review, OMIECs are highly heterogeneous systems considering the spatial variation in ionic/electronic conductivity, hydrophilicity, crystallinity, and crystallite distribution. One structural heterogeneity is separation of domains of high crystallinity/conductivity by amorphous/insulative neighborhoods. Much effort is needed in theoretical evaluation and experimental validation of such heterogeneity imposed on the multiphysics fields. For example, how do deformation and stress evolve with phase separation [196]? What are the boundary conditions between the phase domains? How do the field variables progress across the domain interfaces? (iv) How to incorporate multiphysics in device modeling? Electrochemical devices are complex systems involving large deformation, electrostatics, charge and mass transport, and other field variables that depend on the microstructure and composition. Integrating their coupling into the mathematical framework is nontrivial but essential to understanding the performance output of devices with high fidelity representation.

How to bridge fundamental understanding and design strategies of OMIECs? (i) How to navigate through the design parameter space for on-demand materials properties? As discussed in Sec. 5, materials design ranges from molecular chains, packing, to microstructure and compositing. And tradeoffs often need to be considered. For example, ductile polymers with both long backbone and side chains may induce high swelling and lower the conductivity. Therefore, figure of merit for targeted applications should be established, such as transconductance in OECTs [197], to guide the material design. To this end, a holistic understanding of the design parameters that may impact the structural response across multiple scales is required for on-desire bulk properties. (ii) How to engineer tough and highly conductive/insulative interfaces? OMIECs are integrated with inorganic materials for electrical conduction, organic materials for strengthening, and biomaterials for sensing. These interfaces must remain intact for functionality in diverse physiochemical and mechanical conditions. Strategic principles remain to be established in these areas to achieve tough, highly conductive, and compatible interfacing with the inactive components. (iii) What are the future novel applications? Standing alone, OMIECs of solution processibility, pattern-printed [198], three-dimensional printed [199], or self-assembled [200] are being developed in efficient actuator [201] or chiral optical [202] applications. This opens opportunities for structural designs, such as OMIEC metamaterials, to be explored for innovative applications.

Funding Data

- National Science Foundation (Grant Nos. CMMI-1941323 and CMMI-2210158; Funder ID: 10.13039/100000001).
- Office of Naval Research (Grant No. N00014-22-1-217; Funder ID: 10.13039/100000006).
- Multidisciplinary University Research Initiative (Grant No. N00014-21-1-2476; Funder ID: 10.13039/100014036).

References

[1] Zayat, B., Das, P., Thompson, B. C., and Narayan, S. R., 2021, "In Situ Measurement of Ionic and Electronic Conductivities of Conductive Polymers as a Function of Electrochemical Doping in Battery Electrolytes," J. Phys. Chem. C, **125**(14), pp. 7533–7541.

[2] Rawlings, D., Lee, D., Kim, J., Magdău, I.-B., Pace, G., Richardson, P. M., Thomas, E. M., et al., 2021, "Li+ and Oxidant Addition To Control Ionic and Electronic Conduction in Ionic Liquid-Functionalized Conjugated Polymers," Chem. Mater., **33**(16), pp. 6464–6474.

[3] Cho, B., Park, K. S., Baek, J., Oh, H. S., Koo Lee, Y.-E., and Sung, M. M., 2014, "Single-Crystal Poly(3,4-Ethylenedioxythiophene) Nanowires With Ultrahigh Conductivity," Nano Lett., **14**(6), pp. 3321–3327.

[4] Płocharski, J., Pukacki, W., and Roth, S., 1994, "Conductivity Study of Stretch-Oriented New Polyacetylene," J. Polym. Sci. Part B Polym. Phys., **32**(3), pp. 447–451.

[5] Tang, H., Liang, Y., Liu, C., Hu, Z., Deng, Y., Guo, H., Yu, Z., Song, A., Zhao, H., Zhao, D., Zhang, Y., Guo, X., Pei, J., Ma, Y., Cao, Y., and Huang, F., 2022, "A Solution-Processed n-Type Conducting Polymer With Ultrahigh Conductivity," Nature, **611**(7935), pp. 271–277.

[6] Park, S., Parida, K., and Lee, P. S., 2017, "Deformable and Transparent Ionic and Electronic Conductors for Soft Energy Devices," Adv. Energy Mater., **7**(22), p. 1701369.

[7] Kousseff, C. J., Halaksa, R., Parr, Z. S., and Nielsen, C. B., 2022, "Mixed Ionic and Electronic Conduction in Small-Molecule Semiconductors," Chem. Rev., **122**(4), pp. 4397–4419.

[8] Parr, Z. S., Rashid, R. B., Paulsen, B. D., Poggi, B., Tan, E., Freeley, M., Palma, M., Abrahams, I., Rivnay, J., and Nielsen, C. B., 2020, "Semiconducting Small Molecules as Active Materials for P-Type Accumulation Mode Organic Electrochemical Transistors," Adv. Electron. Mater., **6**(6), p. 2000215.

[9] Weng, B., Ashraf, S., Innis, P. C., and Wallace, G. G., 2013, "Colour Tunable Electrochromic Devices Based on PProDOT-(Hx)2 and PProDOT-(EtHx)2 Polymers," J. Mater. Chem. C, **1**(44), pp. 7430–7439.

[10] Paulsen, B. D., Fabiano, S., and Rivnay, J., 2021, "Mixed Ionic-Electronic Transport in Polymers," Annu. Rev. Mater. Res., **51**(1), pp. 73–99.

[11] Paulsen, B. D., Tybrandt, K., Stavrinidou, E., and Rivnay, J., 2020, "Organic Mixed Ionic–Electronic Conductors," Nat. Mater., **19**(1), pp. 13–26.

[12] Hinckley, A. C., Andrews, S. C., Dunham, M. T., Sood, A., Barako, M. T., Schneider, S., Toney, M. F., Goodson, K. E., and Bao, Z., 2021, "Achieving High Thermoelectric Performance and Metallic Transport in Solvent-Sheared PEDOT:PSS," Adv. Electron. Mater., **7**(3), p. 2001190.

[13] Wang, S., Zuo, G., Kim, J., and Sirringhaus, H., 2022, "Progress of Conjugated Polymers as Emerging Thermoelectric Materials," Prog. Polym. Sci., **129**, p. 101548.

[14] Gu, K., Onorato, J. W., Luscombe, C. K., and Loo, Y.-L., 2020, "The Role of Tie Chains on the Mechano-Electrical Properties of Semiconducting Polymer Films," Adv. Electron. Mater., **6**(4), p. 1901070.

[15] Bässler, H., and Köhler, A., 2012, "Charge Transport in Organic Semiconductors," Unimolecular and Supramolecular Electronics I: Chemistry and Physics Meet at Metal-Molecule Interfaces, R.M. Metzger, ed., Springer, Berlin, Heidelberg, pp. 1–65.

[16] Mollinger, S. A., Krajina, B. A., Noriega, R., Salleo, A., and Spakowitz, A. J., 2015, "Percolation, Tie-Molecules, and the Microstructural Determinants of Charge Transport in Semicrystalline Conjugated Polymers," ACS Macro Lett., **4**(7), pp. 708–712.

[17] Carré, A., 2007, "Polar Interactions at Liquid/Polymer Interfaces," J. Adhes. Sci. Technol., **21**(10), pp. 961–981.

[18] Rigo, E., Dong, Z., Park, J. H., Kennedy, E., Hokmabadi, M., Almonte-Garcia, L., Ding, L., Aluru, N., and Timp, G., 2019, "Measurements of the Size and Correlations Between Ions Using an Electrolytic Point Contact," Nat. Commun., **10**(1), p. 2382.

[19] Ratner, M. A., and Shriver, D. F., 1988, "Ion Transport in Solvent-Free Polymers," Chem. Rev., **88**(1), pp. 109–124.

[20] Yang, H., and Wu, N., 2022, "Ionic Conductivity and Ion Transport Mechanisms of Solid-State Lithium-Ion Battery Electrolytes: A Review," Energy Sci. Eng., **10**(5), pp. 1643–1671.

[21] Choi, P., Jalani, N. H., and Datta, R., 2005, "Thermodynamics and Proton Transport in Nafion: II. Proton Diffusion Mechanisms and Conductivity," J. Electrochem. Soc., **152**(3), p. E123.

[22] Yang, X., Sun, H., He, X., and Zhao, K., 2025, "Molecular Mechanism of Mechanical Breathing in Organic Mixed Ionic-Electronic Conductors," Macromolecules, **58**(1), pp. 45–60.

[23] Zhong, D., Xiang, Y., Wang, Z., Chen, Z., Liu, J., Wu, Z. L., Xiao, R., Qu, S., and Yang, W., 2023, "A Visco-Hyperelastic Model for Hydrogels With Tunable Water Content," J. Mech. Phys. Solids, **173**, p. 105206.

[24] Wang, X., and Zhao, K., 2023, "A Continuum Theory of Organic Mixed Ionic-Electronic Conductors of Phase Separation," J. Mech. Phys. Solids, **172**, p. 105178.

[25] Kusoglu, A., and Weber, A. Z., 2017, "New Insights Into Perfluorinated Sulfonic-Acid Ionomers," Chem. Rev., **117**(3), pp. 987–1104.

[26] Zhou, Y., and Jin, L., 2023, "Mechanics Underpinning Phase Separation of Hydrogels," Macromolecules, **56**(2), pp. 426–439.

[27] Ding, Z., Zhao, K., and Han, Y., 2025, "Strain-Induced Morphology Evolution and Charge Transport in Conjugated Polymer Films," Interdiscip. Mater., **4**(1), pp. 138–161.

[28] Lu, Y., Wang, J.-Y., and Pei, J., 2021, "Achieving Efficient N-Doping of Conjugated Polymers by Molecular Dopants," Acc. Chem. Res., **54**(13), pp. 2871–2883.

[29] Wang, X., Li, X., Mei, J., and Zhao, K., 2022, "Doping Kinetics in Organic Mixed Ionic–Electronic Conductors: Moving Front Experiments and the Stress Effect," Ext. Mech. Lett., **54**, p. 101739.

[30] Chen, K., Hu, H., Song, I., Gobeze, H. B., Lee, W.-J., Abtahi, A., Schanze, K. S., and Mei, J., 2023, "Organic Optoelectronic Synapse Based on Photon-Modulated Electrochemical Doping," Nat. Photonics, **17**(7), pp. 629–637.

[31] Bischak, C. G., Flagg, L. Q., Yan, K., Rehman, T., Davies, D. W., Quezada, R. J., Onorato, J. W., Luscombe, C. K., Diao, Y., Li, C.-Z., and Ginger, D. S., 2020, "A Reversible Structural Phase Transition by Electrochemically-Driven Ion Injection Into a Conjugated Polymer," J. Am. Chem. Soc., **142**(16), pp. 7434–7442.

[32] Kaiser, A. B., 2001, "Systematic Conductivity Behavior in Conducting Polymers: Effects of Heterogeneous Disorder," Adv. Mater., **13**(12–13), pp. 927–941.

[33] Jackson, S. R., Kingsford, R. L., Collins, G. W., and Bischak, C. G., 2023, "Crystallinity Determines Ion Injection Kinetics and Local Ion Density in Organic Mixed Conductors," Chem. Mater., **35**(14), pp. 5392–5400.

[34] Xie, R., Colby, R. H., and Gomez, E. D., 2018, "Connecting the Mechanical and Conductive Properties of Conjugated Polymers," Adv. Electron. Mater., **4**(10), p. 1700356.

[35] Sujanani, R., Nguyen, P. H., Gordon, L. W., Bamford, J. T., Zele, A., Pedretti, B. J., Lynd, N. A., Clément, R. J., and Segalman, R. A., 2025, "Influence of Water Sorption on Ionic Conductivity in Polyether Electrolytes at Low Hydration," ACS Macro Lett., **14**(1), pp. 64–71.

[36] Quill, T. J., LeCroy, G., Marks, A., Hesse, S. A., Thiburce, Q., McCulloch, I., Tassone, C. J., Takacs, C. J., Giovannitti, A., and Salleo, A., 2024, "Charge Carrier Induced Structural Ordering And Disordering in Organic Mixed Ionic Electronic Conductors," Adv. Mater., **36**(15), p. 2310157.

[37] Sun, H., Li, S., Shen, Y., Miao, F., Zhang, P., and Shao, G., 2020, "Integrated Structural Design of Polyaniline-Modified Nitrogen-Doped Hierarchical Porous Carbon Nanofibers as Binder-Free Electrodes Toward All-Solid-State Flexible Supercapacitors," Appl. Surf. Sci., **501**, p. 144001.

[38] Shoa, T., Madden, J. D., Munce, N. R., and Yang, V., 2010, "Analytical Modeling of a Conducting Polymer-Driven Catheter," Polym. Int., **59**(3), pp. 343–351.

[39] Correia, D. M., Barbosa, J. C., Costa, C. M., Reis, P. M., Esperança, J. M. S. S., de Zea Bermudez, V., and Lanceros-Méndez, S., 2019, "Ionic Liquid Cation Size-Dependent Electromechanical Response of Ionic Liquid/Poly (Vinylidene Fluoride)-Based Soft Actuators," J. Phys. Chem. C, **123**(20), pp. 12744–12752.

[40] Melling, D., Martinez, J. G., and Jager, E. W. H., 2019, "Conjugated Polymer Actuators and Devices: Progress and Opportunities," Adv. Mater., **31**(22), p. 1808210.

[41] Shi, P., Amb, C. M., Knott, E. P., Thompson, E. J., Liu, D. Y., Mei, J., Dyer, A. L., and Reynolds, J. R., 2010, "Broadly Absorbing Black to Transmissive Switching Electrochromic Polymers," Adv. Mater., **22**(44), pp. 4949–4953.

[42] Li, X., Perera, K., He, J., Gumyusenge, A., and Mei, J., 2019, "Solution-Processable Electrochromic Materials and Devices: Roadblocks and Strategies Towards Large-Scale Applications," J. Mater. Chem. C, **7**(41), pp. 12761–12789.

[43] Tang, S., Sandström, A., Lundberg, P., Lanz, T., Larsen, C., van Reenen, S., Kemerink, M., and Edman, L., 2017, "Design Rules for Light-Emitting Electrochemical Cells Delivering Bright Luminance at 27.5 Percent External Quantum Efficiency," Nat. Commun., **8**(1), p. 1190.

[44] Sandström, A., Dam, H. F., Krebs, F. C., and Edman, L., 2012, "Ambient Fabrication of Flexible and Large-Area Organic Light-Emitting Devices Using Slot-Die Coating," Nat. Commun., **3**(1), p. 1002.

[45] Ferhat, S., Domain, C., Vidal, J., Noël, D., Ratier, B., and Lucas, B., 2018, "Organic Thermoelectric Devices Based on a Stable N-Type Nanocomposite Printed on Paper," Sustain. Energy Fuels, **2**(1), pp. 199–208.

[46] Song, I., Lee, W.-J., Ke, Z., You, L., Chen, K., Naskar, S., Mehra, P., and Mei, J., 2024, "An N-Doped Capacitive Transparent Conductor for All-Polymer Electrochromic Displays," Nat. Electron., **7**(12), pp. 1158–1169.

[47] Dai, Y., Dai, S., Li, N., Li, Y., Moser, M., Strzalka, J., Prominski, A., et al., 2022, "Stretchable Redox-Active Semiconducting Polymers for High-Performance Organic Electrochemical Transistors," Adv. Mater., **34**(23), p. 2201178.

[48] Rivnay, J., Inal, S., Salleo, A., Owens, R. M., Berggren, M., and Malliaras, G. G., 2018, "Organic Electrochemical Transistors," Nat. Rev. Mater., **3**(2), pp. 1–14.

[49] Mabeck, J. T., and Malliaras, G. G., 2005, "Chemical and Biological Sensors Based on Organic Thin-Film Transistors," Anal. Bioanal. Chem., **384**(2), pp. 343–353.

[50] Lin, P., and Yan, F., 2012, "Organic Thin-Film Transistors for Chemical and Biological Sensing," Adv. Mater., **24**(1), pp. 34–51.

[51] Hu, C., Wang, L., Liu, S., Sheng, X., and Yin, L., 2024, "Recent Development of Implantable Chemical Sensors Utilizing Flexible and Biodegradable Materials for Biomedical Applications," ACS Nano, **18**(5), pp. 3969–3995.

[52] Kim, J., Pankow, R. M., Cho, Y., Duplessis, I. D., Qin, F., Meli, D., Daso, R., Zheng, D., Huang, W., Rivnay, J., Marks, T. J., and Facchetti, A., 2024, "Monolithically Integrated High-Density Vertical Organic Electrochemical Transistor Arrays and Complementary Circuits," Nat. Electron., **7**(3), pp. 234–243.

[53] Gumyusenge, A., Melianas, A., Keene, S. T., and Salleo, A., 2021, "Materials Strategies for Organic Neuromorphic Devices," Annu. Rev. Mater. Res., **51**(1), pp. 47–71.

[54] Liang, Y., Che, C., Tang, H., Zhang, K., Lan, L., Zhou, C., Ma, Y., and Huang, F., 2023, "Influence of Interaction Between Electrolyte With Side-Chain Free

Conjugated Polymer on the Performance of Organic Electrochemical Transistors," ACS Appl. Mater. Interfaces, **16**(16), pp. 19977–19986.
[55] Wang, X., Chen, K., de Vasconcelos, L. S., He, J., Shin, Y. C., Mei, J., and Zhao, K., 2020, "Mechanical Breathing in Organic Electrochromics," Nat. Commun., **11**(1), p. 211.
[56] Das, P., Zayat, B., Wei, Q., Salamat, C. Z., Magdău, I.-B., Elizalde-Segovia, R., Rawlings, D., et al., 2020, "Dihexyl-Substituted Poly(3,4-Propylenedioxythiophene) as a Dual Ionic and Electronic Conductive Cathode Binder for Lithium-Ion Batteries," Chem. Mater., **32**(21), pp. 9176–9189.
[57] Szumska, A. A., Maria, I. P., Flagg, L. Q., Savva, A., Surgailis, J., Paulsen, B. D., Moia, D., et al., 2021, "Reversible Electrochemical Charging of N-Type Conjugated Polymer Electrodes in Aqueous Electrolytes," J. Am. Chem. Soc., **143**(36), pp. 14795–14805.
[58] Tsarfati, Y., Bustillo, K. C., Savitzky, B. H., Balhorn, L., Quill, T. J., Marks, A., Donohue, J., et al., 2025, "The Hierarchical Structure of Organic Mixed Ionic–Electronic Conductors and Its Evolution in Water," Nat. Mater., **24**(1), pp. 101–108.
[59] Tyagi, M., Fathollahzadeh, M., Martinez, J. G., Mak, W. C., Filippini, D., and Jager, E. W. H., 2023, "Radially Actuating Conducting Polymer Microactuators as Gates for Dynamic Microparticle Sieve Based on Printed Microfluidics," Sens. Actuators B Chem., **382**, p. 133448.
[60] Dimov, I. B., Moser, M., Malliaras, G. G., and McCulloch, I., 2022, "Semiconducting Polymers for Neural Applications," Chem. Rev., **122**(4), pp. 4356–4396.
[61] Kang, J., Mun, J., Zheng, Y., Koizumi, M., Matsuhisa, N., Wu, H.-C., Chen, S., Tok, J. B.-H., Lee, G. H., Jin, L., and Bao, Z., 2022, "Tough-Interface-Enabled Stretchable Electronics Using Non-Stretchable Polymer Semiconductors and Conductors," Nat. Nanotechnol., **17**(12), pp. 1265–1271.
[62] Su, X., Wu, X., Chen, S., Nedumaran, A. M., Stephen, M., Hou, K., Czarny, B., and Leong, W. L., 2022, "A Highly Conducting Polymer for Self-Healable, Printable, and Stretchable Organic Electrochemical Transistor Arrays and Near Hysteresis-Free Soft Tactile Sensors," Adv. Mater., **34**(19), p. 2200682.
[63] Wang, X., de Vasconcelos, L. S., Chen, K., Perera, K., Mei, J., and Zhao, K., 2020, "In Situ Measurement of Breathing Strain and Mechanical Degradation in Organic Electrochromic Polymers," ACS Appl. Mater. Interfaces, **12**(45), pp. 50889–50895.
[64] Root, S. E., Savagatrup, S., Printz, A. D., Rodriquez, D., and Lipomi, D. J., 2017, "Mechanical Properties of Organic Semiconductors for Stretchable, Highly Flexible, and Mechanically Robust Electronics," Chem. Rev., **117**(9), pp. 6467–6499.
[65] Paleti, S. H. K., Kim, Y., Kimpel, J., Craighero, M., Haraguchi, S., and Müller, C., 2024, "Impact of Doping on the Mechanical Properties of Conjugated Polymers," Chem. Soc. Rev., **53**(4), pp. 1702–1729.
[66] Xiang, Y., Zhong, D., Rudykh, S., Zhou, H., Qu, S., and Yang, W., 2020, "A Review of Physically Based and Thermodynamically Based Constitutive Models for Soft Materials," ASME J. Appl. Mech., **87**(11), p. 110801.
[67] Boyce, M. C., and Arruda, E. M., 2000, "Constitutive Models of Rubber Elasticity: A Review," Rubber Chem. Technol., **73**(3), pp. 504–523.
[68] Zhang, B., Xiang, L., Yan, C., Jiang, Z., Zhao, H., Li, C., and Zhang, F., 2024, "Morphology-Controlled Ion Transport in Mixed-Orientation Polymers," ACS Appl. Mater. Interfaces, **16**(25), pp. 32456–32465.
[69] Odin, C., and Nechtschein, M., 1991, "Slow Relaxation in Conducting Polymers," Phys. Rev. Lett., **67**(9), pp. 1114–1117.
[70] Bakulin, A. A., Martyanov, D. S., Paraschuk, D. Y., Pshenichnikov, M. S., and van Loosdrecht, P. H. M., 2008, "Ultrafast Charge Photogeneration Dynamics in Ground-State Charge-Transfer Complexes Based on Conjugated Polymers," J. Phys. Chem. B, **112**(44), pp. 13730–13737.
[71] Aziz, I. A., Gladisch, J., Musumeci, C., Moser, M., Griggs, S., Kousseff, C. J., Berggren, M., McCulloch, I., and Stavrinidou, E., 2024, "Electrochemical Modulation of Mechanical Properties of Glycolated Polythiophenes," Mater. Horiz., **11**(8), pp. 2021–2031.
[72] Gladisch, J., Stavrinidou, E., Ghosh, S., Giovannitti, A., Moser, M., Zozoulenko, I., McCulloch, I., and Berggren, M., 2020, "Reversible Electronic Solid–Gel Switching of a Conjugated Polymer," Adv. Sci., **7**(2), p. 1901144.
[73] Abrantes, L. M., Correia, J. P., Savic, M., and Jin, G., 2001, "Structural Modifications During Conducting Polymer Formation — An Ellipsometric Study," Electrochim. Acta, **46**(20–21), pp. 3181–3187.
[74] Richter, S., Rebarz, M., Herrfurth, O., Espinoza, S., Schmidt-Grund, R., and Andreasson, J., 2021, "Broadband Femtosecond Spectroscopic Ellipsometry," Rev. Sci. Instrum.,, **92**(3), p. 033104.
[75] Della Santa, A., De Rossi, D., and Mazzoldi, A., 1997, "Performance and Work Capacity of a Polypyrrole Conducting Polymer Linear Actuator," Synth. Met., **90**(2), pp. 93–100.
[76] Wang, Y., Chen, K.-L., Awada, A., Prine, N., Cao, Z., Zhu, C., Chiu, Y.-C., Rondeau-Gagné, S., and Gu, X., 2023, "Leveraging Non-Covalent Interactions to Control the Morphology and Electrical and Mechanical Properties of Stretchable Semiconducting Composites," Chem. Mater., **35**(22), pp. 9713–9724.
[77] Zhang, S., Ocheje, M. U., Luo, S., Ehlenberg, D., Appleby, B., Weller, D., Zhou, D., Rondeau-Gagné, S., and Gu, X., 2018, "Probing the Viscoelastic Property of Pseudo Free-Standing Conjugated Polymeric Thin Films," Macromol. Rapid Commun., **39**(14), p. 1800092.
[78] Schumacher, R., Borges, G., and Kanazawa, K. K., 1985, "The Quartz Microbalance: A Sensitive Tool to Probe Surface Reconstructions on Gold Electrodes in Liquid," Surf. Sci. Lett., **163**(1), pp. L621–L626.
[79] Easley, A. D., Ma, T., Eneh, C. I., Yun, J., Thakur, R. M., and Lutkenhaus, J. L., 2022, "A Practical Guide to Quartz Crystal Microbalance With Dissipation Monitoring of Thin Polymer Films," J. Polym. Sci., **60**(7), pp. 1090–1107.
[80] Wang, S., Li, F., Easley, A. D., and Lutkenhaus, J. L., 2019, "Real-Time Insight Into the Doping Mechanism of Redox-Active Organic Radical Polymers," Nat. Mater., **18**(1), pp. 69–75.
[81] Ohayon, D., Druet, V., and Inal, S., 2023, "A Guide for the Characterization of Organic Electrochemical Transistors and Channel Materials," Chem. Soc. Rev., **52**(3), pp. 1001–1023.
[82] Umeda, K., McArthur, S. J., and Kodera, N., 2023, "Spatiotemporal Resolution in High-Speed Atomic Force Microscopy for Studying Biological Macromolecules in Action," Microscopy, **72**(2), pp. 151–161.
[83] Giridharagopal, R., Flagg, L. Q., Harrison, J. S., Ziffer, M. E., Onorato, J., Luscombe, C. K., and Ginger, D. S., 2017, "Electrochemical Strain Microscopy Probes Morphology-Induced Variations in Ion Uptake and Performance in Organic Electrochemical Transistors," Nat. Mater., **16**(7), pp. 737–742.
[84] Balke, N., Jesse, S., Kim, Y., Adamczyk, L., Tselev, A., Ivanov, IN., Dudney, N. J., and Kalinin, S. V., 2010, "Real Space Mapping of Li-Ion Transport in Amorphous Si Anodes With Nanometer Resolution," Nano Lett., **10**(9), pp. 3420–3425.
[85] Paulsen, B. D., Wu, R., Takacs, C. J., Steinrück, H.-G., Strzalka, J., Zhang, Q., Toney, M. F., and Rivnay, J., 2020, "Time-Resolved Structural Kinetics of an Organic Mixed Ionic–Electronic Conductor," Adv. Mater., **32**(40), p. 2003404.
[86] Isnard, O., 2007, "A Review of In Situ and/or Time Resolved Neutron Scattering," C. R. Phys., **8**(7–8), pp. 789–805.
[87] Kim, T., Oh, S., Choudhry, U., Meinhart, C. D., Chabinyc, M. L., and Liao, B., 2021, "Transient Strain-Induced Electronic Structure Modulation in a Semiconducting Polymer Imaged by Scanning Ultrafast Electron Microscopy," Nano Lett., **21**(21), pp. 9146–9152.
[88] Panova, O., Ophus, C., Takacs, C. J., Bustillo, K. C., Balhorn, L., Salleo, A., Balsara, N., and Minor, A. M., 2019, "Diffraction Imaging of Nanocrystalline Structures in Organic Semiconductor Molecular Thin Films," Nat. Mater., **18**(8), pp. 860–865.
[89] Kuei, B., Bator, C., and Gomez, E. D., 2020, "Imaging 0.36 Nm Lattice Planes in Conjugated Polymers by Minimizing Beam Damage," Macromolecules, **53**(19), pp. 8296–8302.
[90] Lolla, D., Gorse, J., Kisielowski, C., Miao, J., Taylor, P. L., Chase, G. G., and Reneker, D. H., 2016, "Polyvinylidene Fluoride Molecules in Nanofibers, Imaged at Atomic Scale by Aberration Corrected Electron Microscopy," Nanoscale, **8**(1), pp. 120–128.
[91] Kuei, B., Aplan, M. P., Litofsky, J. H., and Gomez, E. D., 2020, "New Opportunities in Transmission Electron Microscopy of Polymers," Mater. Sci. Eng. R Rep., **139**, p. 100516.
[92] McCulloch, B., Ho, V., Hoarfrost, M., Stanley, C., Do, C., Heller, W. T., and Segalman, R. A., 2013, "Polymer Chain Shape of Poly(3-Alkylthiophenes) in Solution Using Small-Angle Neutron Scattering," Macromolecules, **46**(5), pp. 1899–1907.
[93] Cao, Z., Li, Z., Zhang, S., Galuska, L., Li, T., Do, C., Xia, W., Hong, K., and Gu, X., 2020, "Decoupling Poly(3-Alkylthiophenes)' Backbone and Side-Chain Conformation by Selective Deuteration and Neutron Scattering," Macromolecules, **53**(24), pp. 11142–11152.
[94] Kwok, J. J., Park, K. S., Patel, B. B., Dilmurat, R., Beljonne, D., Zuo, X., Lee, B., and Diao, Y., 2022, "Understanding Solution State Conformation and Aggregate Structure of Conjugated Polymers Via Small Angle X-Ray Scattering," Macromolecules, **55**(11), pp. 4353–4366.
[95] Kuei, B. D., and Gomez, E., 2017, "Chain Conformations and Phase Behavior of Conjugated Polymers," Soft Matter, **13**(1), pp. 49–67.
[96] Balhorn, L., MacPherson, Q., Bustillo, K. C., Takacs, C. J., Spakowitz, A. J., and Salleo, A., 2022, "Closing the Loop Between Microstructure and Charge Transport in Conjugated Polymers by Combining Microscopy and Simulation," Proc. Natl. Acad. Sci., **119**(46), p. e2204346119.
[97] Luo, S., Li, N., Zhang, S., Zhang, C., Qu, T., Ocheje, M. U., Xue, G., Gu, X., Rondeau-Gagné, S., Hu, W., Wang, S., Teng, C., Zhou, D., and Xu, J., 2021, "Observation of Stepwise Ultrafast Crystallization Kinetics of Donor–Acceptor Conjugated Polymers and Correlation With Field Effect Mobility," Chem. Mater., **33**(5), pp. 1637–1647.
[98] Flory, P. J., 1950, "Statistical Mechanics of Swelling of Network Structures," J. Chem. Phys,., **18**(1), pp. 108–111.
[99] Chen, S. E., Flagg, L. Q., Onorato, J. W., Richter, L. J., Guo, J., Luscombe, C. K., and Ginger, D. S., 2022, "Impact of Varying Side Chain Structure on Organic Electrochemical Transistor Performance: A Series of Oligoethylene Glycol-Substituted Polythiophenes," J. Mater. Chem. A, **10**(19), pp. 10738–10749.
[100] Moser, M., Wang, Y., Cecilia Hidalgo, T., Liao, H., Yu, Y., Chen, J., Duan, J., et al., 2022, "Propylene and Butylene Glycol: New Alternatives to Ethylene Glycol in Conjugated Polymers for Bioelectronic Applications," Mater. Horiz., **9**(3), pp. 973–980.
[101] Surgailis, J., Savva, A., Druet, V., Paulsen, B. D., Wu, R., Hamidi-Sakr, A., Ohayon, D., Nikiforidis, G., Chen, X., McCulloch, I., Rivnay, J., and Inal, S., 2021, "Mixed Conduction in an N-Type Organic Semiconductor in the Absence of Hydrophilic Side-Chains," Adv. Funct. Mater., **31**(21), p. 2010165.
[102] Guo, J., Flagg, L. Q., Tran, D. K., Chen, S. E., Li, R., Kolhe, N. B., Giridharagopal, R., Jenekhe, S. A., Richter, L. J., and Ginger, D. S., 2023, "Hydration of a Side-Chain-Free n-Type Semiconducting Ladder Polymer Driven by Electrochemical Doping," J. Am. Chem. Soc., **145**(3), pp. 1866–1876.

[103] Surgailis, J., Flagg, L. Q., Richter, L. J., Druet, V., Griggs, S., Wu, X., Moro, S., et al., 2024, "The Role of Side Chains and Hydration on Mixed Charge Transport in N-Type Polymer Films," Adv. Mater., **36**(51), p. 2313121.
[104] Jeong, D., Jo, I.-Y., Lee, S., Kim, J. H., Kim, Y., Kim, D., Reynolds, J. R., Yoon, M.-H., and Kim, B. J., 2022, "High-Performance n-Type Organic Electrochemical Transistors Enabled by Aqueous Solution Processing of Amphiphilicity-Driven Polymer Assembly," Adv. Funct. Mater., **32**(16), p. 2111950.
[105] Nicolini, T., Surgailis, J., Savva, A., Scaccabarozzi, A. D., Nakar, R., Thuau, D., Wantz, G., Richter, L. J., Dautel, O., Hadziioannou, G., and Stingelin, N., 2021, "A Low-Swelling Polymeric Mixed Conductor Operating in Aqueous Electrolytes," Adv. Mater., **33**(2), p. 2005723.
[106] Advincula, A. A., Jones, A. L., Thorley, K. J., Österholm, A. M., Ponder, J. F. Jr., and Reynolds, J. R., 2022, "Probing Comonomer Selection Effects on Dioxythiophene-Based Aqueous-Compatible Polymers for Redox Applications," Chem. Mater., **34**(10), pp. 4633–4645.
[107] Sun, Z., Khau, B., Dong, H., Takacs, C. J., Yuan, S., Sun, M., Mosevitzky Lis, B., Nguyen, D., and Reichmanis, E., 2023, "Carboxyl-Alkyl Functionalized Conjugated Polyelectrolytes for High Performance Organic Electrochemical Transistors," Chem. Mater., **35**(21), pp. 9299–9312.
[108] Moser, M., Gladisch, J., Ghosh, S., Hidalgo, T. C., Ponder, J. F., Jr., Sheelamanthula, R., Thiburce, Q., et al., 2021, "Controlling Electrochemically Induced Volume Changes in Conjugated Polymers by Chemical Design: From Theory to Devices," Adv. Funct. Mater, **31**(26), p. 2100723.
[109] Lan, L., Chen, J., Wang, Y., Li, P., Yu, Y., Zhu, G., Li, Z., Lei, T., Yue, W., and McCulloch, I., 2022, "Facilely Accessible Porous Conjugated Polymers Toward High-Performance and Flexible Organic Electrochemical Transistors," Chem. Mater., **34**(4), pp. 1666–1676.
[110] Schmode, P., Savva, A., Kahl, R., Ohayon, D., Meichsner, F., Dolynchuk, O., Thurn-Albrecht, T., Inal, S., and Thelakkat, M., 2020, "The Key Role of Side Chain Linkage in Structure Formation and Mixed Conduction of Ethylene Glycol Substituted Polythiophenes," ACS Appl. Mater. Interfaces, **12**(11), pp. 13029–13039.
[111] Hallani, R. K., Paulsen, B. D., Petty, A. J. I., Sheelamanthula, R., Moser, M., Thorley, K. J., Sohn, W., et al., 2021, "Regiochemistry-Driven Organic Electrochemical Transistor Performance Enhancement in Ethylene Glycol-Functionalized Polythiophenes," J. Am. Chem. Soc., **143**(29), pp. 11007–11018.
[112] Moser, M., Hidalgo, T. C., Surgailis, J., Gladisch, J., Ghosh, S., Sheelamanthula, R., Thiburce, Q., et al., 2020, "Side Chain Redistribution as a Strategy to Boost Organic Electrochemical Transistor Performance and Stability," Adv. Mater., **32**(37), p. 2002748.
[113] Perera, K., Wu, W., You, L., Elman, J. F., Wang, Z., Wang, X., Ahmed, M., Ke, Z., and Mei, J., 2023, "Absorption Coefficient and Optical Contrast Modulation Through Side Chain Engineering of Electrochromic Polymers," Macromolecules, **56**(2), pp. 480–489.
[114] Ding, B., Jo, I.-Y., Yu, H., Kim, J. H., Marsh, A. V., Gutiérrez-Fernández, E., et al., 2023, "Enhanced Organic Electrochemical Transistor Performance of Donor–Acceptor Conjugated Polymers Modified With Hybrid Glycol/Ionic Side Chains by Postpolymerization Modification," Chem. Mater., **35**(8), pp. 3290–3299.
[115] Siemons, N., Pearce, D., Cendra, C., Yu, H., Tuladhar, S. M., Hallani, R. K., Sheelamanthula, R., et al., 2022, "Impact of Side-Chain Hydrophilicity on Packing, Swelling, and Ion Interactions in Oxy-Bithiophene Semiconductors," Adv. Mater., **34**(39), p. 2204258.
[116] Wang, K., Huang, L., Eedugurala, N., Zhang, S., Sabuj, M. A., Rai, N., Gu, X., Azoulay, J. D., and Ng, T. N., 2019, "Wide Potential Window Supercapacitors Using Open-Shell Donor–Acceptor Conjugated Polymers With Stable N-Doped States," Adv. Energy Mater., **9**(47), p. 1902806.
[117] Perera, K., Yi, Z., You, L., Ke, Z., and Mei, J., 2020, "Conjugated Electrochromic Polymers With Amide-Containing Side Chains Enabling Aqueous Electrolyte Compatibility," Polym. Chem., **11**(2), pp. 508–516.
[118] Liu, K., Perera, K., Wang, Z., Mei, J., and Boudouris, B. W., 2021, "Impact of Open-Shell Loading on Mass Transport and Doping in Conjugated Radical Polymers," J. Polym. Sci., **59**(22), pp. 2771–2782.
[119] Zhao, X., Alsufyani, M., Tian, J., Lin, Y., Jeong, S. Y., Woo, H. Y., Yin, Y., and McCulloch, I., 2024, "High Efficiency N-Type Doping of Organic Semiconductors by Cation Exchange," Adv. Mater., **36**(47), p. 2412811.
[120] Flagg, L. Q., Bischak, C. G., Quezada, R. J., Onorato, J. W., Luscombe, C. K., and Ginger, D. S., 2020, "P-Type Electrochemical Doping Can Occur by Cation Expulsion in a High-Performing Polymer for Organic Electrochemical Transistors," ACS Mater. Lett., **2**(3), pp. 254–260.
[121] Guo, J., Chen, S. E., Giridharagopal, R., Bischak, C. G., Onorato, J. W., Yan, K., Shen, Z., Li, C.-Z., Luscombe, C. K., and Ginger, D. S., 2024, "Understanding Asymmetric Switching Times in Accumulation Mode Organic Electrochemical Transistors," Nat. Mater., **23**(5), pp. 656–663.
[122] Keene, S. T., Laulainen, J. E. M., Pandya, R., Moser, M., Schnedermann, C., Midgley, P. A., McCulloch, I., Rao, A., and Malliaras, G. G., 2023, "Hole-Limited Electrochemical Doping in Conjugated Polymers," Nat. Mater., **22**(9), pp. 1121–1127.
[123] Keene, S. T., Rao, A. G., and Malliaras, G., 2023, "The Relationship Between Ionic-Electronic Coupling and Transport in Organic Mixed Conductors," Sci. Adv., **9**(35), p. eadi3536.
[124] Rolston, N., Watson, B. L., Bailie, C. D., McGehee, M. D., Bastos, J. P., Gehlhaar, R., Kim, J.-E., Vak, D., Mallajosyula, A. T., Gupta, G., Mohite, A. D., and Dauskardt, R. H., 2016, "Mechanical Integrity of Solution-Processed Perovskite Solar Cells," Extreme Mech. Lett., **9**, pp. 353–358.
[125] Balar, N., and O'Connor, B. T., 2017, "Correlating Crack Onset Strain and Cohesive Fracture Energy in Polymer Semiconductor Films," Macromolecules, **50**(21), pp. 8611–8618.
[126] Chen, A. X., Kleinschmidt, A. T., Choudhary, K., and Lipomi, D. J., 2020, "Beyond Stretchability: Strength, Toughness, and Elastic Range in Semiconducting Polymers," Chem. Mater., **32**(18), pp. 7582–7601.
[127] Seitz, J. T., 1993, "The Estimation of Mechanical Properties of Polymers From Molecular Structure," J. Appl. Polym. Sci., **49**(8), pp. 1331–1351.
[128] Savagatrup, S., Makaram, A. S., Burke, D. J., and Lipomi, D. J., 2014, "Mechanical Properties of Conjugated Polymers and Polymer-Fullerene Composites as a Function of Molecular Structure," Adv. Funct. Mater., **24**(8), pp. 1169–1181.
[129] Chung, S., Kim, S. H., Ok, E., Kim, B. J., Kang, B., and Cho, K., 2024, "Structural Insights Into Conjugated Polymers for Stretchable Organic Transistors," Chem. Mater., **36**(1), pp. 74–98.
[130] Galuska, L. A., Muckley, E. S., Cao, Z., Ehlenberg, D. F., Qian, Z., Zhang, S., Rondeau-Gagné, S., Phan, M. D., Ankner, J. F., Ivanov, IN., and Gu, X., 2021, "SMART Transfer Method to Directly Compare the Mechanical Response of Water-Supported and Free-Standing Ultrathin Polymeric Films," Nat. Commun., **12**(1), p. 2347.
[131] Zhuo, Z., Ni, M., Yu, N., Zheng, Y., Lin, Y., Yang, J., Sun, L., Wang, L., Bai, L., Chen, W., Xu, M., Huo, F., Lin, J., Feng, Q., and Huang, W., 2024, "Intrinsically Stretchable Fully π-Conjugated Polymer Film Via Fluid Conjugated Molecular External-Plasticizing for Flexible Light-Emitting Diodes," Nat. Commun., **15**(1), p. 7990.
[132] Song, R., Schrickx, H., Balar, N., Siddika, S., Sheikh, N., and O'Connor, B. T., 2020, "Unveiling the Stress–Strain Behavior of Conjugated Polymer Thin Films for Stretchable Device Applications," Macromolecules, **53**(6), pp. 1988–1997.
[133] Kim, J.-H., Nizami, A., Hwangbo, Y., Jang, B., Lee, H.-J., Woo, C.-S., Hyun, S., and Kim, T.-S., 2013, "Tensile Testing of Ultra-Thin Films on Water Surface," Nat. Commun., **4**(1), p. 2520.
[134] Choi, J., Kim, W., Kim, D., Kim, S., Chae, J., Choi, S. Q., Kim, F. S., Kim, T.-S., and Kim, B. J., 2019, "Importance of Critical Molecular Weight of Semicrystalline N-Type Polymers for Mechanically Robust, Efficient Electroactive Thin Films," Chem. Mater., **31**(9), pp. 3163–3173.
[135] Printz, A. D., Zaretski, A. V., Savagatrup, S., Chiang, A. S.-C., and Lipomi, D. J., 2015, "Yield Point of Semiconducting Polymer Films on Stretchable Substrates Determined by Onset of Buckling," ACS Appl. Mater. Interfaces, **7**(41), pp. 23257–23264.
[136] Son, S. Y., Lee, G., Wang, H., Samson, S., Wei, Q., Zhu, Y., and You, W., 2022, "Integrating Charge Mobility, Stability and Stretchability Within Conjugated Polymer Films for Stretchable Multifunctional Sensors," Nat. Commun., **13**(1), p. 2739.
[137] Zhao, D., Kim, D., Ghosh, S., Wang, G., Huang, W., Zhu, Z., Marks, T. J., Zozoulenko, I., and Facchetti, A., 2024, "Mechanical, Morphological, and Charge Transport Properties of NDI Polymers With Variable Built-in Π-Conjugation Lengths Probed by Simulation and Experiment," Adv. Funct. Mater., **34**(4), p. 2310071.
[138] Wang, G.-J. N., Gasperini, A., and Bao, Z., 2018, "Stretchable Polymer Semiconductors for Plastic Electronics," Adv. Electron. Mater., **4**(2), p. 1700429.
[139] Martín, J., Muñoz, M., Encinar, M., Calleja, M., and Martín-González, M., 2014, "Fabrication and Mechanical Characterization of Semi-Free-Standing (Conjugated) Polymer Thin Films," Langmuir, **30**(18), pp. 5217–5223.
[140] Young, T. J., Monclus, M. A., Burnett, T. L., Broughton, W. R., Ogin, S. L., and Smith, P. A., 2011, "The Use of the PeakForceTM Quantitative Nanomechanical Mapping AFM-Based Method for High-Resolution Young's Modulus Measurement of Polymers," Meas. Sci. Technol., **22**(12), p. 125703.
[141] Panchal, V., Dobryden, I., Hangen, U. D., Simatos, D., Spalek, L. J., Jacobs, I. E., Schweicher, G., Claesson, P. M., and Venkateshvaran, D., 2022, "Mechanical Properties of Organic Electronic Polymers on the Nanoscale," Adv. Electron. Mater., **8**(3), p. 2101019..
[142] Xiao, M., Sadhanala, A., Abdi-Jalebi, M., Thomas, T. H., Ren, X., Zhang, T., Chen, H., Carey, R. L., Wang, Q., Senanayak, S. P., and Jellett, C., 2021, "Linking Glass-Transition Behavior to Photophysical and Charge Transport Properties of High-Mobility Conjugated Polymers," Adv. Funct. Mater., **31**(7), p. 2007359.
[143] Shpigel, N., Levi, M. D., Sigalov, S., Daikhin, L., and Aurbach, D., 2018, "In Situ Real-Time Mechanical and Morphological Characterization of Electrodes for Electrochemical Energy Storage and Conversion by Electrochemical Quartz Crystal Microbalance With Dissipation Monitoring," Acc. Chem. Res., **51**(1), pp. 69–79.
[144] Chen, Q., Xu, S., Liu, Q., Masliyah, J., and Xu, Z., 2016, "QCM-D Study of Nanoparticle Interactions," Adv. Colloid Interface Sci., **233**, pp. 94–114.
[145] Tummala, N. R., Risko, C., Bruner, C., Dauskardt, R. H., and Brédas, J.-L., 2015, "Entanglements in P3HT and Their Influence on Thin-Film Mechanical Properties: Insights From Molecular Dynamics Simulations," J. Polym. Sci. Part B Polym. Phys., **53**(13), pp. 934–942.
[146] Wang, Y., Li, Z., Niu, K., Xia, W., and Giuntoli, A., 2024, "A Molecular Dynamics Study of Mechanical and Conformational Properties of Conjugated Polymer Thin Films," Macromolecules, **57**(11), pp. 5130–5142.
[147] Root, S. E., Savagatrup, S., Pais, C. J., Arya, G., and Lipomi, D. J., 2016, "Predicting the Mechanical Properties of Organic Semiconductors Using Coarse-Grained Molecular Dynamics Simulations," Macromolecules, **49**(7), pp. 2886–2894.

[148] Rodriquez, D., Kim, J.-H., Root, S. E., Fei, Z., Boufflet, P., Heeney, M., Kim, T.-S., and Lipomi, D. J., 2017, "Comparison of Methods for Determining the Mechanical Properties of Semiconducting Polymer Films for Stretchable Electronics," ACS Appl. Mater. Interfaces, **9**(10), pp. 8855–8862.
[149] Tahk, D., Lee, H. H., and Khang, D.-Y., 2009, "Elastic Moduli of Organic Electronic Materials by the Buckling Method," Macromolecules, **42**(18), pp. 7079–7083.
[150] Mefferd, B. E., Nambiar, V. V., Lu, H., and Stefan, M. C., 2023, "Viscoelastic Characterization of Poly(3-Hexylthiophene): Determination of Young's Modulus," ACS Appl. Polym. Mater., **5**(8), pp. 6318–6324.
[151] Maddali, H., House, K. L., Emge, T. J., and O'Carroll, D. M., 2020, "Identification of the Local Electrical Properties of Crystalline and Amorphous Domains in Electrochemically Doped Conjugated Polymer Thin Films," RSC Adv., **10**(36), pp. 21454–21463.
[152] House, K. L., Christian, K. H., Emge, T. J., Pacheco, H., Haber, R. A., and O'Carroll, D. M., 2024, "Characterization of Nanoscale Morphology and Mechanical Properties of Conjugated Polymer Thin Films Dynamically Exposed to a Secondary Solvent," Polymers, **293**, p. 126625.
[153] Xie, R., Lee, Y., Aplan, M. P., Caggiano, N. J., Müller, C., Colby, R. H., and Gomez, E. D., 2017, "Glass Transition Temperature of Conjugated Polymers by Oscillatory Shear Rheometry," Macromolecules, **50**(13), pp. 5146–5154.
[154] Song, J., Hsu, D. D., Shull, K. R., Phelan, F. R. Jr., Douglas, J. F., Xia, W., and Keten, S., 2018, "Energy Renormalization Method for the Coarse-Graining of Polymer Viscoelasticity," Macromolecules, **51**(10), pp. 3818–3827.
[155] Mikie, T., and Osaka, I., 2020, "Small-Bandgap Quinoid-Based π-Conjugated Polymers," J. Mater. Chem. C, **8**(41), pp. 14262–14288.
[156] Alkahtani, M. E., Elbadawi, M., Chapman, C. A. R., Green, R. A., Gaisford, S., Orlu, M., and Basit, A. W., 2024, "Electroactive Polymers for On-Demand Drug Release," Adv. Healthc. Mater., **13**(3), p. e2301759.
[157] Jacobs, I. E., D'Avino, G., Lemaur, V., Lin, Y., Huang, Y., Chen, C., Harrelson, T. F., et al., 2022, "Structural and Dynamic Disorder, Not Ionic Trapping, Controls Charge Transport in Highly Doped Conducting Polymers," J. Am. Chem. Soc., **144**(7), pp. 3005–3019.
[158] de Vasconcelos, L. S., Xu, R., and Zhao, K., 2020, "Quantitative Spatiotemporal Li Profiling Using Nanoindentation," J. Mech. Phys. Solids, **144**, p. 104102.
[159] Mooney, M., 1940, "A Theory of Large Elastic Deformation," J. Appl. Phys., **11**(9), pp. 582–592.
[160] Rivlin, R. S., and Rideal, E. K., 1997, "Large Elastic Deformations of Isotropic Materials IV. Further Developments of the General Theory," Philos. Trans. R. Soc. Lond. Ser. Math. Phys. Sci., **241**(835), pp. 379–397.
[161] Doi, M., and Edwards, S. F., 1988, *The Theory of Polymer Dynamics*, Oxford University Press, Oxford, New York.
[162] Cho, K. S., 2016, "Nonlinear Constitutive Equations," *Viscoelasticity of Polymers: Theory and Numerical Algorithms*, K. S. Cho, ed., Springer Netherlands, Dordrecht, The Netherlands, pp. 491–543.
[163] Ogden, R. W., and Roxburgh, D. G., 1999, "A Pseudo–Elastic Model for the Mullins Effect in Filled Rubber," Proc. R. Soc. Lond. Ser. Math. Phys. Eng. Sci., **455**(1988), pp. 2861–2877.
[164] Marckmann, G., Verron, E., Gornet, L., Chagnon, G., Charrier, P., and Fort, P., 2002, "A Theory of Network Alteration for the Mullins Effect," J. Mech. Phys. Solids, **50**(9), pp. 2011–2028.
[165] Bristow, G. M., and Westall, B., 1967, "The Molecular Weight Distribution of Natural Rubber," Polymers, **8**, pp. 609–617.
[166] Galuska, L. A., McNutt, W. W., Qian, Z., Zhang, S., Weller, D. W., Dhakal, S., King, E. R., Morgan, S. E., Azoulay, J. D., Mei, J., and Gu, X., 2020, "Impact of Backbone Rigidity on the Thermomechanical Properties of Semiconducting Polymers With Conjugation Break Spacers," Macromolecules, **53**(14), pp. 6032–6042.
[167] Kayser, L. V., Russell, M. D., Rodriquez, D., Abuhamdieh, S. N., Dhong, C., Khan, S., Stein, A. N., Ramírez, J., and Lipomi, D. J., 2018, "RAFT Polymerization of an Intrinsically Stretchable Water-Soluble Block Copolymer Scaffold for PEDOT," Chem. Mater., **30**(13), pp. 4459–4468.
[168] Bernards, D. A., and Malliaras, G. G., 2007, "Steady-State and Transient Behavior of Organic Electrochemical Transistors," Adv. Funct. Mater., **17**(17), pp. 3538–3544.
[169] Kaphle, V., Paudel, P. R., Dahal, D., Radha Krishnan, R. K., and Lüssem, B., 2020, "Finding the Equilibrium of Organic Electrochemical Transistors," Nat. Commun., **11**(1), p. 2515.
[170] Ghasemi, M., Balar, N., Peng, Z., Hu, H., Qin, Y., Kim, T., Rech, J. J., et al., 2021, "A Molecular Interaction–Diffusion Framework for Predicting Organic Solar Cell Stability," Nat. Mater., **20**(4), pp. 525–532.
[171] Flagg, L. Q., Bischak, C. G., Onorato, J. W., Rashid, R. B., Luscombe, C. K., and Ginger, D. S., 2019, "Polymer Crystallinity Controls Water Uptake in Glycol Side-Chain Polymer Organic Electrochemical Transistors," J. Am. Chem. Soc., **141**(10), pp. 4345–4354.
[172] Collins, G. W., Lone, M. S., Jackson, S. R., Keller, J. N., Kingsford, R. L., Noriega, R., and Bischak, C. G., 2024, "Photoluminescence Probes Ion Insertion Into Amorphous and Crystalline Regions of Organic Mixed Conductors," Adv. Funct. Mater., **34**(40), p. 2403710.
[173] Yeo, J.-S., Yun, J.-M., Kim, D.-Y., Park, S., Kim, S.-S., Yoon, M.-H., Kim, T.-W., and Na, S.-I., 2012, "Significant Vertical Phase Separation in Solvent-Vapor-Annealed Poly(3,4-Ethylenedioxythiophene):Poly(Styrene Sulfonate) Composite Films Leading to Better Conductivity and Work Function for High-Performance Indium Tin Oxide-Free Optoelectronics," ACS Appl. Mater. Interfaces, **4**(5), pp. 2551–2560.
[174] Ouyang, L., Musumeci, C., Jafari, M. J., Ederth, T., and Inganäs, O., 2015, "Imaging the Phase Separation Between PEDOT and Polyelectrolytes During Processing of Highly Conductive PEDOT:PSS Films," ACS Appl. Mater. Interfaces, **7**(35), pp. 19764–19773.
[175] Ding, Z., Liu, D., Zhao, K., and Han, Y., 2021, "Optimizing Morphology to Trade Off Charge Transport and Mechanical Properties of Stretchable Conjugated Polymer Films," Macromolecules, **54**(9), pp. 3907–3926.
[176] Melling, D. A., Wilson, S. H., and Jager, E. W., 2015, "Controlling the Electro-Mechanical Performance of Polypyrrole Through 3- and 3,4-Methyl Substituted Copolymers," RSC Adv., **5**(102), pp. 84153–84163.
[177] Tropp, J., Meli, D., Wu, R., Xu, B., Hunt, S. B., Azoulay, J. D., Paulsen, B. D., and Rivnay, J., 2023, "Revealing the Impact of Molecular Weight on Mixed Conduction in Glycolated Polythiophenes Through Electrolyte Choice," ACS Mater. Lett., **5**(5), pp. 1367–1375.
[178] Siemons, N., Pearce, D., Yu, H., Tuladhar, S. M., LeCroy, G. S., Sheelamanthula, R., Hallani, R. K., Salleo, A., McCulloch, I., Giovannitti, A., Frost, J. M., and Nelson, J., 2023, "Controlling Swelling in Mixed Transport Polymers Through Alkyl Side-Chain Physical Cross-Linking," Proc. Natl. Acad. Sci., **120**(35), p. e2306272120.
[179] Maria, I. P., Paulsen, B. D., Savva, A., Ohayon, D., Wu, R., Hallani, R., Basu, A., et al., 2021, "The Effect of Alkyl Spacers on the Mixed Ionic-Electronic Conduction Properties of N-Type Polymers," Adv. Funct. Mater., **31**(14), p. 2008718.
[180] Modarresi, M., and Zozoulenko, I., 2022, "Why Does Solvent Treatment Increase the Conductivity of PEDOT:PSS? Insight From Molecular Dynamics Simulations," Phys. Chem. Chem. Phys., **24**(36), pp. 22073–22082.
[181] Wu, R., Paulsen, B. D., Ma, Q., McCulloch, I., and Rivnay, J., 2023, "Quantitative Composition and Mesoscale Ion Distribution in P-Type Organic Mixed Ionic-Electronic Conductors," ACS Appl. Mater. Interfaces, **15**(25), pp. 30553–30566.
[182] Zheng, Y., Wang, G.-J. N., Kang, J., Nikolka, M., Wu, H.-C., Tran, H., Zhang, S., et al., 2019, "An Intrinsically Stretchable High-Performance Polymer Semiconductor With Low Crystallinity," Adv. Funct. Mater., **29**(46), p. 1905340.
[183] Zheng, Y., Ashizawa, M., Zhang, S., Kang, J., Nikzad, S., Yu, Z., Ochiai, Y., et al., 2020, "Tuning the Mechanical Properties of a Polymer Semiconductor by Modulating Hydrogen Bonding Interactions," Chem. Mater., **32**(13), pp. 5700–5714.
[184] Craighero, M., Guo, J., Zokaei, S., Griggs, S., Tian, J., Asatryan, J., Kimpel, J., et al., 2024, "Impact of Oligoether Side-Chain Length on the Thermoelectric Properties of a Polar Polythiophene," ACS Appl. Electron. Mater., **6**(5), pp. 2909–2916.
[185] Dai, Y., Wai, S., Li, P., Shan, N., Cao, Z., Li, Y., Wang, Y., et al., 2024, "Soft Hydrogel Semiconductors With Augmented Biointeractive Functions," Science, **386**(6720), pp. 431–439.
[186] Chen, J., Huang, W., Zheng, D., Xie, Z., Zhuang, X., Zhao, D., Chen, Y., et al., 2022, "Highly Stretchable Organic Electrochemical Transistors With Strain-Resistant Performance," Nat. Mater., **21**(5), pp. 564–571.
[187] Flagg, L. Q., Giridharagopal, R., Guo, J., and Ginger, D. S., 2018, "Anion-Dependent Doping and Charge Transport in Organic Electrochemical Transistors," Chem. Mater., **30**(15), pp. 5380–5389.
[188] Wei, B., Liu, J., Ouyang, L., Kuo, C.-C., and Martin, D. C., 2015, "Significant Enhancement of PEDOT Thin Film Adhesion to Inorganic Solid Substrates With EDOT-Acid," ACS Appl. Mater. Interfaces, **7**(28), pp. 15388–15394.
[189] Ouyang, L., Wei, B., Kuo, C., Pathak, S., Farrell, B., and Martin, D. C., 2017, "Enhanced PEDOT Adhesion on Solid Substrates With Electrografted P(EDOT-NH2)," Sci. Adv., **3**(3), p. e1600448.
[190] Villemin, E., Lemarque, B., Vũ, T. T., Nguyen, V. Q., Trippé-Allard, G., Martin, P., Lacaze, P.-C., and Lacroix, J.-C., 2019, "Improved Adhesion of Poly(3,4-Ethylenedioxythiophene) (PEDOT) Thin Film to Solid Substrates Using Electrografted Promoters and Application to Efficient Nanoplasmonic Devices," Synth. Met., **248**, pp. 45–52.
[191] Wang, Y., Zeglio, E., Liao, H., Xu, J., Liu, F., Li, Z., Maria, I. P., Mawad, D., Herland, A., McCulloch, I., and Yue, W., 2019, "Hybrid Alkyl–Ethylene Glycol Side Chains Enhance Substrate Adhesion and Operational Stability in Accumulation Mode Organic Electrochemical Transistors," Chem. Mater., **31**(23), pp. 9797–9806.
[192] Gu, K., and Loo, Y.-L., 2019, "The Polymer Physics of Multiscale Charge Transport in Conjugated Systems," J. Polym. Sci. Part B Polym. Phys., **57**(23), pp. 1559–1571.
[193] Zuo, J. M., Vartanyants, I., Gao, M., Zhang, R., and Nagahara, L. A., 2003, "Atomic Resolution Imaging of a Carbon Nanotube From Diffraction Intensities," Science, **300**(5624), pp. 1419–1421.
[194] Wang, S., Wang, Y., Cai, X., Wang, B., Zhao, C., Pan, G., Harder, C., et al., 2025, "A High-Frequency Artificial Nerve Based on Homogeneously Integrated Organic Electrochemical Transistors," Nat. Electron., **8**(3), pp. 254–266.
[195] Ke, Z., Abtahi, A., Hwang, J., Chen, K., Chaudhary, J., Song, I., Perera, K., You, L., Baustert, K. N., Graham, K. R., and Mei, J., 2023, "Highly Conductive and Solution-Processable n-Doped Transparent Organic Conductor," J. Am. Chem. Soc., **145**(6), pp. 3706–3715.
[196] Guan, C., Xiao, C., Liu, X., Hu, Z., Wang, R., Wang, C., Xie, C., Cai, Z., and Li, W., 2023, "Non-Covalent Interactions Between Polyvinyl Chloride and Conjugated Polymers Enable Excellent Mechanical Properties and High Stability in Organic Solar Cells," Angew. Chem. Int. Ed., **62**(44), p. e202312357.
[197] Rivnay, J., Inal, S., Collins, B. A., Sessolo, M., Stavrinidou, E., Strakosas, X., Tassone, C., Delongchamp, D. M., and Malliaras, G. G., 2016, "Structural Control of Mixed Ionic and Electronic Transport in Conducting Polymers," Nat. Commun., **7**(1), p. 11287.

[198] Tan, S. T. M., Giovannitti, A., Marks, A., Moser, M., Quill, T. J., McCulloch, I., Salleo, A., and Bonacchini, G. E., 2022, "Conjugated Polymers for Microwave Applications: Untethered Sensing Platforms and Multifunctional Devices," Adv. Mater., **34**(33), p. 2202994.
[199] Zhao, H., Xu, J., Yuan, H., Zhang, E., Dai, N., Gao, Z., Huang, Y., Lv, F., Liu, L., Gu, Q., and Wang, S., 2022, "3D Printing of Artificial Skin Patches With Bioactive and Optically Active Polymer Materials for Anti-Infection and Augmenting Wound Repair," Mater. Horiz., **9**(1), pp. 342–349.
[200] Park, K. S., Kwok, J. J., Kafle, P., and Diao, Y., 2021, "When Assembly Meets Processing: Tuning Multiscale Morphology of Printed Conjugated Polymers for Controlled Charge Transport," Chem. Mater., **33**(2), pp. 469–498.
[201] Matsui, T., Inose, Y., Powell, D. A., and Shadrivov, I. V., 2016, "Electroactive Tuning of Double-Layered Metamaterials Based on π-Conjugated Polymer Actuators," Adv. Opt. Mater., **4**(1), pp. 135–140.
[202] Sun, R., Park, K. S., Comstock, A. H., McConnell, A., Chen, Y.-C., Zhang, P., Beratan, D., et al., 2024, "Inverse Chirality-Induced Spin Selectivity Effect in Chiral Assemblies of π-Conjugated Polymers," Nat. Mater., **23**(6), pp. 782–789.